

1

2

AEOLIAN SEDIMENT AVAILABILITY AND TRANSPORT

3

BAS HOONHOUT

4

<sup>5</sup> Aeolian Sediment Availability and Transport © 2016, Bas Hoonhout

<sup>6</sup> ISBN: XXX-XX-XXXX-XXX-X

7

8

## AEOLIAN SEDIMENT AVAILABILITY AND TRANSPORT

9

### PROEFSCHRIFT

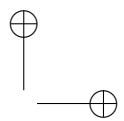
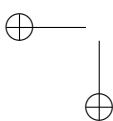
10 ter verkrijging van de graad van doctor  
11 aan de Technische Universiteit Delft;  
12 op gezag van de Rector Magnificus prof. ir. K.Ch.A.M. Luyben  
13 voorzitter van het College voor Promoties  
14 in het openbaar te verdedigen op ... dag ... .....  
15 om ... : ... uur.

16

door

17

Bastiaan Martin HOONHOUT  
18 civiel technisch ingenieur  
19 geboren te Amsterdam



<sup>21</sup> DIT PROEFSCHRIFT IS GOEDGEKEURD DOOR DE PROMOTOR:

Prof. dr. ir. M.J.F. Stive

<sup>22</sup> SAMENSTELLING PROMOTIE COMMISSIE:

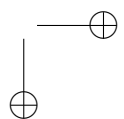
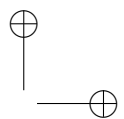
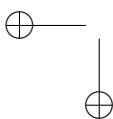
Rector Magnificus	Voorzitter
Prof. dr. ir. M.J.F. Stive	Technische Universiteit Delft, Promotor
Dr. ir. S. de Vries	Technische Universiteit Delft
...	...
...	...
...	...

<sup>23</sup> Dr. ir. J. S. M. van Thiel de Vries en Dr. ir. S. de Vries hebben als begeleider in  
<sup>24</sup> belangrijke mate aan de totstandkoming van het proefschrift bijgedragen.

<sup>25</sup> Het onderzoek ten behoeve van dit proefschrift is gefinancierd door de ERC-  
<sup>26</sup> Advanced Grant 291206 – Nearshore Monitoring and Modeling (NEMO) en Deltares.

28     *All these years they worked like slaves. But they were happy in their work; they grudged no*  
29         *effort or sacrifice, well aware that everything that they did was for the benefit of*  
30         *themselves and those of their kind who would come after them, and not for a pack of idle,*  
31         *thieving human beings.*

32             — George Orwell in Animal Farm (1945)



"thesis" — 2016/11/15 — 10:57 — page vi — #6

---

33 CONTENTS

34	1	INTRODUCTION	1
35	1.1	Motivation . . . . .	1
36	1.2	Research objectives . . . . .	3
37	1.3	Thesis outline . . . . .	4
38	i	FIELD DATA	7
39	2	LARGE SCALE SEDIMENT BUDGETS	9
40	2.1	Introduction . . . . .	9
41	2.2	Field Site . . . . .	10
42	2.3	Methodology . . . . .	11
43	2.3.1	Topographic measurements . . . . .	14
44	2.3.2	Zonation . . . . .	14
45	2.3.3	Spatial variations in porosity . . . . .	16
46	2.4	Results . . . . .	18
47	2.4.1	Morphological change and porosity . . . . .	18
48	2.4.2	Aeolian sediment budgets . . . . .	19
49	2.4.3	Alongshore variation . . . . .	21
50	2.5	Discussion . . . . .	21
51	2.5.1	Sources of inaccuracies . . . . .	22
52	2.5.2	Beach armoring . . . . .	24
53	2.5.3	Mega nourishments as coastal protection . . . . .	25
54	2.6	Conclusions . . . . .	26
55	3	SMALL SCALE SEDIMENT TRANSPORT	27
56	3.1	Introduction . . . . .	27
57	3.2	Field Site . . . . .	28
58	3.3	Methodology . . . . .	30
59	3.3.1	Equipment . . . . .	30
60	3.3.2	Deployments . . . . .	32
61	3.3.3	Data analysis . . . . .	32
62	3.4	Results . . . . .	34
63	3.4.1	Relation between sediment transport and wind speed and water level . . . . .	34
64	3.4.2	Wind direction and sediment source areas . . . . .	36
65	3.4.3	Spatial gradients in sediment transport . . . . .	36
66	3.4.4	Fetch vs. sediment availability . . . . .	41
67	3.5	Discussion . . . . .	41
68	3.6	Conclusions . . . . .	44
70	ii	NUMERICAL MODELING	45
71	4	NUMERICAL MODEL	47
72	4.1	Introduction . . . . .	47
73	4.2	Model Challenges: Bed Surface Properties . . . . .	49
74	4.2.1	Temporal Variations in Bed Surface Properties . . . . .	49

75	4.2.2 Spatial Variations in Bed Surface Properties . . . . .	50
76	4.3 Model Concepts: Sediment Availability, Saturated Transport and En-	
77	trainment . . . . .	51
78	4.4 Model Description . . . . .	53
79	4.4.1 Advection Scheme . . . . .	53
80	4.4.2 Multi-fraction Erosion and Deposition . . . . .	54
81	4.4.3 Simulation of Sediment Sorting and Beach Armoring . . . . .	56
82	4.4.4 Simulation of the Emergence of Non-erodible Roughness Ele-	
83	ments . . . . .	58
84	4.4.5 Simulation of the Hydraulic Mixing, Infiltration and Evaporation	58
85	4.5 Results . . . . .	59
86	4.5.1 Prototype cases . . . . .	59
87	4.5.2 Wind tunnel experiments . . . . .	64
88	4.5.3 Sensitivity . . . . .	65
89	4.6 Discussion . . . . .	68
90	4.6.1 Parameterization . . . . .	69
91	4.6.2 Calibration . . . . .	69
92	4.6.3 Validation . . . . .	70
93	4.7 Conclusions . . . . .	71
94	5 SAND MOTOR HINDCAST	73
95	5.1 Introduction . . . . .	73
96	5.2 Field Site . . . . .	74
97	5.3 Model approach . . . . .	76
98	5.3.1 Reference model . . . . .	76
99	5.3.2 Schematization . . . . .	78
100	5.3.3 Calibration . . . . .	81
101	5.4 Results . . . . .	84
102	5.5 Discussion . . . . .	89
103	5.5.1 Seasonal and local variations in sedimentation and erosion . . .	89
104	5.5.2 Beach armoring, sediment availability and the shear velocity	
105	threshold . . . . .	90
106	5.6 Conclusions . . . . .	91
107	iii DISCUSSION AND CONCLUSIONS	93
108	6 DISCUSSION	95
109	7 CONCLUSIONS	99
110	iv APPENDICES	103
111	A THEORETICAL SEDIMENT TRANSPORT VOLUMES	105
112	B NUMERICAL IMPLEMENTATION	107
113	B.1 Advection equation . . . . .	107
114	B.2 Implicit solver . . . . .	111
115	B.3 Shear velocity threshold . . . . .	112
116	B.3.1 Moisture content . . . . .	112
117	B.3.2 Roughness elements . . . . .	113
118	B.3.3 Salt content . . . . .	113
119	B.3.4 Masks . . . . .	114

120	B.4 Basic Model Interface (BMI) . . . . .	114
121	C MODEL SETTINGS	117
122	BIBLIOGRAPHY	119
123	ACKNOWLEDGMENTS	129
124	CURRICULUM VITAE	131
125	PUBLICATIONS	133
126	COLOPHON	135

"thesis" — 2016/11/15 — 10:57 — page iv — #10

---

127 DEFINITIONS

---

128 **WIND TRANSPORT CAPACITY** [kg/m/s] Transport capacity of the wind over an ide-  
129 alized bed. The wind transport capacity is an upper limit of the (sediment)  
130 transport capacity that includes the influence of bed surface properties.

131 **(SEDIMENT) TRANSPORT CAPACITY** [kg/m/s] Transport capacity of the wind over  
132 a given bed. The (sediment) transport capacity accounts for the impact velocity  
133 threshold. The (sediment) transport capacity is an upper limit of the actual  
134 sediment transport.

135 **EQUILIBRIUM SEDIMENT TRANSPORT** Sediment transport capacity.

136 **SATURATED SEDIMENT TRANSPORT** Sediment transport capacity.

137 **VELOCITY THRESHOLD** [kg/m/s] Impact velocity threshold at which sediment trans-  
138 port is sustained over a given bed. The threshold depends on bed surface prop-  
139 erties that may hamper saltation, e.g. roughness, moist, salt, and represents the  
140 difference between the wind and (sediment) transport capacity.

141 **SEDIMENT AVAILABILITY** [kg/m<sup>2</sup>] Sediment currently available for entrainment  
142 (following [Kocurek and Lancaster, 1999](#)). The sediment availability includes  
143 the fluid velocity threshold at which sediment transport is initiated. Sediment  
144 availability may result in sediment supply if wind is sufficient.

145 **SEDIMENT ENTRAINMENT** [kg/m<sup>2</sup>/s] Entrainment of currently available sediment  
146 by the wind and contributing to the sediment supply.

147 **SEDIMENT SUPPLY** [kg/m/s] Transport of entrained sediment from one location to  
148 another, e.g. from marine sources to intertidal beach or from intertidal beach to  
149 dunes.

150 **TRANSPORT-LIMITED** Transport is determined by the wind transport capacity. An  
151 increase in wind speed will result in an increase in sediment transport as long  
152 as sediment is still available. If insufficient sediment is available, the coastal  
153 system becomes availability-limited.

154 **AVAILABILITY-LIMITED** Transport is determined by the availability of aeolian sed-  
155 iment. An increase in wind speed will not result in an increase in sediment  
156 transport as no additional sediment is available. A decrease in wind speed can  
157 result in a transport-limited coastal system as the sediment availability might be  
158 able to fulfill the demand from the reduced wind.

159 **SUPPLY-LIMITED** Availability-limited.

160 **FETCH-LIMITED** Transport is determined by the available fetch and therefore a wider  
161 beach or more oblique wind will result in an increase in sediment transport. In

162 this thesis fetch is only considered a limiting factor on an idealized bed with  
163 maximum sediment availability (i.e. flat, dry, loose and homogeneous). The  
164 coastal system is considered fetch-limited if and only if the available fetch is  
165 shorter than the fetch necessary for the development of a saturated saltation  
166 cascade in these idealized conditions. In all other cases where the available fetch  
167 influences the sediment transport, the coastal system is considered availability-  
168 limited.

169 **SEDIMENT SORTING** Spatial sorting of (sandy) sediment, either horizontally or ver-  
170 tically, due to differences in (sediment) transport capacity between sediment  
171 fractions.

172 **BEACH ARMORING** Emergence of non-erodible roughness elements from the bed  
173 that shelter (sandy) sediment from wind erosion, resulting in spatiotemporal  
174 differences in sediment availability.

---

<sup>175</sup> ACRONYMS

---

<b>2DH</b>	Two-Dimensional in a Horizontal plane
<b>2DV</b>	Two-Dimensional in a Vertical plane
<b>ATV</b>	All-Terrain Vehicle
<b>AEOLIS</b>	Aeolian sediment transport with Limited Supply
<b>DN</b>	Deployment Number
<b>KNMI</b>	Koninklijk Nederlands Meteorologisch Instituut
<sup>176</sup> <b>MCMC</b>	Markov Chain Monte Carlo
<b>MSL</b>	Mean Sea Level
<b>MEGAPEX</b>	Mega Perturbation EXperiment
<b>NEMO</b>	Nearshore Modeling and Monitoring
<b>R<sup>2</sup></b>	R-squared or Coefficient of Determination
<b>RMSE</b>	Root Mean Square Error
<b>RTK-GPS</b>	Real-Time Kinematic Global Positioning System

"thesis" — 2016/11/15 — 10:57 — page viii — #14

---

<sup>177</sup> SYMBOLS

---

Symbol	Units	Description
$\alpha$	-	Factor to convert from wind velocity to shear velocity.
$\beta$	-	Ratio between drag coefficients of bare surface and roughness elements.
$\theta_u$	-	Wind direction.
$\Gamma$	-	Implicitness parameter.
$\gamma$	-	Maximum wave height over depth ratio.
$\zeta$	-	Bed interaction factor.
$\eta$	m+MSL	Still water level.
$\hat{\eta}$	m+MSL	Local water level.
$\kappa$	-	Von Kármán constant.
$\lambda$	-	Roughness density.
$\xi$	-	Surf similarity parameter.
$\rho_a$	kg/m <sup>3</sup>	Air density.
$\rho_p$	kg/m <sup>3</sup>	Grain density.
$\rho_w$	kg/m <sup>3</sup>	Water density.
$\sigma$	-	Ratio between surface area and frontal area of roughness elements.
$\Phi$	kg/m/s	Space-integrated entrainment function.
$\phi$	kg/m <sup>2</sup> /s	Entrainment function.
$\Psi$	kg/s	Sediment transport potential.
$A$	-	Empirical coefficient.
$A_c$	m <sup>2</sup>	Surface area of control area.
$C$	-	Empirical coefficient to account for grain size distribution width.
$C_c$	kg/m <sup>3</sup>	Sediment concentration in the air as used by <a href="#">de Vries et al. (2014b)</a> . Relates to $c$ as $c = h C_c$ .
$c$	kg/m <sup>2</sup>	Sediment concentration in the air.
$c_{sat}$	kg/m <sup>2</sup>	Saturated sediment concentration in the air.
$D$	kg/m <sup>2</sup>	Total deposition.
$D_n$	m	Reference median grain size (250 µm).
$d$	m	Water depth.
$d_{50}$	m	Median grain size.
$d_n$	m	Nominal grain size.
$E$	kg/m <sup>2</sup>	Total erosion.
$E_v$	m/s	Evaporation rate.
$F$	m	Available fetch.
$\hat{F}$	m	Effective fetch.
$F_c$	m	Critical fetch.
$f_{\Delta z_d}$	-	Depth of disturbance factor.

Symbol	Units	Description	(continued)
$f_{\theta_u}$	-	Factor to include wind direction in sediment transport capacity.	
$f_{u_{*th},M}$	-	Factor to include the influence of moisture to the shear velocity threshold $u_{*th}$ .	
$f_{u_{*th},R}$	-	Factor to include the influence of roughness elements to the shear velocity threshold $u_{*th}$ . Relates to $R_t$ as $R_t = \frac{1}{f_{u_{*th},R}}$ .	
$f_{u_{*th},S}$	-	Factor to include the influence of salt to the shear velocity threshold $u_{*th}$ .	
$g$	$\text{m/s}^2$	Gravitational constant.	
$H$	m	Offshore wave height.	
$\hat{H}$	m	Local wave height.	
$h$	m	Height of saltation layer.	
$i$	-	Cross-shore grid index.	
$j$	-	Alongshore grid index.	
$K^+$	-	Hydrodynamic addition mask.	
$K^\times$	-	Hydrodynamic multiplication mask.	
$k$	-	Grain size fraction index.	
$k_0$	-	Index of smallest non-erodible grain size fraction.	
$l$	-	Diagonal index.	
$m$	-	Factor to account for difference between mean and maximum shear stress.	
$m_a$	$\text{kg/m}^2$	Sediment availability.	
$n$	-	Time step index.	
$n_k$	-	Number of grain size fractions.	
$n_{pc}$	-	Number of counted particles.	
$n_x$	-	Number of grid cells in cross-shore direction.	
$n_y$	-	Number of grid cells in alongshore direction.	
$p$	-	Porosity.	
$p_g$	$\text{kg/kg}$	Geotechnical mass content of water.	
$p_s$	$\text{mg/g}$	Salt content.	
$p_V$	$\text{m}^3/\text{m}^3$	Volumetric water content.	
$Q$	$\text{m}^3$	Cumulative sediment transport capacity.	
$q$	$\text{kg/m/s}$	Sediment transport rate.	
$q_{sat}$	$\text{kg/m/s}$	Saturated sediment transport rate.	
$R$	m	Wave runup height.	
$R_t$	-	Ratio between velocity threshold on bare surface $u_{*th,S}$ and on surface including roughness elements $u_{*th,R}$ .	
$S_k$	-	Degree of saturation of grain size fraction $k$ .	
$\hat{S}_k$	-	Effective degree of saturation of grain size fraction $k$ , including the bed interaction parameter $\zeta$ .	
$T$	s	Adaptation time scale in advection equation.	
$t$	s	Time.	
$\Delta t^n$	s	Size of time step $n$ .	
$u_*$	$\text{m/s}$	Shear velocity.	
$u_z$	$\text{m/s}$	Wind velocity at height $z$ .	

Symbol	Units	Description	(continued)
$u_{*th,R}$	m/s	Shear velocity threshold of surface including roughness elements.	
$u_{*th,S}$	m/s	Shear velocity threshold of bare surface.	
$u_{*th}$	m/s	Shear velocity threshold.	
$u_{th}$	m/s	Wind velocity threshold.	
$u_{z,x}$	m/s	Wind velocity component in x-direction and at height $z$ .	
$u_{z,y}$	m/s	Wind velocity component in y-direction and at height $z$ .	
$V$	$\text{m}^3$	Sediment volume.	
$V_{40\%}$	$\text{m}^3$	Sediment volume normalized to 40% porosity.	
$\Delta V^n$	$\text{m}^3$	Change in sediment volume in time step $n$ .	
$w_k$	-	Weighting factor for grain size fraction $k$ in right-hand-side of the advection equation.	
$w_k^{\text{air}}$	-	Weighting factor for grain size fraction $k$ based on the grain size distribution in the air.	
$w_k^{\text{bed}}$	-	Weighting factor for grain size fraction $k$ based on the grain size distribution in the bed.	
$x$	m	Cross-shore distance.	
$\Delta x_{i,j}$	m	Size of grid cell $i, j$ in cross-shore direction.	
$y$	m	Alongshore distance.	
$\Delta y_{i,j}$	m	Size of grid cell $i, j$ in alongshore direction.	
$z$	m	Height above the bed.	
$z'$	m	Thickness of inner boundary layer.	
$z_b$	$\text{m+MSL}$	Bed level.	
$\Delta z_d$	m	Depth of disturbance.	

"thesis" — 2016/11/15 — 10:57 — page xii — #18

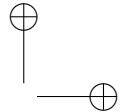
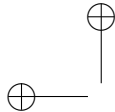
---

178 LIST OF FIGURES

---

179	Figure 2.1	Location, orientation, appearance and evolution of the Sand Motor between construction in 2011 and 2015. The box indicates the measurement domain used in the remainder of this paper. A 100 x 100 m grid aligned with the measurement domain is plotted in gray as reference. . . . .	12
180			
181			
182			
183			
184	Figure 2.2	Wind and hydrodynamic time series from 2011 to 2015. Hourly averaged wind speeds and directions are obtained from the KNMI meteorological station in Hoek van Holland (upper panels). Offshore still water levels, wave heights and wave periods are obtained from the Europlatform (lower panels). Runup levels are estimated following Stockdon et al. (2006). . . . .	13
185			
186			
187			
188			
189			
190	Figure 2.3	Zonation of the Sand Motor domain into zones with net aeolian erosion and no marine influence, net aeolian deposition and no marine influence, mixed aeolian/marine influence and marine influence. Left panels: 2011. Right panels: 2015. . . . .	15
191			
192			
193			
194	Figure 2.4	Yearly sedimentation and erosion above 0 m+MSL in the Sand Motor domain. Comparisons are made between the September surveys of each year. . . . .	17
195			
196			
197	Figure 2.5	Aeolian sediment budgets in the Sand Motor domain in the period between September 1, 2011 and September 1, 2015. . . . .	19
198			
199	Figure 2.6	Cumulative change in sediment volume of all net aeolian erosion and net aeolian deposition zones and the volume deficit. For the linear fit the period prior to February 2012 is discarded (shaded). . . . .	20
200			
201			
202			
203	Figure 2.7	Change in size of aeolian zone and mixed zones since construction of the Sand Motor in 2011. . . . .	20
204			
205	Figure 2.8	Average height of the aeolian zone in the most recent contour. . . . .	21
206	Figure 2.9	Comparison sediment accumulation rates in dunes (>3 m+MSL) for Sand Motor domain and adjacent coasts. Airborne lidar measurements from January 2012 until January 2015 are used. Horizontal dashed lines indicate local averages. The box indicates the Sand Motor domain depicted in previous figures. . . . .	22
207			
208			
209			
210			
211			
212	Figure 2.10	Aeolian sediment budget analysis of the Sand Motor . . . . .	23
213	Figure 3.1	Location, orientation, appearance and evolution of the Sand Motor between construction 2011 and 2015. The box indicates the measurement domain used in the remainder of this paper. A 100 x 100 m grid aligned with the measurement domain is plotted in gray as reference. . . . .	29
214			
215			
216			
217			
218	Figure 3.2	Overview of measurement transects N, W, and SW and locations during the MEGAPEX field campaign. . . . .	30
219			

220	Figure 3.3	Mast with 6 Wenglor fork laser sensors and a Gill 2D Wind-Sonic ultrasonic wind speed and direction sensor. The top 3 laser sensors are optional. . . . .	31
221			
222			
223	Figure 3.4	Wind time series (upper panel), overall particle count rates during the deployments along the westerly transect (middle panel) and offshore tidal elevation (lower panel). Grey lines indicate the raw data, black lines the hourly averaged data. Colored bars refer to the deployments listed in Table 3.1. Deployments DNo2b and DNo6a are not included as these are located along different transects. . . . .	35
224			
225			
226			
227			
228			
229			
230	Figure 3.5	Relations between overall particle count and wind speed (left panel) or water level (right panel). Closed circles and continuous lines refer to non-storm deployments DNo2 to DNo9. Open circles and dashed lines refer to storm deployments DNo10 and DNo11. All deployments are listed in Table 3.1. . . . .	36
231			
232			
233			
234			
235	Figure 3.6	Per-mast particle count, wind speed and direction obtained from stationary mast (Figure 3.2, upper panel) and available fetch and intertidal fetches (lower panel). . . . .	37
236			
237			
238	Figure 3.7	Average per-mast particle count rates during the deployments along the westerly transect (upper panel) and beach profile (lower panel). Line colors refer to the partitioning of the time series in Figure 3.4. . . . .	38
239			
240			
241			
242	Figure 3.8	Average per-mast particle count rates during deployment DNo6a along the southwesterly transect (upper panel) and beach profile (lower panel). . . . .	38
243			
244			
245	Figure 3.9	Erosion measured using erosion pins during five tidal cycles during deployment DNo6a along the southwesterly transect. . . . .	39
246			
247	Figure 3.10	Cumulative particle count distribution over the vertical during deployment DNo8. The line indicates the percentage of particles that surpasses a certain height above the bed. The horizontal bars visualize the variability in time of the particle count per laser sensor. . . . .	40
248			
249			
250			
251			
252	Figure 3.11	Average overall particle count rates depending on governing wind speed and bed level at measurement location, and average still water level depending on governing wind speed. . . . .	41
253			
254			
255	Figure 3.12	Visual impression of armor layer at three locations in the Sand Motor region: a) intertidal beach, no armoring b) lower dry beach, minor armoring with shell fragments c) upper dry beach, severe armoring with many shells and coarse sand. Covered surface is approximately 40 x 40 cm in all cases. . . . .	42
256			
257			
258			
259			
260	Figure 3.13	Conceptual illustration of how temporal deposits facilitate a continuous sediment supply from the intertidal beach to the dunes. . . . .	43
261			
262			
263	Figure 4.1	Contributions of the grain size distribution in the bed and in the air to the weighting factors $\hat{w}_k$ for the equilibrium sediment concentration in Equation 4.9 for different values of the bed interaction parameter. . . . .	56
264			
265			
266			



## 267 Figure 4.2

268  
269  
270  
271  
272  
273  
274  
275

Schematic of bed composition discretisation and advection scheme. Horizontal exchange of sediment may occur solely through the air that interacts with the *bed surface layer*. The detail presents the simulation of sorting and beach armoring where the bed surface layer in the upwind grid cell becomes coarser due to non-uniform erosion over the sediment fractions, while the bed surface layer in the downwind grid cell becomes finer due to non-uniform deposition over the sediment fractions. Symbols refer to Equations 4.6 and 4.7. . . . .

57

## 276 Figure 4.3

277  
278  
279  
280  
281  
282  
283  
284  
285  
286  
287  
288

Sediment transport in time and over the model domain for three scenarios with constant wind. Each line depicts a different location along the beach, starting from  $x = 40$  m, which coincides with the high water line in cases P<sub>3</sub> and P<sub>4</sub>, and ends at the dune foot. Results are normalized using the transport rate in case P<sub>1</sub> with almost constant transport (not shown). The difference between the sediment transport at dune foot (green) and the sediment transport at  $x = 40$  m is visualized by the red dots and represents the sediment supply from the dry beach. In cases P<sub>3</sub> and P<sub>4</sub> the sediment transport at the high water line periodically exceeds the sediment transport at the dune foot, indicating local deposition of sediments originating from the intertidal beach. . . . .

61

## 289 Figure 4.4

290  
291  
292  
293  
294  
295

Distribution of the shell fraction over the model domain and in time. Sediment supply is inversely related to the degree of beach armoring, indicated by the shell fraction. Median grain size increases with the increase in shell fraction indicating erosion of predominantly fines. High-energy wind events in case P<sub>4</sub> even mobilize shell fractions resulting in a decrease in beach armoring and an increase in sediment availability. . . . .

62

## 296 Figure 4.5

297  
298  
299  
300  
301  
302  
303  
304  
305

Average reduction in sediment transport in prototype case P<sub>3b</sub> compared to case P<sub>1b</sub> depending on the hourly averaged wind velocity (left panel). The results are obtained using a synthetic variable wind time series following a Weibull distribution with a mean wind velocity of 12 m/s (right panel). The sediment transport reduction (scatter) is binned according to the wind velocity using 0.5 m/s bins. The median reduction per bin (triangles) is used to fit an exponential curve (line). The reduction tends to increase during the simulation (scatter colors). . . . .

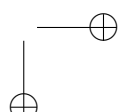
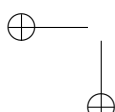
64

## 306 Figure 4.6

307  
308  
309  
310  
311  
312

Comparison between modeled and measured normalized sediment transport rates from wind tunnel experiments described in Nickling and McKenna Neuman (1995). The dashed line depicts the emergence of marbles in terms of increasing roughness density. The visualization of the measurement results is copied from Figure 4 in the original publication without digitization. . . . .

66



313	Figure 4.7	Comparison between model results and measurements from wind tunnel experiments described in Dong et al. (2004b) (left panel) and RMS errors relative to the mean measured transport rate (right panel). The measured transport rates with a wind velocity of 22 m/s are underestimated due to surpassing of sediment over the sediment trap (Dong et al., 2004b). . . . .	67
314			
315			
316			
317			
318			
319	Figure 4.8	Sensitivity of the total normalized sediment transport with respect to case P <sub>3</sub> for four newly introduced parameters and the wind velocity. The sensitivity of the wind velocity is expressed with respect to the transport rate in case P <sub>1</sub> . . . . .	67
320			
321			
322			
323	Figure 5.1	Location, orientation, appearance and evolution of the Sand Motor between construction in 2011 and 2015. The box indicates the measurement domain used in the remainder of this paper. A 100 x 100 m grid aligned with the measurement domain is plotted in gray as reference. . . . .	75
324			
325			
326			
327			
328	Figure 5.2	Wind and hydrodynamic time series from 2011 to 2015. Hourly averaged wind speeds and directions are obtained from the KNMI meteorological station in Hoek van Holland (upper panels). Offshore still water levels, wave heights and wave periods are obtained from the Europlatform (lower panels). Runup levels are estimated following Stockdon et al. (2006). . . . .	77
329			
330			
331			
332			
333			
334	Figure 5.3	Comparison of the cumulative wind transport capacity according to a selection of equilibrium sediment transport formulations and measured total sedimentation in the Sand Motor domain. The equilibrium sediment transport is based on an hourly averaged wind speed and direction time series from September 1, 2011 until September 1, 2015. Offshore wind directions are discarded. For the upper boundary of each estimate all wind directions are weighted equally. For the lower boundary of each estimate the wind directions are weighted according to the magnitude of the onshore component. . . . .	78
335			
336			
337			
338			
339			
340			
341			
342			
343			
344	Figure 5.4	Model grid and topography based on the topographic survey of August 3, 2011 (upper panel) and hydrodynamic mask used to limit tidal and wave motions in the dune lake and lagoon (middle and lower panels). Water levels and wave heights are uniformly imposed to the model and multiplied by the multiplication mask and subsequently increased with the addition mask. . . . .	79
345			
346			
347			
348			
349			
350			
351	Figure 5.5	Zonation of the Sand Motor domain into zones with net aeolian erosion and no marine influence, net aeolian deposition and no marine influence, mixed aeolian/marine influence and marine influence. Zonation is based on the 0, 3 and 5 m+MSL contour lines that roughly correspond with the mean water level, maximum runup level or berm edge and the dune foot respectively. Left panels: 2011. Right panels: 2015. Source: Hoonhout and de Vries (2016a). . . . .	83
352			
353			
354			
355			
356			
357			
358			

359	Figure 5.6	Systematic variation of calibration parameters $\sigma$ and $T_{dry}$ with $T = 1$ s. The circles indicate the realizations made. The colored background depicts a linear interpolation of the $R^2$ values with respect to the data presented in Figure 2.6. The solid isolines depict $R^2$ values from 0.90 to 0.93, while the dashed isolines depict $R^2$ values from 0.0 to 0.9. The red lines depict the relative supply from the mixed zones ranging from 52% to 57%. The yellow star indicates the optimal value model settings. . . . .	84
360			85
361			86
362			86
363			86
364			86
365			86
366			86
367	Figure 5.7	Measured and modeled yearly sedimentation and erosion above 0 m+MSL. Model results only include aeolian sediment transport as hydrodynamic sediment transport is not computed. Comparisons are made between the September surveys of each year. . . . .	87
368			
369			
370			
371			
372	Figure 5.8	Measured and simulated net volume change of erosion and deposition volumes as presented in Figure 2.6. . . . .	
373			
374	Figure 5.9	Total erosion and deposition volumes at the end of the simulation and measured total erosion and deposition volumes as presented in Figure 2.5. . . . .	
375			
376			
377	Figure 5.10	Measured and simulated average beach height in the aeolian zone as presented in Figure 2.8. . . . .	
378			
379	Figure 5.11	Simulated shell fraction in the aeolian zone at the end of the simulation. . . . .	
380			
381	Figure 5.12	The influence of time-varying and space-varying shear velocity thresholds on the total sedimentation volume. The two leftmost bars depict the measured and modeled sedimentation volume as obtained from the calibrated model (Figure 5.9). The middle two bars depict results from two separate model simulations in which a space-averaged threshold time series or a time-averaged threshold field is imposed respectively. The threshold averages are based on the result from the calibrated model. The two rightmost columns depict a result from a separate model simulation with a constant uniform threshold based on only a constant uniform median grain size and the estimated equilibrium sediment transport following Bagnold (1937b) respectively (Table 5.1). . . . .	88
382			
383			
384			
385			
386			
387			
388			
389			
390			
391			
392			
393			
394	Figure 5.13	Relation between shear velocity threshold, shell coverage and $\sigma$ according to Raupach et al. (1993, Equation 4.13). The shaded areas indicate the relevant parameter ranges from McKenna Neuman et al. (2012) (blue) and the model results (green). . . . .	91
395			
396			
397			
398			

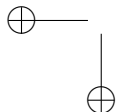
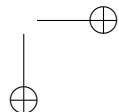
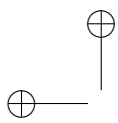
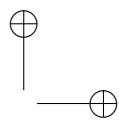
"thesis" — 2016/11/15 — 10:57 — page xviii — #24

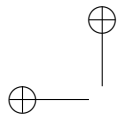
---

399 LIST OF TABLES

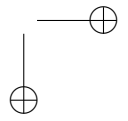
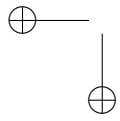
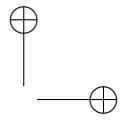
---

400	Table 2.1	Zonation of the Sand Motor domain into seven zones with and without marine influence. See also Figure 2.3. . . . .	16
401	Table 2.2	Measured porosity values in the Sand Motor domain. Each area is sampled at three different locations. The results per area are presented in ascending order. The last column presents the average porosity for each area that is used to convert the sediment volumes presented in this paper to a hypothetical porosity of 40%. . . . .	18
408	Table 3.1	Deployments of measurement masts during the MEGAPEX field campaign. Maximum measured wind speeds are in between brackets. . . . .	33
411	Table 5.1	Equilibrium sediment transport formulations, coefficient values* and the ratio between measurements and model results. .	80
412			





"thesis" — 2016/11/15 — 10:57 — page xx — #26



---

413 ABSTRACT

---

414 This thesis explores the nature of aeolian sediment availability and its influence on  
415 aeolian sediment transport with the aim to improve large scale and long term aeolian  
416 sediment transport estimates in (nourished) coastal environments. The generally poor  
417 performance of aeolian sediment transport models in coastal environments is often  
418 accredited to limitations in sediment availability. Sediment availability can be limited  
419 by particular properties of the bed surface. For example, if the beach is moist or  
420 covered with non-erodible elements, like shells. If sediment availability is limited, the  
421 aeolian sediment transport rate is governed by the sediment availability rather than  
422 the wind transport capacity.

423 Aeolian sediment availability is rather intangible as sediment availability is not only  
424 affected by aeolian processes, but also by marine and meteorological processes that  
425 act on a variety of spatial and temporal scales. The Sand Motor mega nourishment  
426 provides a unique opportunity to quantify the spatiotemporal variations in aeolian  
427 sediment availability and its effect on aeolian sediment transport. Aeolian sediment  
428 accumulation in the Sand Motor region is low compared to the wind transport ca-  
429 pacity, while the Sand Motor itself is virtually permanently exposed to wind and  
430 accommodates large fetches. Aeolian sediment accumulation is therefore largely de-  
431 termined by the sediment availability rather than the wind transport capacity.

432 Multi-annual bi-monthly measurements of the Sand Motor's topography are used  
433 for a large scale aeolian sediment budget analysis. The analysis revealed that aeo-  
434 lian sediment supply from the dry beach area, that is permanently exposed to wind,  
435 diminished a half year after construction of the Sand Motor in 2011 due to the devel-  
436 opment of a beach armor layer. From early 2012, two-third of the aeolian sediment  
437 deposits originate from the intertidal beach area. The source of aeolian sediment in  
438 the Sand Motor region is remarkable as the intertidal beach is periodically flooded  
439 and permanently moist.

440 The importance of the intertidal beach area in the Sand Motor region is tested dur-  
441 ing a six-week field campaign. Gradients in aeolian sediment transport are measured  
442 during the field campaign as to localize aeolian sediment source and sink areas. A  
443 consistent supply from the intertidal beach area was measured that was temporarily  
444 deposited at the dry beach. The temporary deposits were transported further during  
445 high water, when sediment supply from the intertidal beach ceased, resulting in a  
446 continuous sediment supply to the dunes. The temporary deposition of sediment at  
447 the dry beach was likely promoted by the presence of a berm that affects the local  
448 wind shear. Moreover, the berm edge coincided with the onset of the beach armor  
449 layer that might have further promoted deposition of sediment.

450 The measurements on spatiotemporal variations in aeolian sediment availability  
451 and supply inspired an attempt to capture the characteristics of aeolian sediment avail-  
452 ability in coastal environments in a comprehensive model approach. The resulting  
453 model simulates spatiotemporal variations in bed surface properties and their com-  
454 bined influence on aeolian sediment availability and transport. The implementation  
455 of multi-fraction aeolian sediment transport in the model introduces the recurrence

456 relation between aeolian sediment availability and transport through self-grading of  
457 sediment.

458 The model was applied in a four-year hindcast of the Sand Motor mega nourish-  
459 ment as first attempt to field validation. The model reproduces the multi-annual  
460 aeolian sediment erosion and deposition volumes, and the relative importance of the  
461 intertidal beach area as source of aeolian sediment well. Seasonal variations in aeo-  
462 lian sediment transport are incidentally missed by the model. The model accuracy  
463 is reflected in a  $R^2$  value of 0.93 when comparing time series of measured and mod-  
464 eled total aeolian sediment transport volumes in the four years since construction of  
465 the Sand Motor. The results suggest that indeed significant limitations in sediment  
466 availability, due to soil moisture content and beach armoring, govern aeolian sedi-  
467 ment transport in the Sand Motor region. A comparison with a simulation without  
468 limitation in sediment availability suggests that aeolian sediment availability in the  
469 Sand Motor region is limited to about 25% of the wind transport capacity. Moreover,  
470 both spatial and temporal variations in aeolian sediment availability as well as the  
471 recurrence relation between aeolian sediment availability and transport are essential  
472 to accurate long term and large scale aeolian sediment transport estimates.

---

473 SAMENVATTING

---

474 Dit proefschrift onderzoekt de invloed van beschikbaarheid van eolisch sediment op  
475 eolisch sediment transport met als doel het verbeteren van grootschalige en lange ter-  
476 mijn voorspellingen van eolisch sediment transport in (gesuppleerde) kustgebieden.  
477 Bestaande modellen voor eolisch sediment transport presteren in het algemeen slecht  
478 in kustgebieden. De slechte prestaties worden dikwijls geweten aan een beperkte be-  
479 schikbaarheid van eolisch sediment. De beschikbaarheid van eolisch sediment kan  
480 worden beperkt door specifieke eigenschappen van het strandoppervlak. Als bijvoor-  
481beeld het strand vochtig is of bedekt met niet-erodeerbare elementen, zoals schelpen,  
482 kan de beschikbaarheid van sediment worden beperkt. In dat geval wordt de eoli-  
483 sche sediment flux bepaald door de beschikbaarheid van sediment in plaats van de  
484 transportcapaciteit van de wind.

485 De beschikbaarheid van eolisch sediment is een redelijk ongrijpbaar fenomeen, om-  
486 dat deze niet alleen wordt beïnvloed door eolische processen, maar ook door marine  
487 en meteorologische processen die op verschillende ruimtelijke en temporele schalen  
488 actief zijn. De Zandmotor megasuppletie biedt een unieke gelegenheid om de tem-  
489 porele en ruimtelijke variaties in de beschikbaarheid van eolisch sediment en het ef-  
490 effect daarvan op eolisch sediment transport te kwantificeren. Instuifvolumes rond de  
491 Zandmotor zijn klein in vergelijking met de transportcapaciteit van de wind, terwijl  
492 de Zandmotor met haar grote strijklengetjes zelf vrijwel permanent blootgesteld is aan  
493 wind. De instuiving van sediment wordt daar dus grotendeels bepaald door de be-  
494 schikbaarheid van sediment in plaats van de transportcapaciteit van de wind.

495 Meerjarige tweemaandelijks metingen van de topografie van de Zandmotor zijn  
496 gebruikt voor een grootschalige eolische sediment budget analyse. Uit de analyse  
497 bleek dat de aanvoer van eolisch sediment vanaf het droge strand, dat permanent  
498 blootgesteld is aan de wind, vanaf een half jaar na de aanleg van de Zandmotor in  
499 2011 sterk is verminderd als gevolg van het ontstaan van een schelpenlaag. Vanaf het  
500 begin van 2012 is tweederde van het instuivvolume afkomstig uit het intergetijdenge-  
501 bied. Deze bron van eolische sediment rond de Zandmotor is opmerkelijk omdat het  
502 intergetijdenstrand periodiek overstroomd en permanent vochtig is.

503 Het belang van het intergetijdengebied strand rond de Zandmotor wordt beves-  
504 tigd tijdens een zes weken durende veld campagne. Tijdens deze campagne zijn  
505 gradi enten in eolisch sediment transport gemeten de bron van eolisch sediment te  
506 bepalen. De gemeten constante aanvoer vanuit het intergetijdengebied bleek tijde-  
507 lijk te sedimenteren op het droge strand. Deze tijdelijke afzettingen werden tijdens  
508 hoogwater verder getransporteerd wanneer de sediment aanvoer vanaf het intergetij-  
509 denstrand stagneerde. Hierdoor ontstond een continue toevoer van sediment naar de  
510 duinen. De tijdelijke afzetting van sediment op het droge strand werd vermoedelijk  
511 bevorderd door de aanwezigheid van een berm die de lokale schuifspanning van de  
512 wind beïnvloedt. Bovendien viel de rand van de berm samen met het begin van de  
513 schelpenlaag die het neerslaan van sediment mogelijk verder bevorderd heeft.

514 De gemeten ruimtelijke en temporele variaties in de beschikbaarheid van eolisch  
515 sediment hebben een poging geïnspireerd om de kenmerken van beschikbaarheid

516 van eolisch sediment aan de kust te vatten in een alomvattende model aanpak. Het  
517 resulterende model simuleert variaties in tijd en ruimte van eigenschappen van het  
518 strandoppervlak en hun gezamenlijke invloed op de beschikbaarheid en transport van  
519 eolisch sediment. De implementatie van eolisch sediment transport over meerdere  
520 korrelgrootte fracties in het model introduceert de recurrente betrekking tussen de  
521 beschikbaarheid en het transport van eolisch sediment door middel van zelfgradering  
522 van sediment.

523 Het model is toegepast in een vierjarige hindcast van de Zandmotor megasuppletie  
524 als eerste poging tot veldvalidatie. Het model reproduceert de meerjarige erosie  
525 en depositie volumes van eolisch sediment, en het relatieve belang van het interge-  
526 tijdengebied als bron van eolisch sediment, goed. Seizoensafhankelijke variaties in  
527 eolisch sediment transport worden soms gemist door het model. De nauwkeurigheid  
528 van het model is weerspiegeld in een  $R^2$  waarde van 0,93 wanneer gemeten en gemo-  
529 delleerde tijdseries voor het totaal door de wind getransporteerde sedimentvolume  
530 in de vier jaar na constructie van de Zandmotor worden vergeleken. De resultaten  
531 suggereren dat significante beperkingen in sediment beschikbaarheid, als gevolg van  
532 het vochtgehalte van het strand en het vormen van een schelpenlaag, inderdaad be-  
533 palend zijn voor het eolisch sediment transport rond de Zandmotor. Een vergelijking  
534 met een simulatie zonder beperking in beschikbaarheid van sediment suggereert dat  
535 de beschikbaarheid van eolisch sediment rond de Zandmotor is beperkt tot ongeveer  
536 25% van de transportcapaciteit van de wind. Bovendien zijn zowel de ruimtelijke en  
537 temporele variaties in de beschikbaarheid van eolisch sediment, evenals de recurrente  
538 betrekking tussen de beschikbaarheid en transport van eolisch sediment essentieel  
539 voor een nauwkeurige lange termijn en grootschalige voorspellingen van eolisch sedi-  
540 ment transport.

# 1

541

542

## 543 INTRODUCTION

### 544 1.1 MOTIVATION

545 Aeolian sediment transport is a prerequisite to growth and resilience of coastal dunes.  
546 Coastal dunes function as a natural protection against flooding from the sea. As hu-  
547 man societies are particularly attracted to low-lying areas near the sea, the reliability  
548 and resilience of the protective coastal dune systems becomes vital for economic ac-  
549 tivities and human well-being. This societal demand for a safe and comfortable living  
550 space, that initiated the discipline of coastal engineering, developed our understand-  
551 ing of coastal safety tremendously in the past decades. The increased understanding  
552 of our coastal systems resulted in structural mitigation of coastal risks using rigid  
553 solutions or local nourishments (Hamm et al., 2002) and the engineering of entire  
554 coastlines worldwide (Donchyts et al., 2016).

555 With the increased confidence in our ability to mitigate coastal risks, additional de-  
556 mands and functions for coastal flood protections arose. Soft engineering solutions  
557 with limited environmental and ecological impact gained preference over rigid so-  
558 lutions. Recently, the exponent of soft engineering emerged as nature-based coastal  
559 flood protections (Waterman, 2010; de Vriend et al., 2015). Nature-based flood pro-  
560 tections pursue the idea of stimulating natural processes with the aim of increasing  
561 coastal safety and is based on the assumption that the incidental or concentrated  
562 interventions necessary for the stimulation of nature are less intrusive than classic  
563 solutions to coastal safety. Moreover, nature-based solutions tend to accommodate  
564 long-term monitoring and periodic adaptation and intervention that increases flex-  
565 ibility with respect to planning and execution as well as the occurrence of coastal  
566 hazards. The increased flexibility can make nature-based flood protection also cost-  
567 effective (Van Slobbe et al., 2013).

568 An innovative example of a nature-based solution to coastal safety is the Sand Mo-  
569 tor (or Sand Engine, Stive et al., 2013). The Sand Motor is an artificial sandy peninsula  
570 that was constructed along the Dutch coast in 2011. The Sand Motor provides a 21  
571 Mm<sup>3</sup> sediment source to the Dutch coast that is to be dispersed by natural processes,  
572 like tides and waves, over a period of about two decades. Although the construction  
573 of the Sand Motor clearly disturbs the coastal system, the disturbance is incidental  
574 and concentrated. In addition, the presence of the Sand Motor theoretically decreases  
575 the necessity of measures to mitigate coastal risks at other locations along the Dutch  
576 coast.

577 The Sand Motor is the provisional pinnacle of the evolution of soft engineering so-  
578 lutions to coastal safety in The Netherlands. Soft engineering solutions started with

579 the dynamic preservation act of 1990 that prescribes extensive nourishment program  
580 initiated to protect The Netherlands from flooding from the sea (Min. V&W, 1990).  
581 Since the start of the program the distance between nourishments and dunes increased  
582 steadily. The initial dune and beach nourishments were replaced by foreshore nour-  
583 ishments as these are more cost-effective and less intrusive to the environmental and  
584 recreational functions of the coastal dune system. Nature-based solutions, like the  
585 Sand Motor, typically place nourishments kilometers away from the dune system that  
586 needs to be enforced.

587 With the increasing distance between nourishments and dunes, the effectiveness of  
588 nourishments in mitigating coastal risks becomes more difficult to assess. Ultimately  
589 the reliability of coastal dune systems is related to the sediment volume that is con-  
590 tained by the system. However, also the location in the coastal profile where the  
591 sediment resides is important. Sediment in the dunes provides a direct buffer against  
592 flooding in case of storm erosion, while sediment on the beach and foreshore influ-  
593 ences coastal safety indirectly by depth-induced breaking of waves and consequently  
594 a reduction of the critical dune volume required to withstand a normative storm (Wal-  
595 stra, 2016). The sediment volume that resides in the dunes provides arguably a more  
596 persistent protection against flooding as the volume is typically only affected by se-  
597 vere storms. In contrast, the sediment volume that resides on the foreshore and beach  
598 is affected by seasonal nearshore bar cycles and mild storms, which increase the un-  
599 certainty of its contribution to coastal safety. It is therefore relevant to understand  
600 how sediment arrives in the dunes and provide a persistent contribution to coastal  
601 safety.

602 A key issue is to understand sediment transport pathways from nourishment to  
603 dunes. Many studies and sophisticated numerical models are available that describe  
604 hydrodynamic sediment transport. However, only a small fraction of the sediment  
605 moved in the nearshore ultimately arrives in the dunes (Aagaard et al., 2004). It is this  
606 small wind-induced sediment flux that provides us with the natural and persistent  
607 coastal flood protection that nature-based solutions aim for. In addition, this small  
608 wind-induced sediment flux gives coastal dune systems the natural resilience to storm  
609 impacts and the conditions for survival of persistent dune vegetation that strengthens  
610 the coastal dune systems, like marram grass (Borsje et al., 2011). It is also this small  
611 wind-induced sediment flux that is least understood and consistently overestimated  
612 by existing sediment transport models.

613 Aeolian sediment transport models describe the wind-induced sediment transport  
614 rate. In coastal environments these models tend to overestimate the aeolian sediment  
615 accumulation volumes, which is often accredited to limitations in sediment availabil-  
616 ity (Houser, 2009; Delgado-Fernandez et al., 2012; de Vries et al., 2014a). Sediment  
617 availability can be limited by particular properties of the bed surface. For example,  
618 if the beach is moist or covered with non-erodible elements, like shells (Wiggs et al.,  
619 2004; Edwards and Namikas, 2009; Namikas et al., 2010; McKenna Neuman et al.,  
620 2012). If sediment availability is limited, the aeolian sediment transport rate is gov-  
621 erned by the sediment availability rather than the wind transport capacity, which  
622 violates the common assumption in aeolian sediment transport models.

623 This thesis explores the nature of aeolian sediment availability and its influence on  
624 aeolian sediment transport with the aim to improve large scale and long term aeolian  
625 sediment transport estimates in nourished coastal environments. This work is per-

626 formed within the framework of *ERC-Advanced Grant 291206 – Nearshore Monitoring*  
627 *and Modeling (NEMO)* that aims at an integrated modeling strategy for large scale  
628 and long term coastal sediment transport that extends from foreshore to backshore.  
629 Improving aeolian sediment transport estimates helps the completion of the sediment  
630 transport pathways from foreshore to backshore and from nourishment to dunes and  
631 thereby the assessment of measures that attempt to mitigate coastal risks, including  
632 nature-based coastal flood protections, on their effectiveness.

633 1.2 RESEARCH OBJECTIVES

634 This thesis pursues four main research objectives. Each chapter is dedicated to one re-  
635 search objective. The research objectives are elaborated in research questions that are  
636 addressed in the concluding chapter of this thesis (Chapter 7). The research objectives  
637 and questions are formulated as:

638 RESEARCH OBJECTIVE #1 Identify the main sources for aeolian sediment in coastal  
639 environments and particularly at the Sand Motor mega nourishment (Chapter  
640 2).

641 The research questions related to objective #1 are:

- 642 1.1 What is the total aeolian sediment supply at the Sand Motor mega nour-  
643 ishment?
- 644 1.2 What are the main deposition areas of aeolian sediment at the Sand Motor  
645 mega nourishment?
- 646 1.3 What are the main source areas of aeolian sediment at the Sand Motor  
647 mega nourishment?
- 648 1.4 What bed surface characteristics can explain any spatial variations in aeo-  
649 lian sediment supply at the Sand Motor mega nourishment?
- 650 1.5 What is the relevance of these bed surface characteristics for coastal sys-  
651 tems in general?
- 652 1.6 What characteristics of a coastal system determine aeolian sediment supply  
653 and dune growth?

654 RESEARCH OBJECTIVE #2 Identify the main processes that govern aeolian sediment  
655 availability and supply in coastal environments and particularly at the Sand  
656 Motor mega nourishment (Chapter 3).

657 The research questions related to objective #2 are:

- 658 2.1 What bed surface characteristics are related to aeolian sediment supply?
- 659 2.2 What processes govern the supply of aeolian sediment from the source  
660 areas?
- 661 2.3 What processes govern the deposition of aeolian sediment in the deposition  
662 areas?

663 RESEARCH OBJECTIVE #3 Develop a numerical model approach to describe the in-  
664 fluence of spatiotemporal variations in aeolian sediment availability on aeolian  
665 sediment transport and harmonize existing model approaches to aeolian sedi-  
666 ment availability where possible (Chapter 4).

667 The research questions related to objective #3 are:

- 668 3.1 What are existing model approaches to describe the influence of aeolian  
669 sediment availability on aeolian sediment transport, what are the similar-  
670 ties and differences among them and which approaches are mutually ex-  
671 clusive?
- 672 3.2 What processes that were identified to be relevant to aeolian sediment  
673 availability are not covered with sufficient accuracy by existing model ap-  
674 proaches?
- 675 3.3 What are the requirements for a model approach that harmonizes existing,  
676 mutual inclusive model approaches and is conceptually able to describe all  
677 processes relevant to aeolian sediment availability and transport?

678 RESEARCH OBJECTIVE #4 Validate the numerical model approach to reproduce the  
679 location and size of sources for aeolian sediment in coastal environments and  
680 particularly at the Sand Motor mega nourishment (Chapter 5).

681 The research questions related to objective #4 are:

- 682 4.1 Can the calibrated numerical model reproduce the total aeolian sediment  
683 supply at the Sand Motor mega nourishment with any statistical signifi-  
684 cance?
- 685 4.2 Can the calibrated numerical model reproduce the main source and depo-  
686 sition areas at the Sand Motor mega nourishment?
- 687 4.3 What implemented processes are in retrospect significant to the model re-  
688 sult?

689 1.3 THESIS OUTLINE

690 This thesis constitutes four parts:

691 Part I presents field data dedicated to the aeolian sediment supply and transport  
692 at the Sand Motor mega nourishment.

693 Chapter 2 presents a large scale aeolian sediment budget analysis that iden-  
694 tifies the main suppliers of aeolian sediment in the Sand Motor region.

695 The large scale sediment budget analysis inspired the six-week field cam-  
696 paign presented in Chapter 3. Gradients in aeolian sediment transport were  
697 measured during the field campaign. Gradients in aeolian sediment trans-  
698 port reveal areas with net erosion and thereby the sources of aeolian sedi-  
699 ment. The measurements therefore enable a detailed analysis of processes

700 governing the spatiotemporal variations in aeolian sediment availability as  
701 identified in the aeolian sediment budget analysis.

702 Part II presents a numerical model for aeolian sediment availability and transport  
703 that is inspired by the field observations.

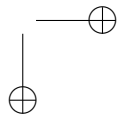
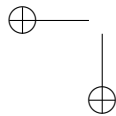
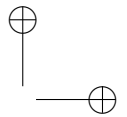
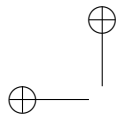
704 The field data show that significant spatial variations in aeolian sediment  
705 availability can exist and can affect net aeolian sediment transport rates. The  
706 variations in aeolian sediment availability coincide with changes in bed sur-  
707 face properties, like soil moisture content and beach armoring. In coastal  
708 environments these bed surface properties typically also vary in time. As-  
709 suming that the spatiotemporal variations in bed surface properties indeed  
710 influence the aeolian sediment availability and transport, a numerical aeolian  
711 sediment transport model is developed.

712 Chapter 4 presents the model philosophy and design. The model focuses on  
713 the incorporation of spatiotemporal variability in aeolian sediment availabil-  
714 ity, which is illustrated using the process of beach armoring. Beach armoring  
715 occurs when roughness elements emerge from the bed and is a typical pro-  
716 cess that causes spatiotemporal variations in aeolian sediment availability.  
717 Both conceptual cases and wind tunnel experiments are used to illustrate  
718 the basic model behavior.

719 Chapter 5 describes the calibration and application of the model to the field  
720 data presented in Chapter 2 as a first attempt to field validation of the nu-  
721 mercial model.

722 Part III concludes this thesis by addressing the research objectives and questions,  
723 and a discussion on the nature of aeolian sediment availability and corre-  
724 sponding modeling strategies.

725 Part IV contains appendices with specifics on the reference model, the numerical  
726 model implementation and available model settings presented in Chapter 4.



727

## Part I

728

### FIELD DATA

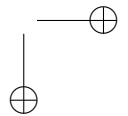
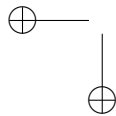
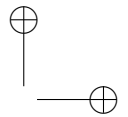
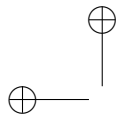
729

Field data is collected at the Sand Motor mega nourishment in The Netherlands. The Sand Motor showed a peculiar morphological development since its construction as it is permanently exposed to wind and yet its sub-aerial morphology is remarkably static.

730

731

732



# 2

733

734

## 735 LARGE SCALE SEDIMENT BUDGETS

736 *This chapter is based on a previous publication: Hoonhout, B. M. and de Vries, S. (2016a).*  
737 *Aeolian sediment supply at a mega nourishment. Coastal Engineering. Submitted.*

### 738 2.1 INTRODUCTION

739 Aeolian sediment supply is a prerequisite to growth and resilience of coastal dunes  
740 that function as a natural protection against flooding from the sea. Expanding hu-  
741 man activities in coastal areas and growing uncertainties related to climate change,  
742 increase coastal risks. Mitigation of these risks resulted in the engineering of entire  
743 coastlines (Donchyts et al., 2016). Rigid solutions and local nourishments are tradi-  
744 tional solutions to a societal demand for coastal safety (Hamm et al., 2002). With the  
745 increased confidence in our ability to mitigate coastal risks, additional demands and  
746 functions for coastal flood protections arose. Soft engineering solutions with limited  
747 environmental and ecological impact (Waterman, 2010; de Vriend et al., 2015) gained  
748 preference over rigid solutions or local nourishments. Recently, the exponent of soft  
749 engineering emerged as mega nourishments (Stive et al., 2013). Mega nourishments  
750 pursue the idea of stimulating natural sediment transport processes with the aim of  
751 increasing coastal safety. The idea is based on the assumption that the incidental or  
752 concentrated interventions necessary for the stimulation of nature are less intrusive  
753 than classic solutions to coastal safety. Moreover, mega nourishments tend to accom-  
754 modate long-term monitoring and periodic adaptation and intervention that increases  
755 flexibility with respect to planning and execution as well as the occurrence of coastal  
756 hazards. The increased flexibility can make mega nourishments also cost-effective  
757 (Van Slootbeek et al., 2013).

758 The effectiveness of a mega nourishment depends on the sediment transport path-  
759 ways from nourishment to dunes. A small fraction of the sediment moved in the  
760 nearshore ultimately arrives in the dunes (Aagaard et al., 2004). It is this small aeolian  
761 sediment supply that provides us with the natural and persistent coastal safety  
762 that mega nourishments aim for. In addition, this small aeolian sediment supply  
763 gives coastal dune systems the natural resilience to storm impacts and the conditions  
764 for survival of persistent dune vegetation that strengthens the dunes, like marram  
765 grass (Borsje et al., 2011). It is also this small aeolian sediment supply that is least  
766 understood.

767 Mega nourishments affect aeolian sediment supply to coastal dunes in various ways.  
768 First, sand used for nourishment is typically obtained from offshore borrowing pits  
769 and differs from the original beach sand in terms of size and composition, affect-

ing the erodibility of the beach (van der Wal, 1998, 2000). Second, aeolian sediment availability (following the definition of Kocurek and Lancaster, 1999) at beach nourishments that are constructed above storm surge level can be significantly reduced by deflation lag deposits (Jackson et al., 2010). The absence of regular flooding and wave-reworking allows lag deposits to develop a beach armor layer, resulting in compartmentalization of the nourishment in armored and unarmored surfaces. McKenna Neuman et al. (2012) illustrated how deflation lag deposits increase the shear velocity threshold significantly and reduce aeolian sediment availability and subsequently supply from the higher supratidal beach. Deflation lag deposits can therefore cause intertidal and low-lying supratidal beaches to gain importance over the high and dry beach as source of aeolian sediment. Third, the placement of a nourishment is known to affect nearshore processes (Grunnet and Ruessink, 2005; Ojeda et al., 2008; De Schipper et al., 2013). Synchronization between aeolian and nearshore processes, like onshore bar migration and welding, is reported to stimulate aeolian sediment supply to coastal dunes (Houser, 2009; Anthony, 2013). The importance of low-lying beaches as source of aeolian sediment might therefore also be affected by changing bar dynamics.

Jackson and Nordstrom (2011) emphasized the necessity for the quantification of the effect of large scale beach nourishment designs on aeolian sediment supply. Quantitative predictions of aeolian sediment availability and supply in coastal environments has proven to be challenging (Sherman et al., 1998; Sherman and Li, 2012). Limitations in aeolian sediment availability are often identified as reason for the discrepancy between measured and predicted sediment transport rates (Delgado-Fernandez et al., 2012; de Vries et al., 2014a; Lynch et al., 2016).

Mega nourishments inherently cause spatiotemporal variations in aeolian sediment availability. The spatial variations are caused by compartmentalization of the beach. The temporal variations are induced by adaptation of the large coastal disturbance to the wave and wind climate, resulting in changes in beach width, slope and composition (de Schipper et al., 2016). Consequently, quantification of aeolian sediment availability and supply from mega nourishments requires differentiation in space and time.

This paper presents an aeolian sediment budget analysis of the 21 Mm<sup>3</sup> Sand Motor mega nourishment based on four years of bi-monthly topographic surveys. The sediment budget analysis quantifies the net aeolian sediment supply to the dunes, dune lake and lagoon accommodated by the Sand Motor. The Sand Motor constitutes distinct areas that are either influenced by marine processes, by aeolian processes or by a combination of both. Therefore, the influence of marine and aeolian processes on aeolian sediment supply can be separated and spatiotemporal variations in aeolian sediment availability can be identified with reasonable accuracy. The observed compartmentalization of the Sand Motor is discussed in relation to limitations in aeolian sediment availability, as well as the design of mega nourishments like the Sand Motor as solution to coastal safety.

## 2.2 FIELD SITE

The Sand Motor (or Sand Engine) is an artificial 21 Mm<sup>3</sup> sandy peninsula protruding into the North Sea off the Delfland coast in The Netherlands (Figure 2.1, Stive et al.,

815 2013). The Sand Motor is an example of a mega nourishment and is intended to nourish  
816 the Holland coast for a period of two decades, while stimulating both biodiversity  
817 and recreation.

818 The Sand Motor was constructed in 2011 and its bulged shoreline initially extended  
819 about 1 km seaward and stretched over approximately 2 km along the original coast-  
820 line. The original coast was characterized by an alongshore uniform profile with a  
821 vegetated dune with an average height of 13 m and a linear beach with a 1:40 slope.  
822 The dune foot is located at a height of approximately 5 m+MSL.

823 Due to natural sediment dynamics the Sand Motor distributes about 1 Mm<sup>3</sup> of  
824 sand per year to the adjacent coasts (Figure 2.1). The majority of this sand volume  
825 is transported by tides and waves. However, the Sand Motor is constructed up to 5  
826 m+MSL and locally up to 7 m+MSL, which is in either case well above the maximum  
827 surge level of 3 m+MSL (Figure 2.2c). Therefore, the majority of the Sand Motor area  
828 is uniquely shaped by wind.

829 The Sand Motor comprises both a dune lake and a lagoon that act as large traps  
830 for aeolian sediment (Figure 2.1). The lagoon is affected by tidal forcing, although  
831 the tidal amplitude quickly diminished over time as the entry channel elongated. The  
832 tidal range of about 2 m that is present at the Sand Motor periphery (Figure 2.2c), is  
833 nowadays damped to less than 20 cm inside the lagoon (de Vries et al., 2015). Con-  
834 sequently, the tidal currents at the closed end of the lagoon, where most aeolian  
835 sediment is trapped, are negligible.

836 Sand used for construction of the Sand Motor is obtained from an offshore borrow-  
837 ing pit in the North Sea. The sand is predominantly Holocene sand with a significant  
838 amount of fines. The median grain size is slightly coarser than found originally along  
839 the Delfland coast. Apart from sand fractions, the sediment contains a large amount  
840 of shells, shell fractions, some pebbles and cobbles and an occasional fraction of a  
841 mammoth bone.

842 The dominant wind direction at the Sand Motor is south to southwest (Figure 2.2a).  
843 However, during storm conditions the wind direction tends to be southwest to north-  
844 west. During extreme storm conditions the wind direction tends to be northwest.  
845 Northwesternerly storms are typically accompanied by significant surges as the fetch is  
846 virtually unbounded to the northwest, while surges from the southwest are limited  
847 due to the presence of the narrowing of the North Sea at the Strait of Dover (Figure  
848 2.1, inset).

### 849 2.3 METHODOLOGY

850 Spatiotemporal variations in aeolian sediment supply in the Sand Motor domain are  
851 identified using an aeolian sediment budget analysis. A sediment budget analysis can  
852 be performed if frequent topographic measurements are available (Davidson-Arnott  
853 and Law, 1990) and sediment exchange over the border of the measurement domain  
854 is limited. In a sediment budget analysis the morphological change in predetermined  
855 areas are converted to volumetric changes (budgets) that are compared in a sediment  
856 volume balance.

857 A sediment budget analysis is particularly suitable for coastal sites with a complex  
858 and dynamic topography, like the Sand Motor. The use of (dense) topographic mea-  
859 surements ensures that any local variations in the topography are included. Moreover,

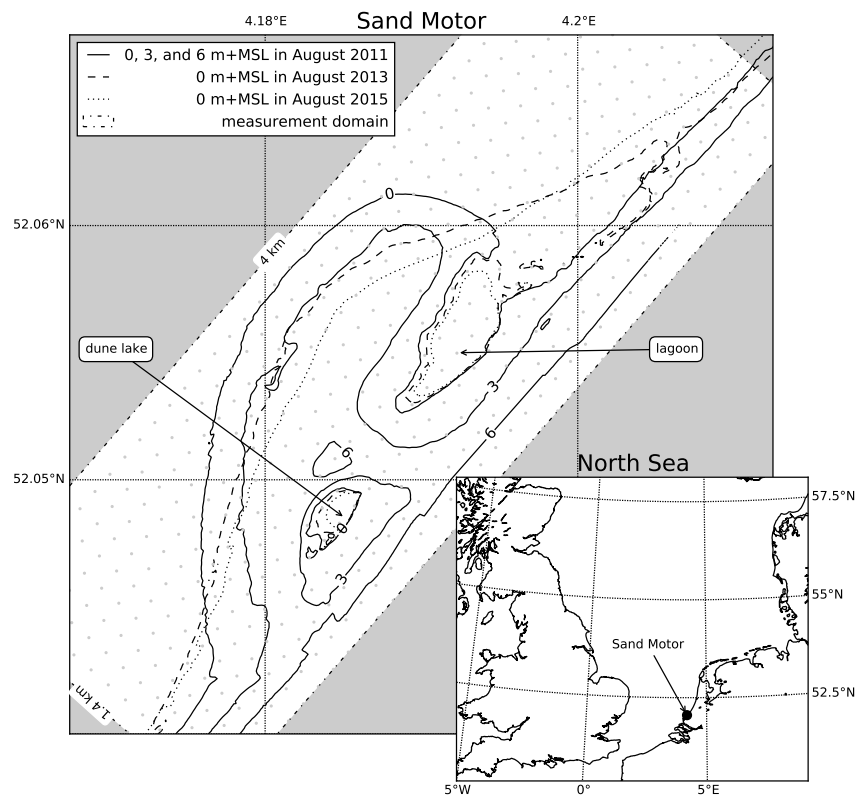


Figure 2.1: Location, orientation, appearance and evolution of the Sand Motor between construction in 2011 and 2015. The box indicates the measurement domain used in the remainder of this paper. A 100 x 100 m grid aligned with the measurement domain is plotted in gray as reference.

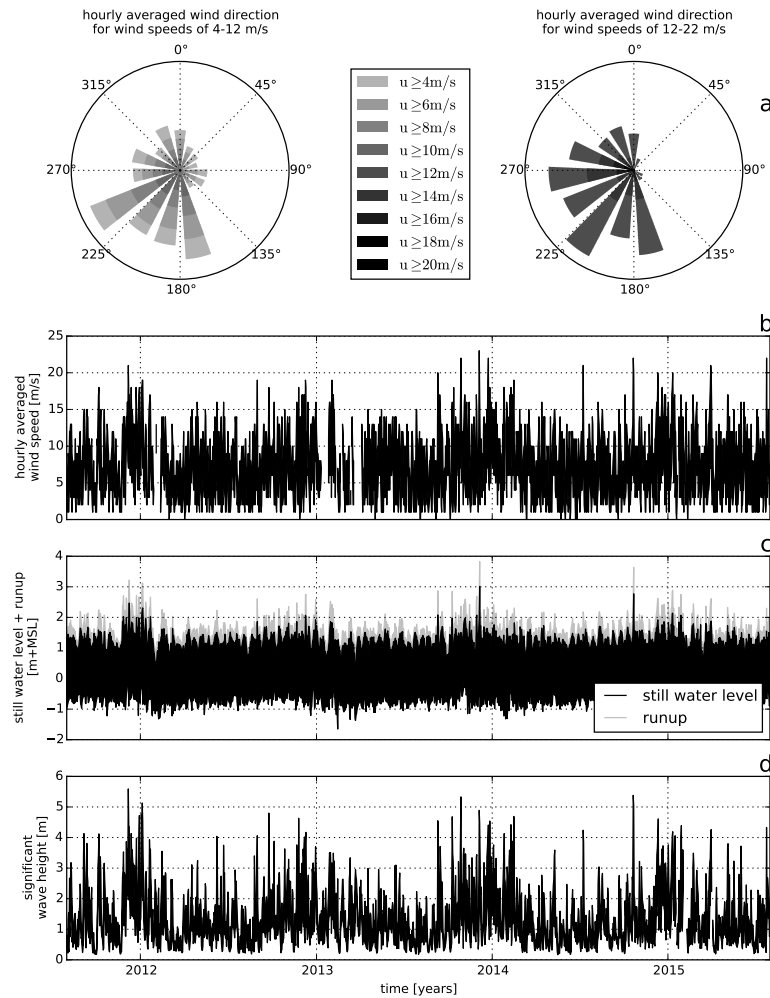


Figure 2.2: Wind and hydrodynamic time series from 2011 to 2015. Hourly averaged wind speeds and directions are obtained from the KNMI meteorological station in Hoek van Holland (upper panels). Offshore still water levels, wave heights and wave periods are obtained from the Europlatform (lower panels). Runup levels are estimated following Stockdon et al. (2006).

no assumptions on the local representativeness of the measurements are needed and the methodology is applicable to a wide range of spatial or temporal scales.

In the Sand Motor domain it is possible to separate the marine and aeolian influence on erosion and deposition of sediment directly from a sediment budget analysis. The high construction height of the Sand Motor and the absence of regular storm surges in the first four years after construction make that distinct areas exist that are either influenced by marine or aeolian processes. The sediment budgets are determined along the borders of these marine and aeolian zones.

### 2.3.1 Topographic measurements

32 topographic measurements of the Sand Motor domain obtained over a period of four years are used to determine the overall sediment budget of the Sand Motor domain (de Schipper et al., 2016). The measurement area covers 1.4 km cross-shore and 4 km alongshore (Figure 2.1). The nearshore bathymetry is surveyed using a jetski equipped with an echo sounder and RTK-GPS receiver. The topography of the Sand Motor from the waterline up to the dune foot is surveyed using an all-terrain vehicle (ATV) that is also equipped with a RTK-GPS receiver. Inundated areas that are too shallow for the jetski, like the tidal channel and the dune lake, are surveyed using a manually pushed RTK-GPS wheel. The survey is performed along cross-shore transects that are 20 m apart. The resulting trajectories are interpolated to a regular 10 m x 10 m grid for the sediment budget analysis. Surveys that show a morphological rate of change that is more than two standard deviations from the average are considered outliers. The measurements of September 4, 2011 and June 21, 2012 are discarded as outliers.

The topography in the dune area, which is not included in the RTK-GPS surveys, is monitored by airborne lidar. Half-yearly measurements from the southern Holland coast (Delfland coast) are available since 2011, prior to the construction of the Sand Motor. The lidar measurements have a spatial resolution of 2 m or 5 m. The measurements are corrected for the presence of vegetation and artificial objects, like beach pavilions, and interpolated to the same 10 m x 10 m grid and the same moments in time as the RTK-GPS measurements.

### 2.3.2 Zonation

The Sand Motor domain is divided into seven zones for the aeolian sediment budget analysis (Table 2.1 and Figure 2.3). The zonation aims to separate areas with marine influences from areas without marine influences, and separate areas with net aeolian erosion from areas with net aeolian deposition.

The zonation is based on the 0 m+MSL, 3 m+MSL and 5 m+MSL contour lines that roughly correspond to mean sea level, the edge of the berm or maximum runup level (Figure 2.2c) and the dune foot respectively. The contours are determined such that the spatial variance in the bed level change of the zones is minimized. The minimization ensures that the optimal division between erosion and deposition areas is found. Moreover, the 3 m+MSL and 5 m+MSL contour lines have been relatively static since construction of the Sand Motor.

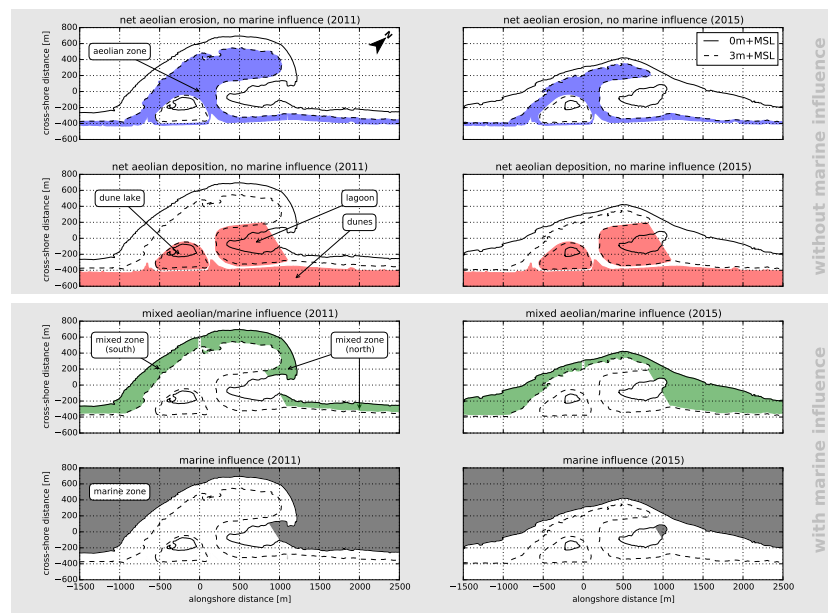


Figure 2.3: Zonation of the Sand Motor domain into zones with net aeolian erosion and no marine influence, net aeolian deposition and no marine influence, mixed aeolian/marine influence and marine influence. Left panels: 2011. Right panels: 2015.

Table 2.1: Zonation of the Sand Motor domain into seven zones with and without marine influence. See also Figure 2.3.

<i>without</i> marine influence	<i>with</i> marine influence
aeolian zone	mixed zone (north)
dunes	mixed zone (south)
dune lake	marine zone
lagoon	

902 To ensure a constant shape and size of the zones during the analysis, the convex  
 903 hull of all 3 m+MSL contour lines is used as zone boundary for the lake and lagoon.  
 904 Also for the dunes minimal variations over time in zone shape and size are removed  
 905 by using the most seaward position of all contour lines. Consequently, only the ae-  
 906 olian zone and mixed zones change in shape and size over time. The volumetric  
 907 change between two consecutive measurements is determined for these zones within  
 908 the smaller contour:

$$\Delta V^n = \hat{A}_c \cdot (\bar{z}_b^n - \bar{z}_b^{n-1}) \quad \text{where } \hat{A}_c = \min(A_c^n; A_c^{n-1}) \quad (2.1)$$

909 with  $\Delta V^n$  the volume change,  $A_c^n$  the surface area of the zone and  $\bar{z}_b^n$  the average  
 910 bed level in the zone, all in time interval  $n$ . The (cumulative) sum over all time  
 911 intervals of the volume changes in each zone is used in the analysis. By using the  
 912 smaller of two contours in a comparison, a part of the larger contour is neglected:

$$A_{c,\text{neglected}}^n = \max(A_c^n; A_c^{n-1}) - \hat{A}_c \quad (2.2)$$

913 The neglected area of the zone with the largest change in size, the aeolian zone, is on  
 914 average 2% and never larger than 8%.

### 915 2.3.3 Spatial variations in porosity

916 The change in sediment volume is susceptible to changes in porosity. In order to  
 917 relate the changes in sediment volume to the transport of sediment mass, variations  
 918 in porosity need to be accounted for. Porosity values in the Sand Motor domain are  
 919 obtained from core samples and used to account for the spatial variations in porosity.  
 920 The core samples have a diameter of 8 cm and depth of 10 cm from the bed surface  
 921 in an attempt to capture the porosity in the aeolian active layer of the bed. Each  
 922 sample is dried and submerged in water to determine the porosity. For comparison,  
 923 all presented sediment volumes in this paper are converted to a hypothetical porosity  
 924 of 40% according to:

$$V_{40\%} = V \cdot \frac{1-p}{1-40\%} \quad (2.3)$$

925 where  $V$  [ $\text{m}^3$ ] is the measured sediment volume and  $p$  [-] the porosity.

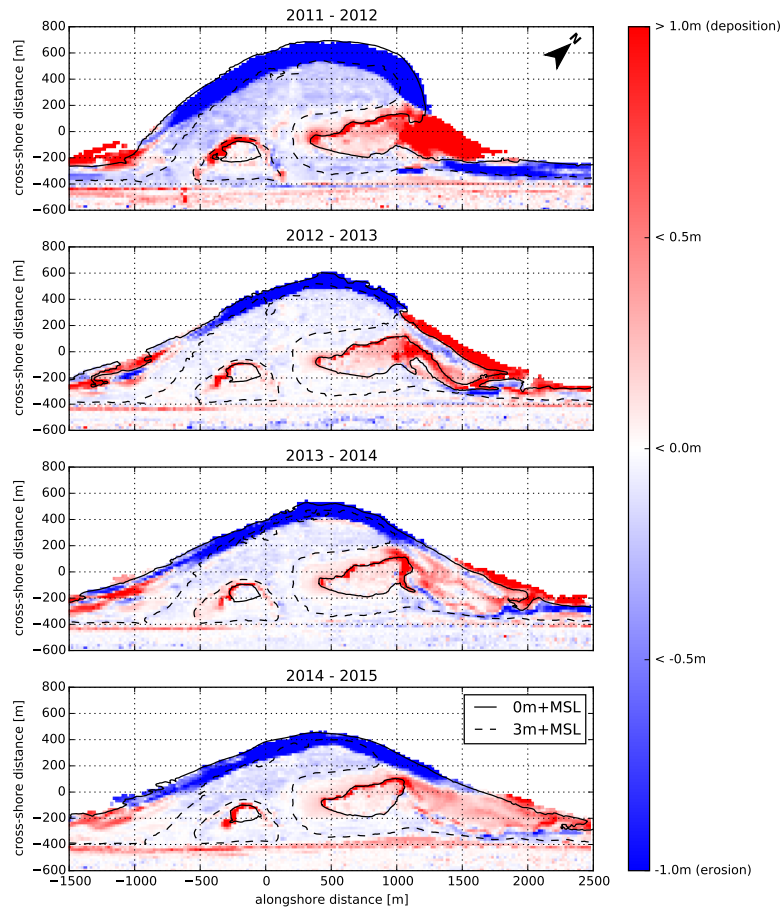


Figure 2.4: Yearly sedimentation and erosion above 0 m+MSL in the Sand Motor domain. Comparisons are made between the September surveys of each year.

Table 2.2: Measured porosity values in the Sand Motor domain. Each area is sampled at three different locations. The results per area are presented in ascending order. The last column presents the average porosity for each area that is used to convert the sediment volumes presented in this paper to a hypothetical porosity of 40%.

Area	Porosity		
	min.	max.	avg.
Aeolian zone	39.0%	39.4%	40.2%
Mixed zone (north)	38.4%	39.8%	40.8%
Mixed zone (south)	37.1%	38.4%	38.4%
Dunes	36.1%	36.3%	37.1%
Dune lake	34.7%	34.9%	36.3%
Lagoon	46.3%	47.3%	49.0%
			47.6%

926 2.4 RESULTS

927 The overall sediment budget of the Sand Motor domain is determined given mor-  
 928 phological change in the net aeolian erosion and net aeolian deposition zones for the  
 929 period between September 1, 2011 and September 1, 2015 (Figure 2.4).

930 2.4.1 *Morphological change and porosity*

931 The net morphological change within the 3 m+MSL contour can be accredited en-  
 932 tirely to aeolian sediment transport as this area is not significantly affected by marine  
 933 processes since the construction of the Sand Motor. Also the net contribution of along-  
 934 shore sediment fluxes are assumed to be relatively small given that the beach width  
 935 (< 100 m) is small compared to the alongshore span of the measurement domain (4  
 936 km). Within the 3 m+MSL contour sediment is deposited in the dunes and eroded  
 937 from the aeolian zone.

938 The morphological change in the dune lake and the closed end of the lagoon is  
 939 assumed to be driven predominantly by wind. Hydrodynamic forcing and conse-  
 940 quently marine deposits in these zones diminished quickly over time, while significant  
 941 amounts of fine aeolian deposits are found along the southwestern to northwestern  
 942 shores.

943 The aeolian contribution to the morphological change in the mixed zones cannot be  
 944 determined directly due to the presence of both marine and aeolian forces. However,  
 945 by balancing the changes in sediment volume in the net aeolian deposition zones with  
 946 the changes in sediment volume in the net aeolian erosion zones the aeolian sediment  
 947 supply from the mixed zones is estimated.

948 18 porosity measurements from six zones (Table 2.2) are used to convert all mea-  
 949 sured sediment volumes to a hypothetical porosity of 40%.

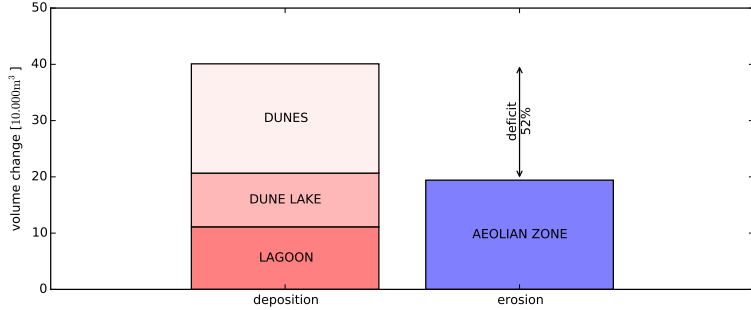


Figure 2.5: Aeolian sediment budgets in the Sand Motor domain in the period between September 1, 2011 and September 1, 2015.

#### 950 2.4.2 Aeolian sediment budgets

951 The aeolian zone consistently provides less sediment than is deposited in the dunes,  
 952 dune lake and lagoon (Figure 2.5). Over the four years since construction of the  
 953 Sand Motor the volume deficit accumulates to  $21 \cdot 10^4 \text{ m}^3$ , which is 52% of the total  
 954 sediment accumulation of  $40 \cdot 10^4 \text{ m}^3$ . The total wind transport capacity (or cumulative  
 955 theoretical sediment transport volume) in this period is roughly estimated as  
 956  $110 \cdot 10^4 \text{ m}^3$  (Appendix A). As the actual sediment transport rates appear to be only  
 957 about 35% of the wind transport capacity, the Sand Motor can be classified as an  
 958 availability-limited system.

959 Late January 2012, the surveys show a net volume deficit of zero, while subsequent  
 960 surveys show a more or less linear growth of the volume deficit (Figure 2.6). Fitting  
 961 a linear trend reveals an average growth rate of  $5.2 \cdot 10^4 \text{ m}^3/\text{yr}$ , which is 67% of  
 962 the total sediment accumulation rate of  $7.7 \cdot 10^4 \text{ m}^3/\text{yr}$  ( $R^2 = 0.96$ ). The increase  
 963 in growth rate of the volume deficit is likely caused by a significant decrease of the  
 964 sediment contribution from the aeolian zone. The erosion from the aeolian zone in  
 965 the first half year after construction of the Sand Motor exceeds the total erosion in the  
 966 four years thereafter, while sediment continued to be accumulated in the dunes, dune  
 967 lake and lagoon. The surface area of the aeolian zone decreased continuously (Figure  
 968 2.7).

969 The diminishing of the aeolian sediment supply from the aeolian zone is also re-  
 970 flected in the average bed level within the 3 m+MSL contour of September 22, 2015  
 971 (Figure 2.8). The bed level within this contour has been almost constant since the  
 972 volume deficit started to grow steadily from late January 2012. Only a few periods  
 973 of significant erosion can be distinguished that can be related to storm events. Most  
 974 notably, the event of December 5, 2013 with wind speeds up to 34 m/s. That day  
 975  $1.5 \cdot 10^4 \text{ m}^3$  of sediment was eroded from within the 3 m+MSL contour of Septem-  
 976 ber 22, 2015, which is 52% of the total erosion that year. Although this event is among  
 977 the few events during which the runup levels exceeded the 3 m+MSL level (Figure  
 978 2.2), the erosion can still be accredited to wind as the 3 m+MSL contour of September  
 979 22, 2015 was located about 100 m landward of the 3 m+MSL contour at the time of the

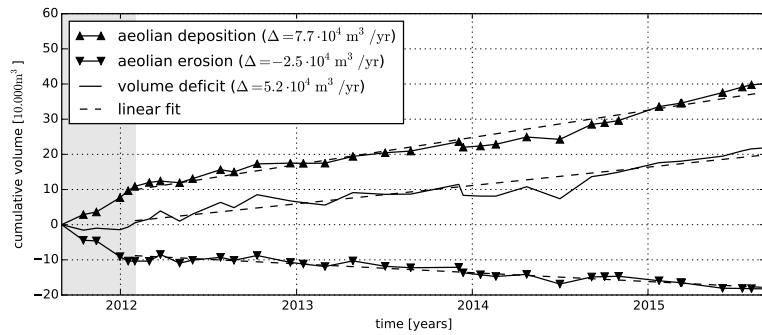


Figure 2.6: Cumulative change in sediment volume of all net aeolian erosion and net aeolian deposition zones and the volume deficit. For the linear fit the period prior to February 2012 is discarded (shaded).

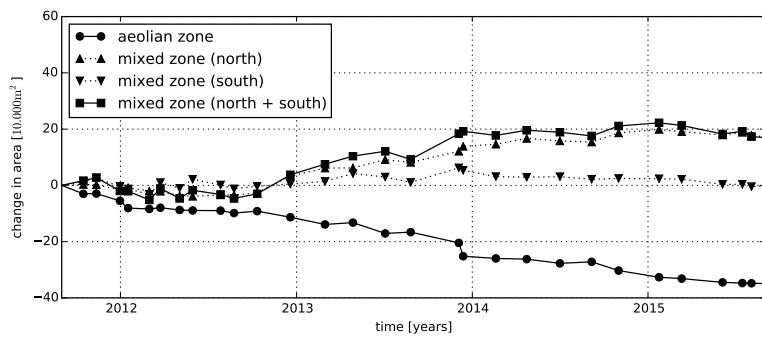


Figure 2.7: Change in size of aeolian zone and mixed zones since construction of the Sand Motor in 2011.

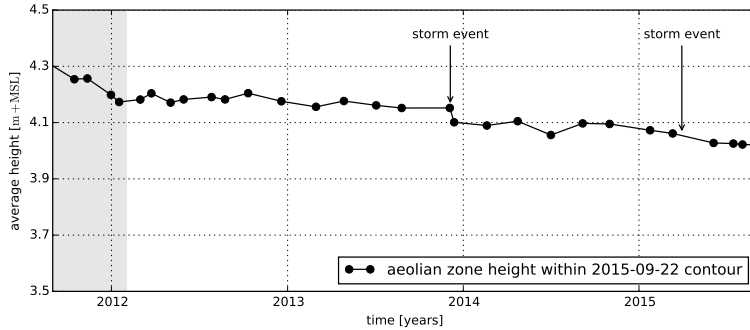


Figure 2.8: Average height of the aeolian zone in the most recent contour.

980 storm event. Therefore the bed level in the more recent contour was not affected by  
981 the surge, which is confirmed by observations from a local permanent camera station.

982 In general, the use of the 3 m+MSL contour as divide between the areas with and  
983 without marine influence appears to be valid for almost the entire four years after  
984 construction of the Sand Motor. Only four events have been registered in which runup  
985 levels exceeded the 3 m+MSL level (Figure 2.2). Observations from a local permanent  
986 camera station indicate that only during the event of December 5, 2013 the surface of  
987 the aeolian zone was significantly affected by tides and waves. Pre- and post-storm  
988 topographic surveys that are available for this event indicate that the marine erosion  
989 from the flooded areas above the 3 m+MSL level was less than  $1 \cdot 10^4 \text{ m}^3$ .

#### 990 2.4.3 Alongshore variation

991 The sediment deposits in the dunes show an alongshore variation. A depression in  
992 dune growth is observed in the lee of the dune lake and lagoon (Figure 2.9). South of  
993 the dune lake and in between the dune lake and lagoon a passage for aeolian sediment  
994 transport is present, which seems to result in a locally elevated dune growth. The  
995 average dune growth of  $14 \text{ m}^3/\text{m}/\text{yr}$  in the Sand Motor domain is low compared to  
996 the dune growth rate along the adjacent southern ( $15 \text{ m}^3/\text{m}/\text{yr}$ ) and northern ( $19 \text{ m}^3/\text{m}/\text{yr}$ )  
997 beach stretches. However, aeolian deposits in the dune lake and lagoon  
998 are of the same order of magnitude resulting in a total average sediment deposition of  
999  $27 \text{ m}^3/\text{m}/\text{yr}$  in the Sand Motor domain, which is on average 56% higher than along  
1000 the adjacent coasts.

## 1001 2.5 DISCUSSION

1002 The volume deficit between the net aeolian erosion and net aeolian deposition zones  
1003 can be accredited to the mixed zones that are affected by both marine and aeolian  
1004 processes. The mixed zones in the Sand Motor domain are consequently estimated to  
1005 provide 67% of the aeolian sediment in the Sand Motor domain. The aeolian sediment  
1006 supply from the mixed zones is therefore significant, but still small compared to the

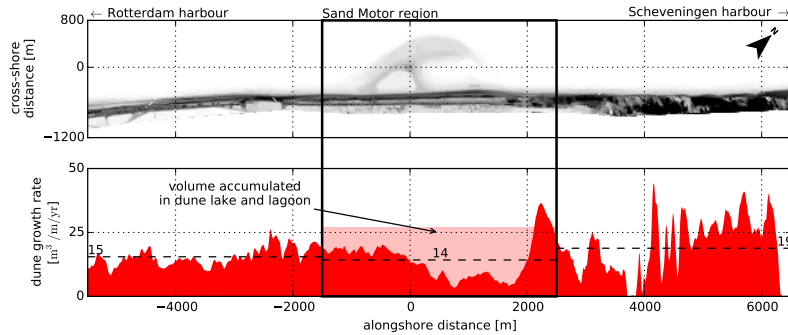


Figure 2.9: Comparison sediment accumulation rates in dunes ( $>3$  m+MSL) for Sand Motor domain and adjacent coasts. Airborne lidar measurements from January 2012 until January 2015 are used. Horizontal dashed lines indicate local averages. The box indicates the Sand Motor domain depicted in previous figures.

98% reported by Jackson et al. (2010). The importance of the mixed zone cannot be explained by the size of the surface area as the mixed zones are initially smaller than the other main sediment source: the aeolian zone (Figure 2.7). Only from 2013 onward the surface area of the mixed zones exceed the area of the aeolian zone. However, the increase in surface area of the mixed zones is concentrated in the north where a low-lying spit develops (Figure 2.4). Given the dominant south to southwesterly wind direction and their position with respect to the lagoon that separates the spit from the dunes, it is unlikely that these intertidal beaches, provide a significant amount of sediment to dunes, dune lake and lagoon. Therefore, despite the periodic flooding and a size that is 40% – 60% smaller than the aeolian zone, the mixed zone (south) appears to provide the majority of the aeolian sediment in the Sand Motor domain.

#### 2.5.1 Sources of inaccuracies

By accrediting the volume deficit to the mixed zones it is assumed that no sediment is exchanged over the boundaries of the Sand Motor domain and the sediment volume balance is thus closed. This assumption is not strictly valid, but the external sediment exchange with the Sand Motor domain is limited compared to the total sediment accumulation of  $40 \cdot 10^4$  m<sup>3</sup>.

The predominantly southwesterly wind direction might blow sediment over the lateral borders that is not taken into account. However, the net alongshore sediment supply to the Sand Motor domain is estimated to be two orders smaller than the net onshore sediment supply, or less than 1% of the total sediment accumulation (Figure 2.10), because:

1. The onshore and alongshore sediment flux *per meter width* are estimated to be of the same order of magnitude (Appendix A), but the lateral beach cross-section (< 100 m) through which the alongshore flux enters the Sand Motor domain

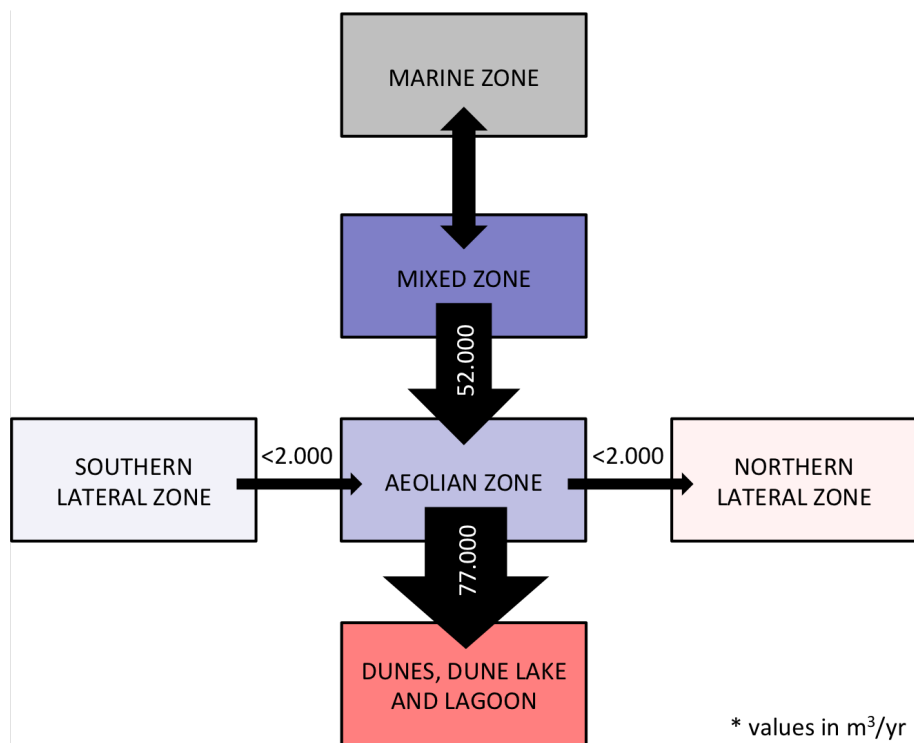


Figure 2.10: Aeolian sediment budget analysis of the Sand Motor

at the southern border is an order of magnitude smaller than the alongshore span of the Sand Motor domain (4 km) through which the onshore flux enters the domain. Therefore, the absolute alongshore contribution to the total sediment volume balance is likely an order of magnitude smaller than the onshore contribution.

2. The contribution of the net alongshore sediment flux that enters the Sand Motor domain at the southern border is at least partially compensated by a net alongshore sediment flux of the same order of magnitude that leaves the domain at the northern border. Therefore, the contribution to the total sediment volume balance of the southern and northern alongshore sediment fluxes combined (alongshore sediment transport gradient) is likely two orders of magnitude smaller than the contribution of the onshore sediment flux.

In reality the contribution of the alongshore sediment fluxes is likely to be even smaller as the sediment fluxes can locally be more onshore directed due to local wind steering. In addition, the estimates of the order of magnitude of the sediment fluxes are likely to be overestimated as possible limitations in sediment availability are ignored.

The influence of marine deposits in the lagoon is estimated to be less than 4% of the total sediment accumulation. 85% of the deposited sediment in the lagoon has the form of a southwesterly infill protruding above water and consisting of loosely packed, fine sediment and is therefore likely from aeolian origin (Figure 2.4 and Table 2.2). 15% of the deposited sediment in the lagoon, or 4% of the total sediment accumulation, is spread over a wider area and is possibly from marine origin.

The influence of marine erosion of the aeolian zone during the limited number of storm surges is estimated to be less than  $1 \cdot 10^4 \text{ m}^3$  (Section 2.4.2), or 2.5% of the total sediment accumulation. Similarly, the influence of the changing size of the aeolian zone is estimated to be 2% of the total erosion in this area (Section 2.3.2), or less than 1% of the total sediment accumulation.

In summary, the error that is introduced by assuming a closed sediment volume balance is estimated to be less than 9% of the total sediment accumulation. The volume deficit of 67% of the total sediment accumulation that is accredited to aeolian erosion from the mixed zones therefore needs to be nuanced and is estimated to be 58% – 76%.

### 2.5.2 Beach armoring

The relative importance of the mixed zones for aeolian sediment supply can likely be explained by a visually observed beach armor layer that developed in the aeolian zone since construction of the Sand Motor. A beach armor layer can reduce the availability of aeolian sediment significantly (McKenna Neuman et al., 2012). Because the Sand Motor was constructed several meters above common storm surge level, the aeolian zone has never been influenced by waves or tides. Consequently, no process is present that regularly resets the armor layer, except for the occasional high-energy wind event. Moreover, salt crusts that form due to salt spray have a similar effect on the sediment availability as an armor layer. Small concentrations of salt ( $\leq 7 \text{ mg/g}$ ) can already reduce the sediment availability by a factor two (Nickling and Ecclestone, 1981).

1076 In contrast, no beach armor layer or salt crusts develop in the mixed zones as pe-  
1077 riodic flooding and related wave-reworking regularly deposit marine sediments, mix  
1078 the top layer of the bed, and wash shells and shell fragments away. In addition,  
1079 onshore bar migration and welding periodically provide additional unarmored sed-  
1080 iment that can be entrained by the wind during low water (Houser, 2009; Anthony,  
1081 2013). However, aeolian sediment availability in the mixed zones is also limited due  
1082 to the relatively high soil moisture contents in these areas. Also soil moisture content  
1083 is known to increase the shear velocity threshold (Wiggs et al., 2004; Edwards and  
1084 Namikas, 2009; Namikas et al., 2010) and limit the local aeolian sediment availability.  
1085 Given that the mixed zones appear to be a more important supplier of aeolian sedi-  
1086 ment than the aeolian zone, limitations in sediment availability due to beach armoring  
1087 seems to outweigh limitations due to high moisture contents.

1088 During a storm event even shell fragments and shells can be mobilized. Conse-  
1089 quently, the beach armor layer itself might be transported and its reducing effect on  
1090 the sediment availability is (partially) neutralized. Storm events are regularly accom-  
1091 panied with surges that prevent wind erosion of the mixed zones. Entrainment of  
1092 sediment therefore starts at a relatively high point along the fetch and much of the  
1093 sediment transport capacity can be used for erosion of the aeolian zone, which con-  
1094 tributes to the removal of the beach armor layer. If the surge is high enough it can  
1095 also remove the beach armor layer by wave action or bury it by deposition of marine  
1096 sediments. The removal or burial of the beach armor layer can elevate sediment avail-  
1097 ability from the aeolian zone also after the the storm passed. Only after development  
1098 of a new beach armor layer the sediment availability and transport rates approach the  
1099 pre-storm situation.

#### 1100 2.5.3 *Mega nourishments as coastal protection*

1101 The Sand Motor mega nourishment shows a morphological development that is signif-  
1102 icantly different from natural beaches or the original Delfland coast. Aeolian sediment  
1103 supply at the Sand Motor shows larger spatial variations compared to natural beaches,  
1104 while dune growth rates lag behind compared to the adjacent coastal stretches. It can  
1105 be questioned if such exotic behavior is desired for a coastal protection that aims  
1106 to stimulate natural processes, or that, for example, it would be beneficial not to  
1107 construct future mega nourishments above local storm surge level and prevent com-  
1108 partmentalization of the beach.

1109 In this context, it is interesting to consider what would happen if the Sand Motor  
1110 was constructed up to local storm surge level (3 m+MSL). The vast aeolian zone would  
1111 not exist as the entire Sand Motor would be flooded at least once a year. Compart-  
1112 mentalization would be minimized and aeolian sediment availability be maximized as  
1113 the formation of deflation lag deposits is counteracted by wave-reworking. The dune  
1114 lake and lagoon would be filled in up to three times faster due to transport-limited  
1115 aeolian sediment supply. Soon, all aeolian sediment transport pathways would end  
1116 in the dunes, resulting in an up to six times larger dune growth than currently ob-  
1117 served. Marine sediment transport would enhance these relatively rapid changes as  
1118 more sediment is redistributed within the Sand Motor domain to the lagoon, dune  
1119 lake and offshore by overwash.

1120 A lower construction height of the Sand Motor would therefore result in a more  
1121 rapid and more localized redistribution of sediment. Both rapid and localized redis-  
1122 tribution are at odds with the purpose of the Sand Motor to nourish the entire Holland  
1123 coast over a period of two decades. The static behavior of the supratidal areas of Sand  
1124 Motor might therefore prove to be a crucial design criterion of a mega nourishment.

1125 **2.6 CONCLUSIONS**

1126 A sediment budget analysis is used to identify spatial variations in aeolian sediment  
1127 deposition and supply, and dune growth in the Sand Motor domain. From the analy-  
1128 sis the following conclusions can be drawn regarding aeolian sediment transport and  
1129 supply in the Sand Motor domain:

- 1130 1. The (southern) low-lying beaches that are affected by both aeolian and marine  
1131 processes (mixed zone) currently supply 58% – 76% of all aeolian sediment  
1132 deposits in the Sand Motor domain, despite that this area is periodically flooded  
1133 and 40% – 60% smaller than the upper dry beach areas (aeolian zone) that are  
1134 only affected by aeolian processes and supply the other 24% – 42% of the aeolian  
1135 deposits;
- 1136 2. The aeolian sediment supply from the aeolian zone diminished in the first half  
1137 year after construction of the Sand Motor, likely due to the development of a  
1138 beach armor layer;
- 1139 3. The aeolian sediment supply from the aeolian zone tends to increase temporar-  
1140 ily during and after a storm event, likely due to (partial) removal of the beach  
1141 armor layer;
- 1142 4. The dune growth in the Sand Motor domain is low compared to the adjacent  
1143 coasts, likely due to blocking of aeolian sediment transport pathways by the  
1144 dune lake and lagoon.

1145 From the analysis the following conclusions can be drawn regarding mega nourish-  
1146 ments in general:

- 1147 1. The construction height should be a design criterion of any mega nourishment  
1148 as it governs compartmentalization of the beach due to beach armoring;
- 1149 2. Compartmentalization of the beach can influence the lifetime and region of in-  
1150 fluence of a mega nourishment as it affects the balance between local aeolian  
1151 deposition and regional marine spreading of sediment.
- 1152 3. The consequences of compartmentalization is not yet fully understood as the  
1153 contribution of the upper dry beach (aeolian zone) to local aeolian sediment  
1154 supply can range from 42% as observed at the Sand Motor to less than 2% as  
1155 reported by Jackson et al. (2010).

# 3

1156

1157

---

## 1158 SMALL SCALE SEDIMENT TRANSPORT

---

1159 This chapter is based on a previous publication: Hoonhout, B. M. and de Vries, S. (2016c).  
1160 Field measurements on spatial variations in aeolian sediment availability at the sand motor  
1161 mega nourishment. Aeolian Research. Submitted.

1162 **3.1 INTRODUCTION**

1163 The Sand Motor (or Sand Engine) is a innovative solution to counter act the anticipated  
1164 coastal recession due to sea level rise (Stive et al., 2013). The Sand Motor is a 21  
1165 Mm<sup>3</sup> mega nourishment along the Dutch coast that is constructed well above storm  
1166 surge level and therefore largely shaped by wind. While the Sand Motor accommodates  
1167 fetches up to 1.0 km and is permanently exposed to wind, the dry surface  
1168 area is remarkably stable (Hoonhout and de Vries, 2016a). An armor layer consisting  
1169 of shells, pebbles and cobbles prevent erosion by wind and thus limit the sediment  
1170 availability (following the definition of Kocurek and Lancaster, 1999). Consequently,  
1171 the aeolian sediment transport rates at the Sand Motor are limited to approximately  
1172 25% of the wind transport capacity (Hoonhout and de Vries, 2016a) making the Sand  
1173 Motor an availability-limited coastal system.

1174 In an availability-limited coastal system, not the wind transport capacity, but the  
1175 sediment availability governs the sediment supply towards the dunes. Sediment  
1176 availability can be limited by various bed surface properties, like shells, salt crusts,  
1177 moisture and vegetation. Studies on the influence of bed surface properties on aeolian  
1178 sediment availability and transport started as wind tunnel experiments (e.g. Belly,  
1179 1964; Howard, 1977; Dyer, 1986; Gillette and Stockton, 1989). These studies typically  
1180 determine an adapted threshold velocity that relates the theoretical wind transport  
1181 capacity to a measured sediment transport capacity (Bagnold, 1937a). In the field, the  
1182 influence of different bed surface properties on sediment availability cannot easily be  
1183 distinguished and the sediment availability is often presented spatially aggregated  
1184 sediment supply in terms of critical fetch (e.g. Jackson and Cooper, 1999; Davidson-  
1185 Arnott et al., 2005, 2008; Bauer et al., 2009). The critical fetch is the distance over  
1186 which the saltation cascade develops and aeolian sediment transport becomes saturated  
1187 (Bauer and Davidson-Arnott, 2002). Since the saltation cascade develops slower  
1188 when sediment is scarce, the critical fetch is inversely proportional to the sediment  
1189 supply (Delgado-Fernandez, 2010).

1190 Expressing the sediment supply in terms of critical fetch assumes that saturated  
1191 transport is reached if the available fetch is sufficient. Hoonhout and de Vries (2016a)  
1192 showed that sediment supply can be severely limited even with fetches as large as

1193 at the Sand Motor. Consequently, critical fetches may become very large or even un-  
 1194 defined and the definition and interpretation of the critical fetch impractical (Lynch  
 1195 et al., 2016; de Vries et al., 2014a). Moreover, significant spatial variations in sediment  
 1196 supply were found in the Sand Motor region that challenges the spatial aggregation of  
 1197 sediment availability. Alternatively, aeolian sediment transport is expressed in terms  
 1198 of local sediment availability without the need for spatial aggregation. Such approach  
 1199 would require detailed measurements on spatiotemporal variations in aeolian sedi-  
 1200 ment availability.

1201 This paper presents detailed measurements of aeolian sediment transport rates  
 1202 from the Sand Motor during a six week field campaign in the fall of 2014. Spatial  
 1203 differences in sediment transport rates reveal the main erosion and deposition areas  
 1204 of aeolian sediment. Local variations in sediment availability influence the aeolian  
 1205 sediment supply and consequently aeolian sediment transport. Temporal variations  
 1206 in aeolian sediment transport are therefore expected to be correlated with the wind  
 1207 speed, but spatial variations are expected to be correlated with local variations in  
 1208 sediment availability. Understanding local sediment availability ultimately helps im-  
 1209 proving gross aeolian sediment transport rate in availability-limited coastal systems.

### 1210 3.2 FIELD SITE

1211 The Sand Motor mega nourishment was constructed in 2011 along the Delfland coast  
 1212 in The Netherlands (Figure 3.1, Stive et al., 2013). The Delfland coast was originally  
 1213 characterized by an alongshore uniform profile with an average dune height of 13 m,  
 1214 a dune foot at about 5 m+MSL and a beach slope of about 1:40.

1215 The Sand Motor is constructed as a 21 Mm<sup>3</sup> hook-shaped peninsula that initially  
 1216 protruded about 1 km into the sea and stretched over approximately 2 km alongshore.  
 1217 The original crest height of the Sand Motor was on average about 5 m+MSL and lo-  
 1218 cally 7 m+MSL; both are well above common surge level. Consequently, a significant  
 1219 part of the Sand Motor is uniquely shaped by aeolian processes that redistribute sig-  
 1220 nificant amounts of sediments within the Sand Motor region (Hoonhout and de Vries,  
 1221 2016a).

1222 Sand used for construction of the Sand Motor is medium sand with a median di-  
 1223 ameter of about 350 µm. The sand is obtained from an offshore borrowing pit in  
 1224 the North Sea and contains many shells and some pebbles, cobbles and other non-  
 1225 erodible material.

1226 The predominant wind direction is south to southwest. Storms have a tendency to  
 1227 be oriented either southwest or northwest. Also the sediment transport potential ( $\Psi$ ),  
 1228 defined as:

$$\Psi \propto \int u^3 dt \quad (3.1)$$

1229 in which  $u$  is the wind speed, is predominantly southwesterly or northwesterly ori-  
 1230 ented. The northwesterly storms are generally accompanied with significant surges  
 1231 as the North Sea is virtually unbounded in northwesterly direction (Figure 3.1, inset).

1232 The contour of the Sand Motor changed significantly in the four years after con-  
 1233 struction. Tidal forces diffuse about 1 Mm<sup>3</sup> per year along the coast (de Schipper

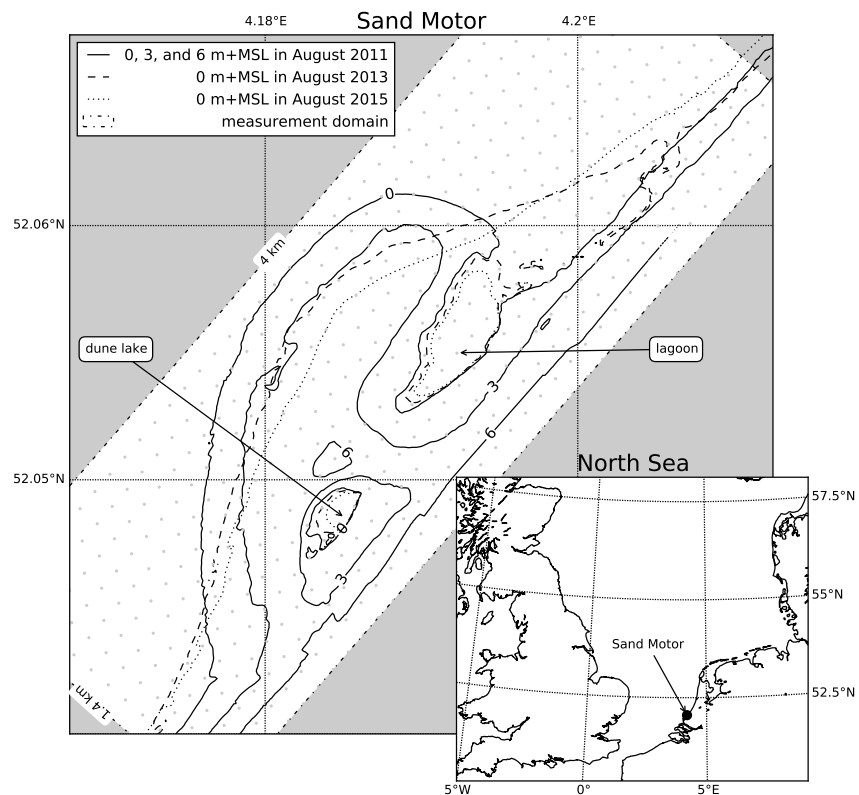


Figure 3.1: Location, orientation, appearance and evolution of the Sand Motor between construction 2011 and 2015. The box indicates the measurement domain used in the remainder of this paper. A 100 x 100 m grid aligned with the measurement domain is plotted in gray as reference.

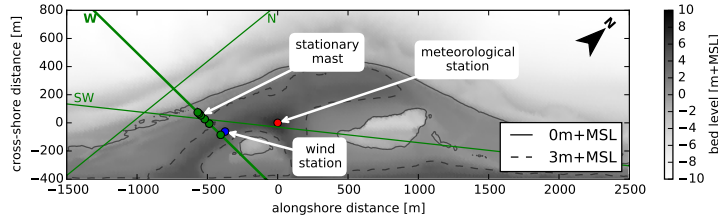


Figure 3.2: Overview of measurement transects N, W, and SW and locations during the MEGAPEX field campaign.

et al., 2016). Four years after construction, the peninsula protrudes about 800 m into the sea and stretches over 4 km alongshore (Figure 3.1).

The Sand Motor provides a unique opportunity to perform measurements on spatial variations in aeolian sediment availability and transport. It accommodates vast and armored beaches next to dynamic intertidal beaches of varying width, while limitations in fetch are negligible.

### 1240 3.3 METHODOLOGY

1241 Sediment transport measurements were performed to investigate the role of the south-  
 1242 ern intertidal beaches as supplier of aeolian sediment in the Sand Motor region  
 1243 (Hoonhout and de Vries, 2016a). The change in sediment transport in downwind  
 1244 direction (spatial gradient) was measured along cross-shore transects running from  
 1245 the water line until the dry beach at approximately 5 m+MSL. Spatial gradients in  
 1246 saltation transport are positive in areas with net erosion and negative in areas with  
 1247 net deposition of sediment. The measurements were performed during the six week  
 1248 field campaign MEGAPEX (Mega Perturbation EXperiment) from September 17, 2014  
 1249 until October 23, 2014.

#### 1250 3.3.1 Equipment

1251 The measurement set-up consists of 8 masts with battery power and data log-  
 1252 gers. Each mast was equipped with at least three Wenglor fork laser sensors (P/N:  
 1253 YHo8PCT8) for saltation measurements at 3, 10 and 25 cm above the bed (Figure 3.3).  
 1254 The lowest sensor was buried as to minimize the disturbance of the wind field. An  
 1255 additional three laser sensors were added to the most landward mast at 40, 55 and  
 1256 70 cm above the bed to estimate the amount of particles surpassing the lower three  
 1257 sensors. Other masts could be equipped with three additional laser sensors as well.  
 1258 The Wenglor fork laser sensors register passing particles of 50 µm and larger with a  
 1259 frequency of 10 kHz using a laser beam of 0.6 mm. As the particle count is linearly

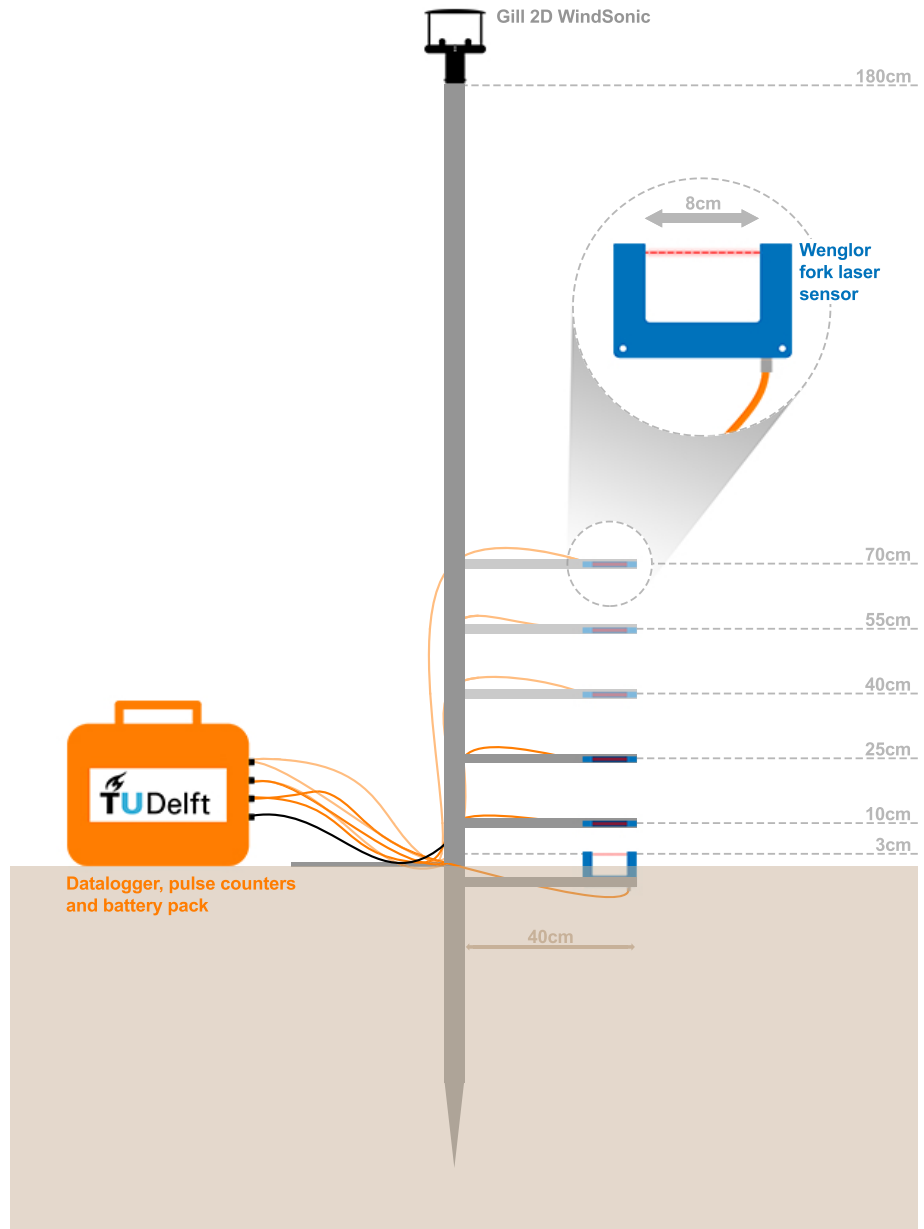


Figure 3.3: Mast with 6 Wenglor fork laser sensors and a Gill 2D WindSonic ultrasonic wind speed and direction sensor. The top 3 laser sensors are optional.

related to the sediment flux (Barchyn et al., 2014a), both are used indiscriminately in this study. The particle count is accumulated by a HOBO pulse counter (P/N: S-UCC-Moo1). A HOBO Energy data logger (P/N: H22-001) logged all sensors, including the pulse counters, at 1 Hz. In addition, three masts were equipped with a Gill 2D WindSonic ultrasonic wind speed and direction sensor (P/N: 1405-PK-040) at a height of 180 cm above the bed.

The masts can be rotated, but are not self-rotating to the wind as the masts were relocated depending on the wind direction. One stationary mast was present during almost the entire field campaign (Figure 3.2).

A separate Eijkelkamp wind station with three cup anemometers (P/N: 16.98.31) at heights 50, 100 and 180 cm and a wind vane (P/N: 16.98.34) at height 180 cm was present at a stationary location at the high beach for the entire duration of the field campaign. A Campbell Scientific meteorological station was present at the heart of the Sand Motor providing measurements on precipitation, humidity, solar radiation and wind speed and direction (Figure 3.2).

Qualitative small scale measurements on bed level change were performed by pressing erosion pins (nails) in the beach with falling tide. The erosion pins were placed along a cross-shore transect and about 10 cm apart with their heads flush to the bed. The erosion around the pins was measured manually with a ruler at the onset of flood.

Daily topographic surveys are performed along cross-shore transects using a Leica Viva GS10 RTG-GPS receiver. Offshore water levels and wave heights are obtained from gauges at the permanent offshore Europlatform.

### 3.3.2 Deployments

The measurement masts were deployed continuously during the field campaign, but have been relocated according to the governing wind direction. An overview of the measurement locations is given in Figure 3.2.

A single measurement transect consists of at least four masts: two in the intertidal beach area in order to capture the entrainment rate from the assumed sediment source region, one above the high water mark to capture the sediment flux from the intertidal beach area onto the dry upper beach and one higher up the beach to capture any additional sediment supply from the dry beach itself.

Table 3.1 lists the partitioning of the field campaign in 10 deployments with constant location and orientation of the measurement equipment. Most deployments were located along the westerly transect at the southern flank of the Sand Motor (Figure 3.2). Deployments DNo2a and DNo5a were aligned along alternative transects concurrent with deployments DNo2b and DNo5b respectively. During deployment DN11 all masts were clustered at high grounds as to provide a safe buffer from the expected surge during the storm event of October 23. Consequently, no transport gradients were measured during deployment DN11.

### 3.3.3 Data analysis

Particle count time series obtained from individual Wenglor laser sensors are summed up

Table 3.1: Deployments of measurement masts during the MEGAPEX field campaign.  
Maximum measured wind speeds are in between brackets.

	wind speed [m/s]	wind dir. [°]	laser dir. [°]	transect	duration [h]	sensors [-]	valid* [%]
DNo2a	3 (10)	358	262	W	22	3	0
DNo2b	3 (10)	359	360	N	22	3	100
DNo4	5 (13)	343	360	W	42	3	92
DNo5	3 (15)	196	270	W	312	3	40
DNo6a	5 (17)	166	225	SW	170	3	55
DNo6b	5 (17)	180	225	W	170	3	77
DNo8	5 (16)	199	225	W	160	6	89
DNo9	9 (21)	240	270	W	32	6	87
DNo10	15 (22)	301	315	W	9	6	100
DNo11	10 (24)	322	315	-	25	6	44

\* The last column indicates the percentage of time with valid measurements. DNo1 is omitted from the list as it involved a test run of the equipment only. DNo2b and DNo6b were originally named DNo3 and DNo7 respectively and can be found by these names only in the published dataset (Hoonhout et al., 2016c).

1302 1. per mast, to obtain *per-mast* particle count time series for each measurement  
1303 mast, and

1304 2. over all masts, to obtain *overall* particle count time series over all measurement  
1305 masts.

1306 The per-mast particle counts are not corrected for the number of Wenglor laser sensors  
1307 per mast. Particle count time series are interchangeably referred to as particle count  
1308 rates as the measurement interval was 1 Hz.

1309 The overall particle count time series are used for comparison with the governing  
1310 wind speed. For comparison with the wind direction per-mast particle count time  
1311 series are discretized in bins according to the governing wind direction and subse-  
1312 quently summed over time. Also for comparison with water and bed levels, the  
1313 per-mast particle count time series are discretized in bins and summed over time. Dis-  
1314 cretization is then done according to the global water level and local bed level at the  
1315 measurement location.

1316 Horizontal gradients in particle counts are computed from the per-mast particle  
1317 count time series and the distance between the measurement masts. Vertical distribu-  
1318 tions in particle counts are computed from the per-sensor particle count time series  
1319 for each measurement mast.

1320 Variations in wind direction of more than 45° resulted in adjustment of the ori-  
1321 entation of the Wenglor fork laser sensors. Particle counts with a discrepancy between  
1322 wind direction and laser orientation ( $\Delta\theta_u$ ) of more than 60° are considered invalid  
1323 and are discarded. Other particle counts ( $n_{pc}$ ) are corrected for orientation inaccura-  
1324 cies ( $\hat{n}_{pc}$ ) using the basic geometric correction:

$$\hat{n}_{pc} = \frac{n_{pc}}{\cos(\Delta\theta_u)} \quad (3.2)$$

1325 Periods without significant particle counts are not discarded from the analysis, ex-  
1326 cept for the determination of the average wind direction as the wind direction tends  
1327 to show random behavior for low wind conditions. The last column in Table 3.1 states  
1328 the percentage of time in which valid particle counts are obtained.

1329 **3.4 RESULTS**

1330 The conditions during the field campaign were characterized by calm and sunny  
1331 weather and negligible precipitation. The average wind speed over the entire experi-  
1332 ment was 6 m/s (Figure 3.4, upper panel). The maximum wind speed was registered  
1333 at 24 m/s at the end of the campaign on October 23 during the only measured storm  
1334 event (DN10). The average overall particle count rate over the entire experiment was  
1335  $120 \text{ s}^{-1}$  averaged over all deployed sensors (Figure 3.4, middle panel). The maximum  
1336 overall particle count rate was registered on October 7 at  $5800 \text{ s}^{-1}$  (DN06b). There-  
1337 fore, the maximum registered overall particle count rate did not coincide with the  
1338 maximum wind speed.

1339 The experiment covered two spring-neap cycles with a tidal range varying between  
1340 1.5 and 2.0 m (Figure 3.4, lower panel). The maximum still water level of 2.8 m+MSL  
1341 was measured during storm deployment DN11 on October 22. This surge flooded the  
1342 southern flank of the Sand Motor up to 5 m+MSL.

1343 **3.4.1 Relation between sediment transport and wind speed and water level**

1344 Periods with low wind conditions seem to coincide with periods with a negligible  
1345 overall particle count, whereas periods with fair wind conditions seem to coincide  
1346 with periods with a significant overall particle count (Figure 3.4, upper and middle  
1347 panel). Also the occurrence of peaks in overall particle count show a correspondence  
1348 with peaks in wind speed. However, the highest peaks in wind speed do not neces-  
1349 sarily coincide with the highest peaks in overall particle count, resulting in an overall  
1350 poor correlation between wind speed and overall particle count (Figure 3.5, left panel).  
1351 The poor correlation is reflected in a Spearman rank correlation coefficient (Spearman,  
1352 1904) of zero, indicating that the data cannot be described by a monotonic function of  
1353 any kind.

1354 In the remainder of this paper it is shown that the storm deployments DN10 and  
1355 DN11 provide signals with respect to wind direction, sediment availability and fetch  
1356 that are consistently different from the non-storm deployments DN02 to DN09. In  
1357 anticipation to these findings, correlations between wind speed and overall particle  
1358 count are computed for the storm and non-storm deployments separately, resulting  
1359 in a weak positive relation between wind speed and overall particle count. Fitting  
1360 a third-power curve through these separate datasets results in  $R^2$ -values of 0.43 and  
1361 0.27 respectively. The low  $R^2$ -values indicate that much of the variance in the overall  
1362 particle count is not explained by wind speed.

1363 No relation between the still water level and the overall particle count is found  
1364 (Figure 3.5, right panel). There is no evidence that the spring-neap modulation of the  
1365 high water level of about 0.5 m influenced the overall particle count significantly.

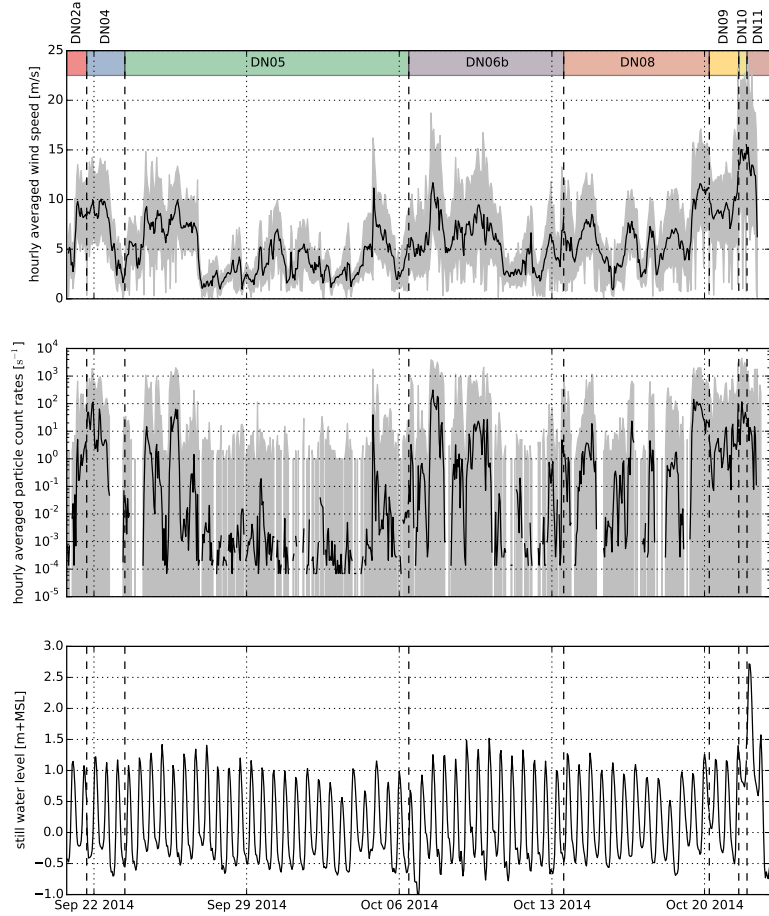


Figure 3.4: Wind time series (upper panel), overall particle count rates during the deployments along the westerly transect (middle panel) and offshore tidal elevation (lower panel). Grey lines indicate the raw data, black lines the hourly averaged data. Colored bars refer to the deployments listed in Table 3.1. Deployments DN02b and DN06a are not included as these are located along different transects.

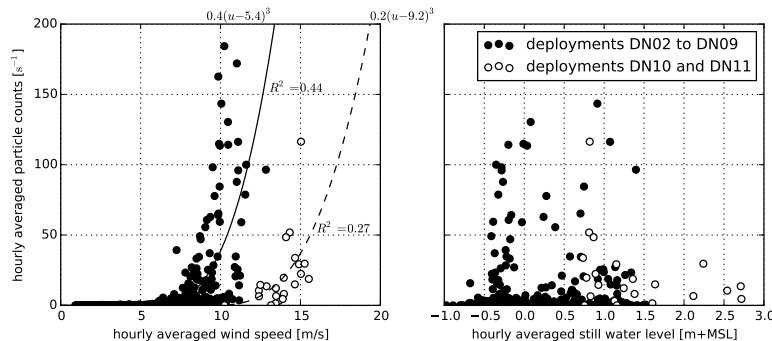


Figure 3.5: Relations between overall particle count and wind speed (left panel) or water level (right panel). Closed circles and continuous lines refer to non-storm deployments DN02 to DN09. Open circles and dashed lines refer to storm deployments DN10 and DN11. All deployments are listed in Table 3.1.

#### 1366 3.4.2 Wind direction and sediment source areas

1367 The vast majority of per-mast particle counts registered at the stationary mast, that  
 1368 was located at the high water line during almost the entire field campaign (Figure  
 1369 3.2), was registered from a limited number of wind directions. These directions do  
 1370 not coincide with the prevailing wind direction or the wind direction with the largest  
 1371 transport potential (Figure 3.6, upper panel).

1372 The upper panel in Figure 3.6 shows that the prevailing wind direction was south,  
 1373 but that the largest transport potential (Equation 3.1) came from the southwesterly  
 1374 and northwesterly directions. The per-mast particle count does not align with the  
 1375 prevailing wind direction or the directions with the largest transport potential as both  
 1376 the southerly and northwesterly wind directions did not induce a significant particle  
 1377 count.

1378 The lower panel in Figure 3.6 shows that most particles are registered from the  
 1379 wind directions with the shortest fetches. However, these wind directions provide  
 1380 among the largest intertidal beach widths along the Dutch coast. The exception is the  
 1381 northwesterly wind direction, that does accommodate a fair intertidal beach width,  
 1382 but did not register a per-mast particle count close to what could be expected from  
 1383 the transport potential. The northwesterly wind directions were solely present during  
 1384 the storm deployment DN10.

#### 1385 3.4.3 Spatial gradients in sediment transport

1386 Significant variations in per-mast particle count along the measurement transects is  
 1387 found. Figure 3.7 shows that the largest increase in per-mast particle count in down-  
 1388 wind direction (positive gradients) is consistently located in the intertidal beach area.

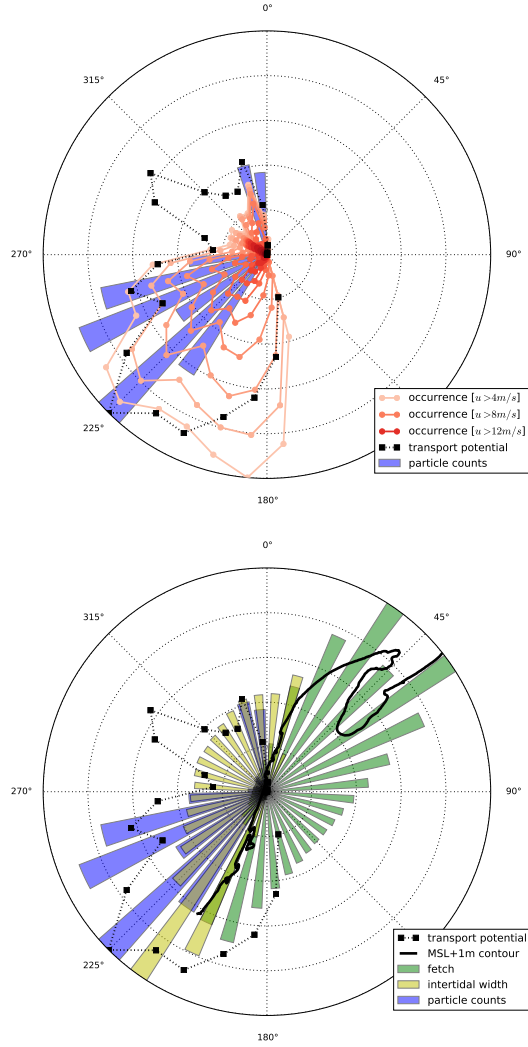


Figure 3.6: Per-mast particle count, wind speed and direction obtained from stationary mast (Figure 3.2, upper panel) and available fetch and intertidal fetches (lower panel).

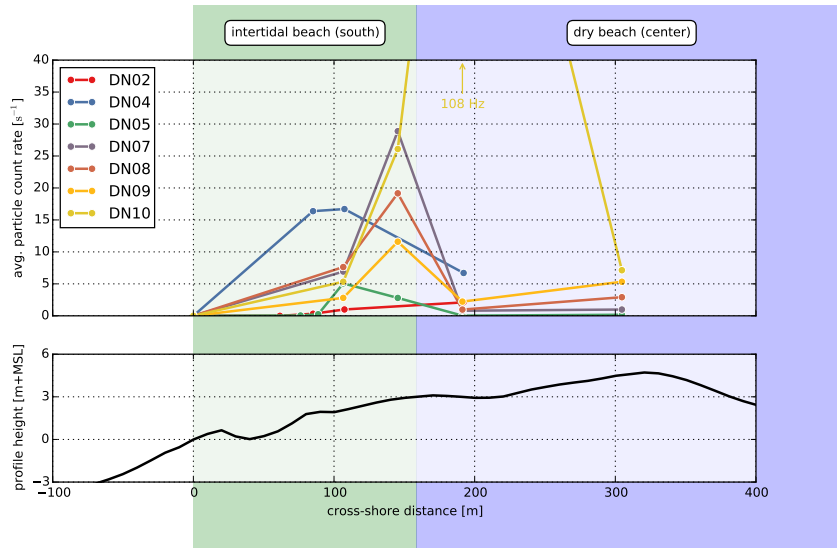


Figure 3.7: Average per-mast particle count rates during the deployments along the westerly transect (upper panel) and beach profile (lower panel). Line colors refer to the partitioning of the time series in Figure 3.4.

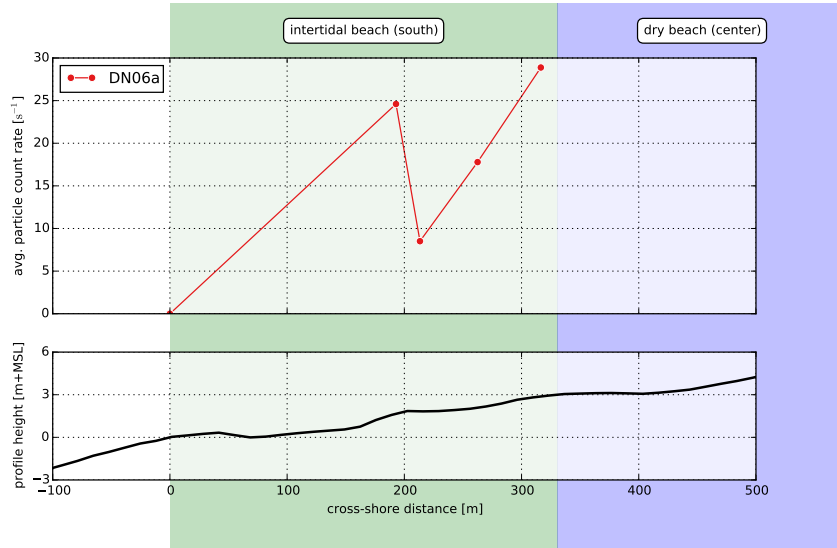


Figure 3.8: Average per-mast particle count rates during deployment DN06a along the southwesterly transect (upper panel) and beach profile (lower panel).

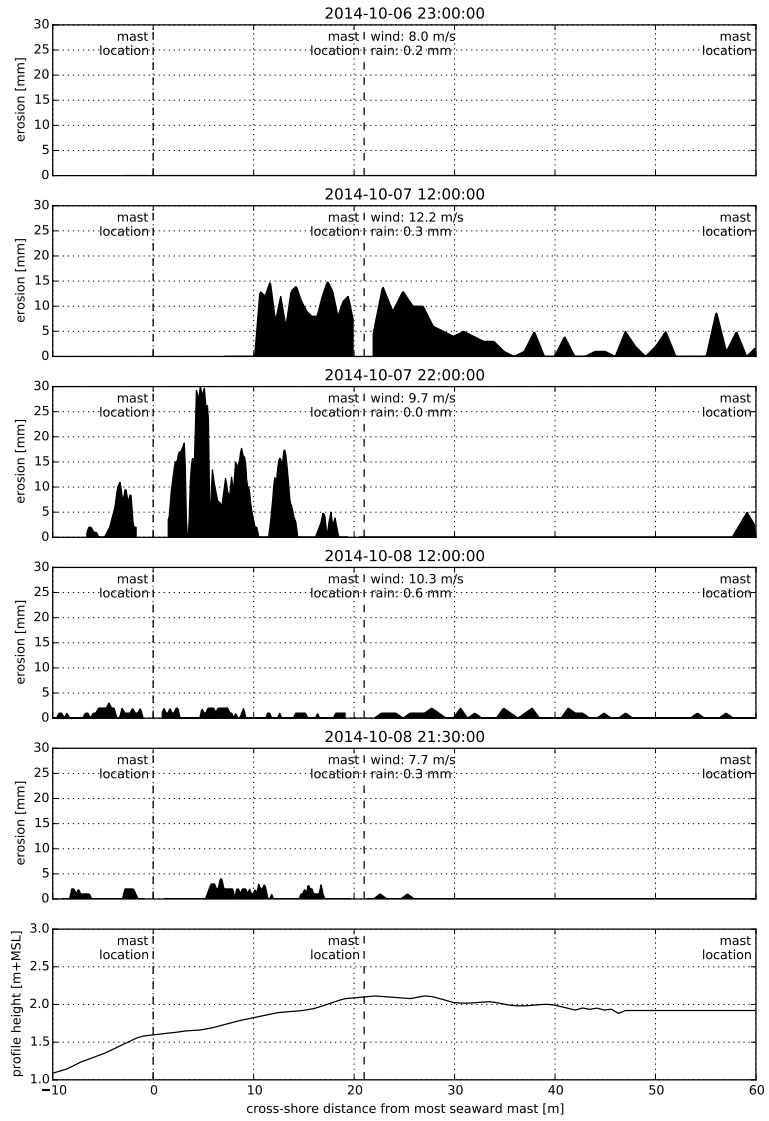


Figure 3.9: Erosion measured using erosion pins during five tidal cycles during deployment DNo6a along the southwesterly transect.

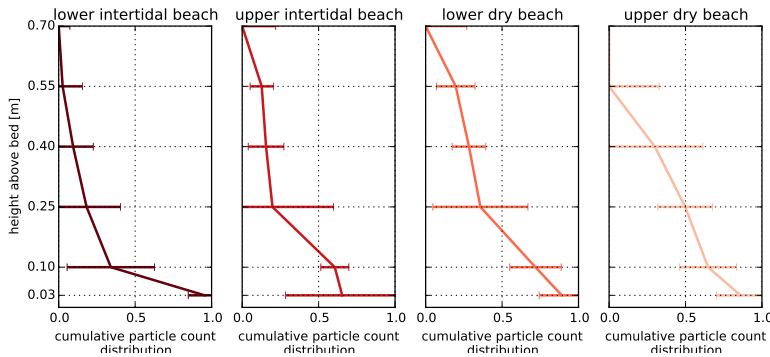


Figure 3.10: Cumulative particle count distribution over the vertical during deployment DNo8. The line indicates the percentage of particles that surpasses a certain height above the bed. The horizontal bars visualize the variability in time of the particle count per laser sensor.

1389 Positive gradients in sediment transport indicate a net erosion of the beach surface  
1390 and thus entrainment of sediment.

1391 A significant decrease in per-mast particle count in downwind direction (negative  
1392 gradients) is consistently found at the transition between intertidal and dry beach.  
1393 Negative gradients in sediment transport indicate net deposition of sediment. Only  
1394 during storm deployment DN10 the negative gradients at the transition were absent  
1395 and large positive gradients in both the intertidal and dry beach area were found  
1396 (Figure 3.7).

1397 The negative gradients coincide with the transition from the berm slope to the  
1398 berm flat. Local deposition of aeolian sediment at the edge of a berm appears to  
1399 be consistent behavior as it is also observed within the intertidal beach area. Four  
1400 masts were deployed along a southwesterly transect within the intertidal beach area  
1401 (DNo6a, Figure 3.8) concurrent with deployment DNo6b. These measurements show  
1402 a significant decrease in per-mast particle count over a minor berm-like feature ( $x =$   
1403 200 m) in the intertidal beach area. Downwind of this feature the per-mast particle  
1404 count increased again with a rate comparable to what was found upwind of the berm-  
1405 like feature. In addition, small scale measurements on bed level change confirm that  
1406 wind erosion is concentrated on the berm slope (Figure 3.9), while the berm flat tends  
1407 to accrete. The maximum erosion of 1.2 cm in a single tidal cycle was measured with  
1408 wind speeds above 10 m/s and little precipitation.

1409 Measured negative gradients might also be caused by sediment locally surpassing  
1410 the measurement equipment. To ensure that the number of surpassing particles is  
1411 limited, the most landward mast in each transect was permanently equipped with  
1412 six laser sensors up to 70 cm above the bed. The number of particles counted in the  
1413 upper laser sensor was consistently low ( $\leq 1\%$ ), suggesting that only a small number  
1414 of particles surpassed the equipment at this point.

1415 At the location downwind of the negative gradients more sediment might have sur-  
1416 passed than at the most landward measurement location. During deployment DNo8  
1417 all four masts were equipped with six laser sensors in order to capture the vertical

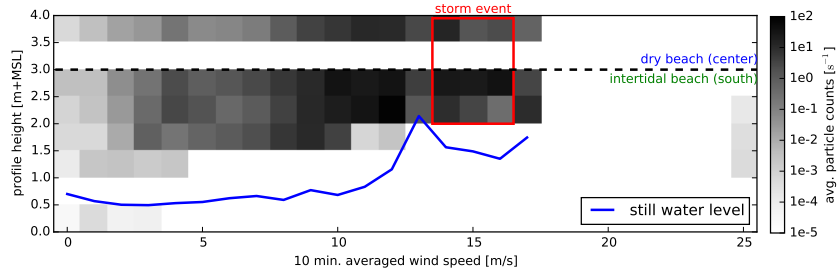


Figure 3.11: Average overall particle count rates depending on governing wind speed and bed level at measurement location, and average still water level depending on governing wind speed.

1418 distribution of the particle count across the beach (Figure 3.10). It appears that the center  
 1419 of gravity of the particle count moves upward in downwind direction. Downwind  
 1420 of the negative transport gradient the percentage of particles counted by the upper  
 1421 laser sensor is 20% compared to  $\leq 10\%$  at the other locations, suggesting that most  
 1422 particles surpass at this location. The difference between the fraction of surpassing  
 1423 particles is too small to explain the large negative gradients, but are likely to cause  
 1424 the measured negative gradients to be overestimated.

#### 1425 3.4.4 Fetch vs. sediment availability

1426 In Figure 3.11 the overall particle count obtained during the field campaign is binned  
 1427 according to the prevailing wind speed and the bed level at the measurement location.  
 1428 The average still water level is an indication of available fetch. The peak in overall par-  
 1429 ticle count is at 3 m+MSL irrespective of the wind speed and available fetch. Therefore  
 1430 the overall particle count seems to be limited by location rather than wind speed or  
 1431 available fetch. The specific location at which the particle count peaks corresponds  
 1432 to the high water line and the onset of the shell pavement that largely covers the dry  
 1433 beach.

#### 1434 3.5 DISCUSSION

1435 The positive gradients in per-mast particle count in the intertidal beach area and minor  
 1436 positive gradients in the dry beach area suggest that the intertidal beach is a primary  
 1437 source of aeolian sediment in the Sand Motor region. This observation is in accor-  
 1438 dance with the large scale sediment budgets of the Sand Motor region (Hoonhout  
 1439 and de Vries, 2016a). Armoring of the dry beach surface, due to the emergence of  
 1440 shells and other roughness elements, might lead to a significant reduction in local  
 1441 aeolian sediment availability. Similarly, sediment availability might also be limited in  
 1442 the intertidal beach area due to periodic flooding and consequently high soil mois-

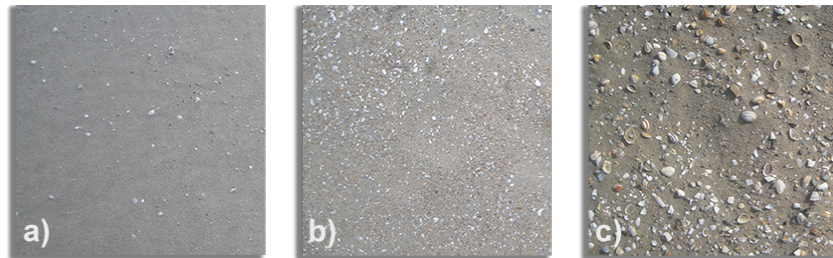


Figure 3.12: Visual impression of armor layer at three locations in the Sand Motor region: a) intertidal beach, no armoring b) lower dry beach, minor armoring with shell fragments c) upper dry beach, severe armoring with many shells and coarse sand. Covered surface is approximately 40 x 40 cm in all cases.

ture contents. From the differences in per-mast particle count gradients between the intertidal and dry beach it can be assumed that the reduction of sediment availability due to armoring outweighs the influence of soil moisture. Local differences in bed surface properties would therefore induce relative differences in sediment availability that govern aeolian sediment transport in the Sand Motor region.

The negative gradients in per-mast particle count at the transition between intertidal and dry beach indicate that sediment eroded from the intertidal beach is deposited locally on the dry beach. Morphological feedback with the wind might cause the sediment transport capacity to peak at the berm edge due to the presence of a locally accelerated wind (i.e. jet flow; [Hesp and Smyth, 2016](#)), resulting in deposition at the berm flat. In addition, the berm edge coincides with the visually observed onset of a shell pavement (Figure 3.12). The shell pavements emerged from the nourished sediment in the first half year after construction of the Sand Motor ([Hoonhout and de Vries, 2016a](#)) due to winnowing of sand from the bed. The exact influence of a shell pavement on saltation is challenging to assess. Roughness elements, like shells and cobbles, might trap impacting grains, and hamper saltation, or cause fully elastic collisions, and enhance saltation. The shell pavement at the measurement locations is relatively open and therefore both processes are likely to be relevant. The consistent negative gradients in particle count at the onset of the shell pavement suggest that trapping of sediment is dominant over the enhancement of saltation due to fully elastic collisions.

The local deposition of sediment at the berm flat is temporary as no accumulation of sand is observed on top of the shell pavement during the MEGAPEX field campaign. This suggests that sediment supply from marine sources and deposition in dunes, dune lake and lagoon is a phased process. Otherwise the sediment supply to the dunes would cease during high water as the main sediment source is flooded. In an phased system the local sediment deposits at the berm flat might act as temporary sediment source during high water (Figure 3.13). Consequently, measured aeolian sediment transport rates would be continuous and independent of the instantaneous water level. The phasing of erosion and deposition can therefore explain the weak

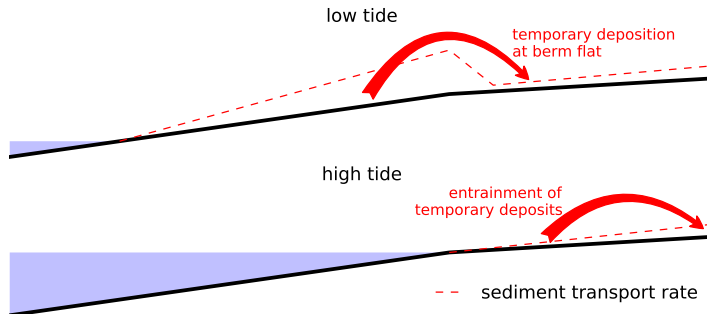


Figure 3.13: Conceptual illustration of how temporal deposits facilitate a continuous sediment supply from the intertidal beach to the dunes.

1473 correlations between measured overall particle count and the instantaneous water  
 1474 level, which seemed to contrast the conclusion that the intertidal beach is a primary  
 1475 source of aeolian sediment.

1476 The phasing of erosion and deposition increases the duration of transport from the  
 1477 intertidal beach to the dunes. The environmental conditions therefore need to be fa-  
 1478 vorable for aeolian sediment transport over a longer period for the sediment to reach  
 1479 the dunes. This requirement for dune growth closely relates to the need for synchro-  
 1480 nization between sediment availability and wind transport capacity emphasized by  
 1481 Houser (2009).

1482 Low average water levels accommodate initiation of aeolian sediment transport rel-  
 1483 atively distant from the high water line where the overall particle count tends to peak.  
 1484 As average water levels increase with increasing wind speed, due to wind setup, the  
 1485 available fetch decreases. Nevertheless, the overall particle count still peaks close to  
 1486 the high water line and not beyond. Moreover, the height of the peak in overall par-  
 1487 ticle count increases with increasing wind speed. Both the decrease in available fetch  
 1488 and the increase in maximum overall particle count result in an increase in overall  
 1489 particle count gradient over the intertidal beach. The increased gradient indicates  
 1490 that also the rate of sediment entrainment in the intertidal beach area increases and  
 1491 overcompensates the decrease in fetch. Also the entrainment rate at the dry beach  
 1492 increases with increasing wind speed, but to a significantly less extent than at the  
 1493 intertidal beach. The exception is again the storm deployment DN10, which shows a  
 1494 peak in overall particle count landward of the high water line.

1495 During a high wind event the relative importance of limitations in sediment avail-  
 1496 ability might change. Strong winds can mobilize even the largest sediment fractions  
 1497 and shell fragments. Consequently, the beach armor layer itself might be transported  
 1498 and its reducing effect on sediment availability might be (partially) neutralized. Also  
 1499 the trapping of sediment due to an increase in bed roughness might be less effective  
 1500 and the influence of the berm on the wind flow reduced. In addition, high wind  
 1501 events are regularly accompanied with surges that prevent wind erosion of the in-  
 1502 tertidal beach. Instead, the wind energy can be used for erosion of the dry beach,  
 1503 which contributes to the removal of the beach armor layer. The surge itself might

1504 also remove the beach armor layer by wave action or bury it by deposition of marine  
1505 sediments. The removal or burial of the beach armor layer might elevate sediment  
1506 availability from the dry beach also after the the storm passed. Only after develop-  
1507 ment of a new beach armor layer the sediment availability and transport rates then  
1508 equal the pre-storm situation.

1509 **3.6 CONCLUSIONS**

1510 The Sand Motor (or Sand Engine) is a 21 Mm<sup>3</sup> mega nourishment along the Dutch  
1511 coast that is constructed well above storm surge level (Stive et al., 2013) and therefore  
1512 largely shaped by wind. During the six week MEGAPEX field campaign in the fall of  
1513 2014, spatial gradients in aeolian sediment transport were measured. The gradients  
1514 identified the intertidal beach as the primary source of aeolian sediment. In addition,  
1515 local temporal deposition of sediment at the berm flat occurred. The deposition is  
1516 likely caused by a combination of morphological feedback with the wind and an in-  
1517 crease in bed roughness due to the presence of a shell pavement. The local deposition  
1518 of sediment causes the transport of sediment from intertidal beach to dunes, dune  
1519 lake and lagoon to be phased.

1520 From the measurements the following conclusions can be drawn:

- 1521 1. In the Sand Motor region, the (southern) intertidal beach area is a more impor-  
1522 tant source of aeolian sediment than the dry beach area.
- 1523 2. The relative importance of the intertidal beach as supplier of aeolian sediment  
1524 could be explained by the development of a beach armor layer in the dry beach  
1525 area that outweighs the influence of high soil moisture contents in the intertidal  
1526 beach area.
- 1527 3. Aeolian sediment originating from the intertidal beach seems to settle on the  
1528 berm flat and to be gradually transported further resulting in an continuous  
1529 sediment flux from the intertidal beach area and into the dunes, even if the  
1530 intertidal beach is flooded.
- 1531 4. During high wind events, aeolian sediment availability in the intertidal beach  
1532 area tends to be reduced by high water levels, while the sediment availability in  
1533 the dry beach area tends to be increased due to mobilization of the beach armor  
1534 layer.

1535

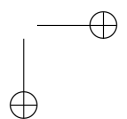
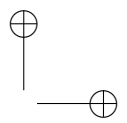
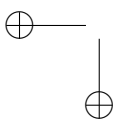
## Part II

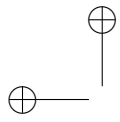
1536

### NUMERICAL MODELING

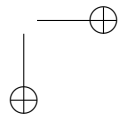
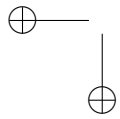
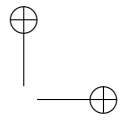
1537  
1538  
1539

Inspired by the field observations a numerical model is developed and applied to hindcast the sub-aerial morphological evolution of the Sand Motor for the 4 years after construction.





"thesis" — 2016/11/15 — 10:57 — page 46 — #76



# 4

1540

1541

---

## 1542 NUMERICAL MODEL

---

1543 This chapter is based on a previous publication: Hoonhout, B. M. and de Vries, S. (2016d).  
 1544 A process-based model for aeolian sediment transport and spatiotemporal varying sediment  
 1545 availability. Journal of Geophysical Research: Earth Surface. 2015JF003692.

1546 The numerical implementation of the model presented in this chapter and experimental features  
 1547 not discussed are elaborated in Appendix B.

1548 4.1 INTRODUCTION

1549 Aeolian sediment transport is influenced by a variety of bed surface properties that  
 1550 are commonly found in coastal environments, like: moisture, shells, strandlines, salt  
 1551 crusts, bed slopes, vegetation, non-erodible elements and anthropogenic disturbances.  
 1552 The bed surface properties influence aeolian sediment transport by changing the sed-  
 1553 ient transport capacity and/or the sediment availability (Kocurek and Lancaster,  
 1554 1999). In current aeolian sediment transport models the effects on the sediment trans-  
 1555 port capacity and sediment availability are generally incorporated through a single  
 1556 parameter: the velocity threshold. This approach appears to be a critical limitation  
 1557 in existing aeolian sediment transport models for simulation of real-world cases with  
 1558 spatiotemporal variations in bed surface properties.

1559 The velocity threshold was introduced by Bagnold (1935), and incorporated in his  
 1560 initial aeolian sediment transport model (Bagnold, 1937b) according to:

$$q_{\text{sat}} = \underbrace{\alpha}_{\substack{\text{sediment} \\ \text{transport} \\ \text{capacity}}} \underbrace{C \frac{\rho_a}{g} \sqrt{\frac{d_n}{D_n}}}_{\substack{\text{properties} \\ \text{of sediment} \\ \text{in transport}}} (u_z - u_{\text{th}})^3 \quad (4.1)$$

1561 in which  $q_{\text{sat}}$  [kg/m/s] is the equilibrium or saturated sediment transport rate and  
 1562 represents the sediment transport capacity.  $u_z$  [m/s] is the wind velocity at height  $z$   
 1563 [m] and  $u_{\text{th}}$  the velocity threshold [m/s]. The properties of the sediment in transport  
 1564 are represented by a series of parameters:  $C$  [-] is a parameter to account for the  
 1565 grain size distribution width,  $\rho_a$  [kg/m<sup>3</sup>] is the density of the air,  $g$  [m/s<sup>2</sup>] is the  
 1566 gravitational constant,  $d_n$  [m] is the nominal grain size and  $D_n$  [m] is a reference grain  
 1567 size.  $\alpha$  is a constant to account for the conversion of the measured wind velocity to the  
 1568 near-bed shear velocity following Prandtl-Von Kármán's Law of the Wall:  $\left(\frac{\kappa}{\ln z/z'}\right)^3$   
 1569 in which  $z'$  [m] is the height at which the idealized velocity profile reaches zero and  $\kappa$

1570 [-] is the Von Kármán constant. Many studies following the work of [Bagnold \(1937b\)](#)  
1571 effectively proposed different parameterizations for sediment properties (e.g. [Owen,](#)  
1572 [1964; Hsu, 1971; Sørensen, 2004](#)) or changed the weight of the velocity threshold (e.g.  
1573 [Kawamura, 1951; Lettau and Lettau, 1978](#)). However, the characteristic structure and  
1574 application of these models stayed essentially the same.

1575 [Sherman et al. \(1998\)](#) and [Sherman and Li \(2012\)](#) summarized the performance of  
1576 eight aeolian sediment transport models compared to field measurements on a sandy  
1577 beach. All the models systematically overpredict the measured aeolian sediment trans-  
1578 port rates, which is in agreement with other coastal field studies (e.g. [Jackson and](#)  
1579 [Cooper, 1999; Lynch et al., 2008; Davidson-Arnott and Bauer, 2009; Aagaard, 2014](#)).  
1580 Besides, the original model of [Bagnold \(1937b\)](#) appeared to outperform the models of  
1581 later date. In an attempt to explain the poor performance of aeolian sediment trans-  
1582 port models in coastal environments, many authors emphasized the importance of  
1583 bed surface properties. Typical bed surface properties that are found along the coast  
1584 and assumed to explain at least partially the poor performance of aeolian sediment  
1585 transport models are high moisture contents (e.g. [Wiggs et al., 2004; Davidson-Arnott](#)  
1586 [et al., 2008; Darke and McKenna Neuman, 2008; McKenna Neuman and Sanderson,](#)  
1587 [2008; Udo et al., 2008; Bauer et al., 2009; Edwards and Namikas, 2009; Namikas et al.,](#)  
1588 [2010; Scheidt et al., 2010](#)), salt crusts (e.g. [Nickling and Ecclestone, 1981](#)), bed slopes  
1589 (e.g. [Iversen and Rasmussen, 2006](#)), vegetation (e.g. [Arens, 1996; Lancaster and Baas,](#)  
1590 [1998; Okin, 2008; Li et al., 2013; Dupont et al., 2014](#)), shell pavements (e.g. [van der](#)  
1591 [Wal, 1998; McKenna Neuman et al., 2012](#)) and sorted and armored beach surfaces (e.g.  
1592 [Gillette and Stockton, 1989; Gillies et al., 2006; Tan et al., 2013; Cheng et al., 2015](#)). The  
1593 influence of these bed surface properties on aeolian sediment transport has been inves-  
1594 tigated and often resulted in modified values for the velocity threshold (e.g. [Howard,](#)  
1595 [1977; Dyer, 1986; Belly, 1964; Johnson, 1965; Hotta et al., 1984; Nickling and Ecclestone,](#)  
1596 [1981; Arens, 1996; King et al., 2005](#)).

1597 A critical limitation of the use of the velocity threshold alone to cope with the  
1598 influence of bed surface properties is that it changes inherently in time and space  
1599 ([Stout, 2004](#)) and that it accounts for two fundamentally different phenomena:

- 1600 1. The change in the sediment transport capacity which represents the ease of  
1601 sediment transport *over* a given bed; and
- 1602 2. The change in sediment availability, which represents the ease of sediment en-  
1603 trainment *from* a given bed.

1604 Although in uniform and constant situations, like often used in wind tunnel experi-  
1605 ments, the difference might be negligible, in real-world field conditions it is not. The  
1606 difference is most apparent when observing transport over a bed with spatial vari-  
1607 ations in bed surface properties. For example due to tidal motions in the intertidal  
1608 beach area, emergence of roughness elements in the dry beach area and vegetation in  
1609 the dune area. In addition, temporal variations in bed surface properties, for example  
1610 due to tidal spring/neap cycles, rain showers, storm surges, seasonal variations in  
1611 vegetation and progressive armoring of the beach, increase the need for simulation  
1612 rather than parameterization of bed surface properties and sediment availability (as  
1613 discussed in section [4.2](#)).

1614 This paper presents a new model approach for aeolian sediment transport. The  
1615 model simulates rather than parameterizes bed surface properties and sediment avail-

ability. The model explicitly defines sediment availability following de Vries et al. (2014b) and introduces multi-fraction aeolian sediment transport in order to simulate processes that limit the availability of sediment, like beach armoring, and processes that enhance the availability of sediment, like hydraulic mixing. Consequently, the model can cope with arbitrary spatiotemporal configurations of bed surface properties. Although validation of the model is ongoing, the performance of the model is illustrated using four prototype cases, the simulation of two wind tunnel experiments from literature (Nickling and McKenna Neuman, 1995; Dong et al., 2004b) and a sensitivity analysis of newly introduced parameters.

In literature the *velocity threshold* is used interchangeably to describe the (change in) sediment transport capacity and sediment availability. In this paper the term *velocity threshold* is strictly used to describe the (change in) sediment transport capacity (Equation 4.1). The term *sediment availability* is used in accordance with the terminology proposed by Kocurek and Lancaster (1999), which is often referred to as *sediment supply* in literature.

#### 1631 4.2 MODEL CHALLENGES: BED SURFACE PROPERTIES

1632 The importance of spatiotemporal variations in bed surface properties for aeolian  
 1633 sediment transport is most apparent when observing transport over a bed consisting  
 1634 of both erodible and non-erodible fractions. Many studies have investigated the  
 1635 influence of varying grain sizes on aeolian sediment transport. In most cases it in-  
 1636 volved studies on the influence of non-erodible or roughness elements using either  
 1637 field experiments (e.g. Davidson-Arnott et al., 1997; Gillies et al., 2006; Tan et al.,  
 1638 2013) or wind tunnel experiments (e.g. Gillette and Stockton, 1989; Nickling and  
 1639 McKenna Neuman, 1995; McKenna Neuman and Nickling, 1995; Dong et al., 2004b;  
 1640 McKenna Neuman et al., 2012) and occasionally numerical modeling (e.g. Turpin et al.,  
 1641 2010). The studies typically use granular material with a clear bi-modal distribution.  
 1642 A flat sandy surface is then partially covered by a significantly larger grain size frac-  
 1643 tion ranging from shells and gravel to pebbles and cobbles. Typically the coverage  
 1644 of non-erodible elements is expressed using the roughness density  $\lambda$  as described by  
 1645 Raupach et al. (1993). Raupach et al. (1993) uses the roughness density to determine  
 1646 the relative increase in the shear velocity threshold according to:

$$R_t = \frac{u_{*th,S}}{u_{*th,R}} = \frac{1}{\sqrt{(1 - m\sigma\lambda)(1 + m\beta\lambda)}} \quad (4.2)$$

1647 in which  $u_{*th,S}$  is the shear velocity threshold with a bare surface,  $u_{*th,R}$  is the shear  
 1648 velocity threshold with a surface including non-erodible elements and  $m$ ,  $\sigma$  and  $\beta$   
 1649 are calibration coefficients that account for the size and shape of the non-erodible  
 1650 elements.

##### 1651 4.2.1 Temporal Variations in Bed Surface Properties

1652 The concept of the roughness density is useful to describe the instantaneous influence  
 1653 of roughness elements in the bed on aeolian sediment transport. However, it does

not account for the fact that roughness elements tend to emerge from the bed over time due to winnowing of fines. Following Gillette and Stockton (1989), Nickling and McKenna Neuman (1995) and McKenna Neuman and Nickling (1995) showed that the winnowing of fines and the emergence of roughness elements result in a time-dependent aeolian sediment transport rate. The time-dependency is caused by a recurrence relation between sediment transport and sediment availability. Consequently, neither the roughness density nor the sediment availability can be determined a-priori. We argue that process-based simulation of bed surface properties rather than parameterization is needed to solve the instantaneous sediment availability.

McKenna Neuman et al. (2012) shows that even small shell fragments cause a sandy surface to be armored over time. But even in the absence of non-erodible roughness elements, spatiotemporal variations in bed surface properties may develop as the transport capacity is inversely related to the grain size (Bagnold, 1937b) resulting in sediment sorting: a coarsening of the bed surface and downwind deposition of fines (Bagnold, 1937b; van der Wal, 2000; Arens et al., 2002).

#### 4.2.2 Spatial Variations in Bed Surface Properties

Spatial variations in bed surface properties occur naturally in coastal environments. For example, strandlines locally cover the erodible bed and reduce the sediment availability. However, strandlines not necessarily reduce the sediment transport capacity to the same extent and may even increase the transport capacity due to fully elastic collisions with the sediment in transport. The distinction between sediment availability and sediment transport capacity in relation to bed surface properties is not offered by existing models.

Dong et al. (2004b) describes a similar situation in a wind tunnel. In their experiment a patch of gravel (10 - 40 mm) is positioned downwind of a patch of sandy material. Dong et al. (2004b) show how the gravel patch reduces the aeolian sediment transport rate downwind of the domain compared to the situation without the gravel. However, in all conditions sediment passes the patch, while sediment availability from the patch is zero. There seems to be a tendency of an increase in sediment transport rate with increasing patch size when the patch size is relatively small. This is attributed to the change in transport characteristics due to fully elastic collisions between the sand grains and the gravel. Consequently, the saltation height and rebound angle increase and in turn influence the sediment transport capacity. Only for large patch sizes the trapping of sand grains in the gravel pores becomes a dominant process resulting in a decrease in the sediment transport rate downwind of the gravel patch.

Dong et al. (2004b) acknowledged the limitations of the use of the shear velocity threshold to describe the results of his wind tunnel experiments. Therefore they introduced a factor in the aeolian sediment transport formulation of Dymen (1954) that depends on the length of the gravel patch squared. Although an important observation, the method is hardly generalizable to more realistic situations where moist intertidal beaches are located adjacent to strandlines and armored beaches that subsequently border a vegetated dune. Therefore, to cope with spatially varying bed surface properties an aeolian sediment transport model is needed that provides a

1698 generic distinction between the effect of bed surface properties on the sediment trans-  
 1699 port capacity and sediment availability.

1700 4.3 MODEL CONCEPTS: SEDIMENT AVAILABILITY, SATURATED TRANSPORT AND  
 1701 ENTRAINMENT

1702 The sediment transport capacity and sediment availability together determine the sed-  
 1703 iment entrainment. Sediment availability differs from entrainment in that the avail-  
 1704 ability defines the *potential* erosion of the bed, while the entrainment defines the *actual*  
 1705 erosion of the bed. If aeolian sediment transport is transport-limited, the sediment  
 1706 availability is larger than entrainment and not all available sediment will be trans-  
 1707 ported. Consequently, entrainment is governed by the sediment transport capacity. If  
 1708 aeolian sediment transport is availability-limited, entrainment is equal to the sediment  
 1709 availability. Whether aeolian sediment transport is transport- or availability-limited  
 1710 depends on the balance between the sediment transport capacity and the sediment  
 1711 availability that are both influenced by bed surface properties. In the literature vari-  
 1712 ous concepts to incorporate the influence of bed surface properties in aeolian sediment  
 1713 transport models can be found:

- 1714 1. the concept of the shear velocity threshold (e.g. Howard, 1977; Dyer, 1986; Belly,  
 1715 1964; Johnson, 1965; Hotta et al., 1984; Nickling and Ecclestone, 1981; Arens,  
 1716 1996);
- 1717 2. the concept of critical fetch (e.g. Bauer and Davidson-Arnott, 2002; Delgado-  
 1718 Fernandez, 2010);
- 1719 3. the concept of explicit availability (or supply; de Vries et al., 2014b).

1720 From these concepts the shear velocity threshold is typically applied in conjunction  
 1721 with a formulation for the aeolian sediment transport capacity (e.g. Equation 4.1).  
 1722 The sediment transport capacity described by these formulations is the equilibrium  
 1723 or saturated sediment transport rate. The saturated sediment transport rate is the  
 1724 maximum transport rate reached in case of a fetch ( $F$ ) beyond the critical fetch ( $F_c$ ,  
 1725 Bauer and Davidson-Arnott, 2002). In case of abundant sediment availability and  
 1726 fetches beyond the critical fetch the saturated sediment transport rate seems to be  
 1727 an appropriate indicator for the actual sediment flux downwind of the observed do-  
 1728 main. However, in coastal environments fetches can be limited due to limited beach  
 1729 widths (e.g. Jackson and Cooper, 1999; Bauer et al., 2009; Davidson-Arnott et al., 2005;  
 1730 Delgado-Fernandez, 2010; Dong et al., 2004a) and sediment availability is limited due  
 1731 to beach armoring as well as other bed surface properties. Consequently, in reality  
 1732 the saturated sediment transport rate is not necessarily an appropriate indicator for  
 1733 the sediment flux downwind of the observed domain.

1734 The concept of critical fetch therefore introduces a measure to distinguish between  
 1735 saturated ( $F \geq F_c$ ) and unsaturated sediment transport situations ( $F < F_c$ ). In this  
 1736 approach the aeolian sediment transport rate, (critical) fetch distance, entrainment  
 1737 and sediment availability are related following:

$$q = \int_0^{\hat{F}} \phi(u_*, u_{*th}, m_a) dx \quad \text{with } \hat{F} = \min(F, F_c) \quad (4.3)$$

1738 where  $q$  [kg/s/m] is the instantaneous sediment transport rate per unit width,  $F$   
 1739 [m] is the fetch distance and  $F_c$  [m] the critical fetch distance,  $\phi$  is the entrainment  
 1740 function that depends on the shear velocity  $u_*$  [m/s], the shear velocity threshold  $u_{*th}$   
 1741 [m/s] and the available sediment mass  $m_a$  [kg/m<sup>2</sup>].  $x$  [m] is the downwind distance  
 1742 from a zero-transport boundary. This integral is solved for by assuming a pre-defined  
 1743 entrainment rate. Equation 4.3 then simplifies to:

$$q = \Phi(u_*, u_{*th}, m_a, \hat{F}) \quad (4.4)$$

1744 where  $\Phi$  is the analytically integrated solution to Equation 4.3. Delgado-Fernandez  
 1745 and Davidson-Arnott (2011) use the critical fetch concept to incorporate the effect of  
 1746 spatiotemporal variations in soil moisture. However, due to the recurrence relation in  
 1747 time between the aeolian sediment transport rate  $q$  and the sediment availability  $m_a$ ,  
 1748 neither the sediment availability nor the entrainment can be determined a-priori and  
 1749 the integral in Equation 4.3 cannot easily be solved analytically.

1750 Equation 4.3 can be simplified by observing the difference between availability-  
 1751 limited and transport-limited situations. In availability-limited situations the entrain-  
 1752 ment function simplifies to  $\frac{\partial m_a}{\partial t}$ , while in transport-limited situations the sediment  
 1753 availability is abundant. Equation 4.3 can therefore be rewritten as:

$$q = \begin{cases} \int_0^{\hat{F}} \frac{\partial m_a}{\partial t} dx & \text{if availability-limited} \\ \int_0^{\hat{F}} \phi(u_*, u_{*th}) dx & \text{if transport-limited} \end{cases} \quad (4.5)$$

1754 The wind velocity can influence sediment availability indirectly through beach armor-  
 1755 ing. Given constant wind velocity, the development of a beach armor layer can turn a  
 1756 transport-limited situation into an availability-limited situation, which subsequently  
 1757 influences the instantaneous aeolian sediment transport rate. In an availability-limited  
 1758 situation, entrainment does not depend on the wind velocity since the wind velocity  
 1759 is sufficiently high to mobilize all available sediment.

1760 The distinction between availability-limited and transport-limited situations in  
 1761 Equation 4.5 naturally reveals the fundamental difference between sediment availabil-  
 1762 ity and the sediment transport capacity and shows why these two phenomena cannot  
 1763 be represented by a single parameter like the shear velocity threshold. Moreover,  
 1764 Equation 4.5 provides an opportunity to model availability-limited and transpor-  
 1765 t-limited situations separately as proposed by de Vries et al. (2014b), who uses a 1D  
 1766 advection formulation in combination with the concept of a spatiotemporal varying  
 1767 sediment availability  $m_a$  (or supply  $S_e$  according to the terminology of de Vries et al.  
 1768 (2014b)) to regulate the entrainment, transport and deposition of sediment by wind.

1769 The disadvantage of the use of an explicit term for the sediment availability is that  
 1770 little is known about the quantitative relation between availability and the different  
 1771 availability-limiting bed surface properties. Moreover, also in the approach of de Vries  
 1772 et al. (2014b) sediment availability is not quantified by the model, but is input to  
 1773 the model. Due to the recurrence relation between the sediment transport rate and  
 1774 sediment availability the governing input parameter to this model is unknown and the  
 1775 resulting instantaneous sediment transport rate cannot be computed. Therefore we  
 1776 propose to extend the approach of de Vries et al. (2014b) with numerical simulation  
 1777 of spatiotemporal varying bed surface properties and sediment availability.

1778 4.4 MODEL DESCRIPTION

1779 The model approach of [de Vries et al. \(2014b\)](#) is extended to compute the spatiotemporal  
 1780 varying sediment availability through simulation of the process of beach armoring.  
 1781 For this purpose the bed is discretized in horizontal grid cells and in vertical bed layers  
 1782 (2DV). Moreover, the grain size distribution is discretized into fractions. This allows  
 1783 the grain size distribution to vary both horizontally and vertically. A bed composition  
 1784 module is used to compute the sediment availability for each sediment fraction in-  
 1785 dividually. This model approach is a generalization of existing model concepts, like  
 1786 the shear velocity threshold and critical fetch, and therefore compatible with these  
 1787 existing concepts.

1788 4.4.1 Advection Scheme

1789 A 1D advection scheme is adopted in correspondence with [de Vries et al. \(2014b\)](#) in  
 1790 which  $c$  [kg/m<sup>2</sup>] is the instantaneous sediment mass per unit area in transport:

$$\frac{\partial c}{\partial t} + u_z \frac{\partial c}{\partial x} = E - D \quad (4.6)$$

1791  $t$  [s] denotes time and  $x$  [m] denotes the cross-shore distance from a zero-transport  
 1792 boundary.  $E$  and  $D$  [kg/m<sup>2</sup>/s] represent the erosion and deposition terms and hence  
 1793 combined represent the net entrainment of sediment. Note that Equation 4.6 differs  
 1794 from Equation 9 in [de Vries et al. \(2014b\)](#) as they use the saltation height  $h$  [m] and the  
 1795 sediment concentration  $C_c$  [kg/m<sup>3</sup>]. As  $h$  is not solved for, the presented model com-  
 1796 putes the sediment mass per unit area  $c = hC_c$  rather than the sediment concentration  
 1797  $C_c$ . For conciseness we still refer to  $c$  as the *sediment concentration*.

1798 The net entrainment is determined based on a balance between the equilibrium  
 1799 or saturated sediment concentration  $c_{sat}$  [kg/m<sup>2</sup>] and the instantaneous sediment  
 1800 transport concentration  $c$  and is maximized by the available sediment in the bed  $m_a$   
 1801 [kg/m<sup>2</sup>] according to:

$$E - D = \min \left( \frac{\partial m_a}{\partial t} ; \frac{c_{sat} - c}{T} \right) \quad (4.7)$$

1802  $T$  [s] represents an adaptation time scale that is assumed to be equal for both erosion  
 1803 and deposition. A time scale of 1 second is commonly used ([de Vries et al., 2014b](#)).

1804 The saturated sediment concentration  $c_{sat}$  is computed using an empirical sediment  
 1805 transport formulation (e.g. Equation 4.1) where the transport rate  $q_{sat}$  is divided by  
 1806 the wind velocity  $u_z$  to obtain a mass per unit area (per unit width):

$$c_{sat} = \max \left( 0 ; \alpha C \frac{\rho_a}{g} \sqrt{\frac{d_n}{D_n}} \frac{(u_z - u_{th})^3}{u_z} \right) \quad (4.8)$$

1807 in which  $C$  [-] is an empirical constant to account for the grain size distribution  
 1808 width,  $\rho_a$  [kg/m<sup>3</sup>] is the air density,  $g$  [m/s<sup>2</sup>] is the gravitational constant,  $d_n$  [m] is  
 1809 the nominal grain size,  $D_n$  [m] is a reference grain size,  $u_z$  [m/s] is the wind velocity  
 1810 at height  $z$  [m] and  $\alpha$  [-] is a constant to convert from measured wind velocity to  
 1811 shear velocity.

1812 Note that at this stage the spatial variations in wind velocity are not solved for and  
 1813 hence no morphological feedback is included in the simulation. The model is initially  
 1814 intended to provide accurate sediment fluxes from the beach to the dunes rather than  
 1815 to simulate subsequent dune formation.

1816 *4.4.2 Multi-fraction Erosion and Deposition*

1817 The formulation for the equilibrium or saturated sediment concentration  $c_{\text{sat}}$  (Equation 4.8) is capable of dealing with variations in grain size through the variables  $u_{\text{th}}$ ,  
 1818  $d_n$  and C (Bagnold, 1937b). However, the transport formulation only describes the  
 1819 saturated sediment concentration assuming a fixed grain size distribution, but does  
 1820 not define how multiple fractions coexist in transport. If the saturated sediment con-  
 1821 centration formulation would be applied to each fraction separately and summed up  
 1822 to a total transport, the total sediment transport would increase with the number of  
 1823 sediment fractions. Since this is unrealistic behavior the saturated sediment concen-  
 1824 tration  $c_{\text{sat}}$  for the different fractions should be weighted in order to obtain a realistic  
 1825 total sediment transport. Equation 4.7 therefore is modified to include a weighting  
 1826 factor  $\hat{w}_k$  in which  $k$  represents the sediment fraction index:

$$E_k - D_k = \min \left( \frac{\partial m_{a,k}}{\partial t} ; \frac{\hat{w}_k \cdot c_{\text{sat},k} - c_k}{T} \right) \quad (4.9)$$

1828 It is common to use the grain size distribution in the bed as weighting factor for the  
 1829 saturated sediment concentration (e.g. Delft3D-FLOW Manual, 2014, section 11.6.4).  
 1830 Using the grain size distribution at the bed surface as a weighting factor assumes, in  
 1831 case of erosion, that all sediment at the bed surface is equally exposed to the wind.

1832 Using the grain size distribution at the bed surface as weighting factor in case  
 1833 of deposition would lead to the behavior where deposition becomes dependent on  
 1834 the bed composition. Alternatively, in case of deposition, the saturated sediment  
 1835 concentration can be weighted based on the grain size distribution in the air. Due  
 1836 to the nature of saltation, in which continuous interaction with the bed forms the  
 1837 saltation cascade, both the grain size distribution in the bed and in the air are likely  
 1838 to contribute to the interaction between sediment fractions. The ratio between both  
 1839 contributions in the model is determined by a bed interaction parameter  $\zeta$ .

1840 The weighting of erosion and deposition of individual fractions is computed ac-  
 1841 cording to:

$$\hat{w}_k = \frac{w_k}{\sum_{k=1}^{n_k} w_k} \quad (4.10a)$$

$$\text{where } w_k = (1 - \zeta) \cdot w_k^{\text{air}} + (1 - \hat{S}_k) \cdot w_k^{\text{bed}} \quad (4.10b)$$

1842 in which  $k$  represents the sediment fraction index,  $n_k$  the total number of sediment  
 1843 fractions,  $w_k$  is the unnormalized weighting factor for fraction  $k$ ,  $\hat{w}_k$  is its normalized  
 1844 counterpart,  $w_k^{\text{air}}$  and  $w_k^{\text{bed}}$  are the weighting factors based on the grain size distribu-  
 1845 tion in the air and bed respectively and  $\hat{S}_k$  is the effective sediment saturation of the  
 1846 air. The weighting factors based on the grain size distribution in the air and the bed  
 1847 are computed using mass ratios:

$$w_k^{\text{air}} = \frac{c_k}{c_{\text{sat},k}} ; w_k^{\text{bed}} = \frac{m_{a,k}}{\sum_{k=1}^{n_k} m_{a,k}} \quad (4.11)$$

1848 The sum of the ratio  $w_k^{\text{air}}$  over the fractions denotes the degree of saturation of the  
 1849 air column for fraction  $k$ . The degree of saturation determines if erosion of a fraction  
 1850 may occur. Also in saturated situations erosion of a sediment fraction can occur due  
 1851 to an exchange of momentum between sediment fractions, which is represented by  
 1852 the bed interaction parameter  $\zeta$ . The effective degree of saturation is therefore also  
 1853 influenced by the bed interaction parameter and defined as:

$$\hat{S}_k = \min \left( 1 ; (1 - \zeta) \cdot \sum_{k=1}^{n_k} w_k^{\text{air}} \right) \quad (4.12)$$

1854 When the effective saturation is greater than or equal to unity the air is  
 1855 (over)saturated and no erosion will occur. The grain size distribution in the bed is  
 1856 consequently less relevant and the second term in Equation 4.10b is thus minimized  
 1857 and zero in case  $\zeta = 0$ . In case the effective saturation is less than unity erosion may  
 1858 occur and the grain size distribution of the bed also contributes to the weighting over  
 1859 the sediment fractions. The weighting factors for erosion are then composed from  
 1860 both the grain size distribution in the air and the grain size distribution at the bed  
 1861 surface. Finally, the resulting weighting factors are normalized to sum to unity over  
 1862 all fractions ( $\hat{w}_k$ ).

1863 The composition of weighting factors for erosion is based on the saturation of the  
 1864 air column. The non-saturated fraction determines the potential erosion of the bed.  
 1865 Therefore the non-saturated fraction can be used to scale the grain size distribution  
 1866 in the bed in order to combine it with the grain size distribution in the air according  
 1867 to Equation 4.10b. The non-saturated fraction of the air column that can be used for  
 1868 scaling is therefore  $1 - \hat{S}_k$ .

1869 For example, if bed interaction is disabled ( $\zeta = 0$ ) and the air is 70% saturated,  
 1870 then the grain size distribution in the air contributes 70% to the weighting factors  
 1871 for erosion, while the grain size distribution in the bed contributes the other 30%  
 1872 (Figure 4.1, upper left panel). In case of (over)saturation the grain size distribution  
 1873 in transport contributes 100% to the weighting factors and the grain size distribution  
 1874 in the bed is of no influence. Transport progresses in downwind direction without  
 1875 interaction with the bed.

1876 To allow for bed interaction in saturated situations in which no net erosion can  
 1877 occur, the bed interaction parameter  $\zeta$  is used (Figure 4.1). The bed interaction pa-  
 1878 rameter can take values between 0.0 and 1.0 in which the weighting factors for the  
 1879 equilibrium or saturated sediment concentration in an (over)saturated situation are  
 1880 fully determined by the grain size distribution in the bed or in the air respectively.  
 1881 A bed interaction value of 0.2 represents the situation in which the grain size distri-  
 1882 bution at the bed surface contributes 20% to the weighting of the saturated sediment  
 1883 concentration over the fractions. In the example situation where the air is 70% sat-  
 1884 urated such value for the bed interaction parameter would lead to weighting factors  
 1885 that are constituted for  $70\% \cdot (100\% - 20\%) = 56\%$  based on the grain size distribution  
 1886 in the air and for the other 44% based on the grain size distribution at the bed surface  
 1887 (Figure 4.1, upper right panel).

1888 The parameterization of the exchange of momentum between sediment fractions  
 1889 is an aspect of saltation that is still poorly understood. Therefore calibration of the  
 1890 bed interaction parameter  $\zeta$  is necessary. The model parameters in Equation 4.8 can  
 1891 be chosen in accordance with the assumptions underlying multi-fraction sediment

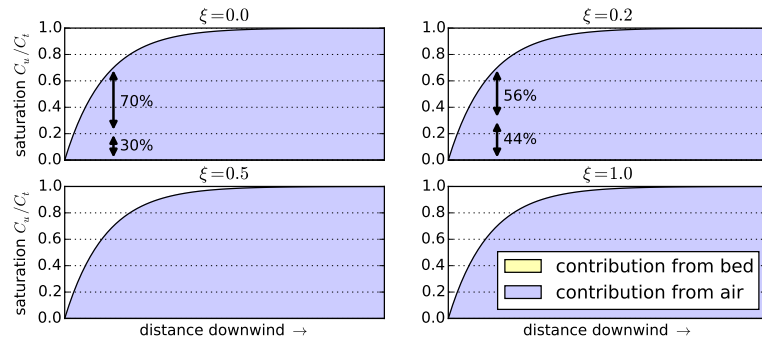


Figure 4.1: Contributions of the grain size distribution in the bed and in the air to the weighting factors  $w_k$  for the equilibrium sediment concentration in Equation 4.9 for different values of the bed interaction parameter.

1892 transport.  $C$  should be set to 1.5 as each individual sediment fraction is well-sorted,  $d_n$   
 1893 should be chosen equal to  $D_n$  as the grain size dependency is implemented through  
 1894  $u_{th}$ .  $u_{th}$  typically varies between 1 and 6 m/s for sand.

#### 1895 4.4.3 Simulation of Sediment Sorting and Beach Armoring

1896 Since the equilibrium or saturated sediment concentration  $c_{sat,k}$  is weighted over mul-  
 1897 tiple sediment fractions in the extended advection model, also the instantaneous sed-  
 1898 iment concentration  $c_k$  is computed for each sediment fraction individually. Conse-  
 1899 quently, grain size distributions may vary over the model domain and in time. These  
 1900 variations are thereby not limited to the horizontal, but may also vary over the verti-  
 1901 cal since fine sediment may be deposited on top of coarse sediment or, reversely, fines  
 1902 may be eroded from the bed surface leaving coarse sediment to reside on top of the  
 1903 original mixed sediment. In order to allow the model to simulate the processes of  
 1904 sediment sorting and beach armoring the bed is discretized in horizontal grid cells  
 1905 and vertical bed layers (2DV; Figure 4.2).

1906 The discretization of the bed consists of a minimum of three vertical bed layers with  
 1907 a constant thickness and an unlimited number of horizontal grid cells. The top layer  
 1908 is the *bed surface layer* and is the only layer that interacts with the wind and hence  
 1909 determines the spatiotemporal varying sediment availability and the contribution of  
 1910 the grain size distribution in the bed to the weighting of the saturated sediment con-  
 1911 centration. One or more *bed composition layers* are located underneath the bed surface  
 1912 layer and form the upper part of the erodible bed. The bottom layer is the *base layer*  
 1913 and contains an infinite amount of erodible sediment according to the initial grain  
 1914 size distribution. The base layer cannot be eroded, but can supply sediment to the  
 1915 other layers.

1916 Each layer in each grid cell describes a grain size distribution over a predefined  
 1917 number of sediment fractions (Figure 4.2, detail). Sediment may enter or leave a grid  
 1918 cell only through the bed surface layer. Since the velocity threshold depends among

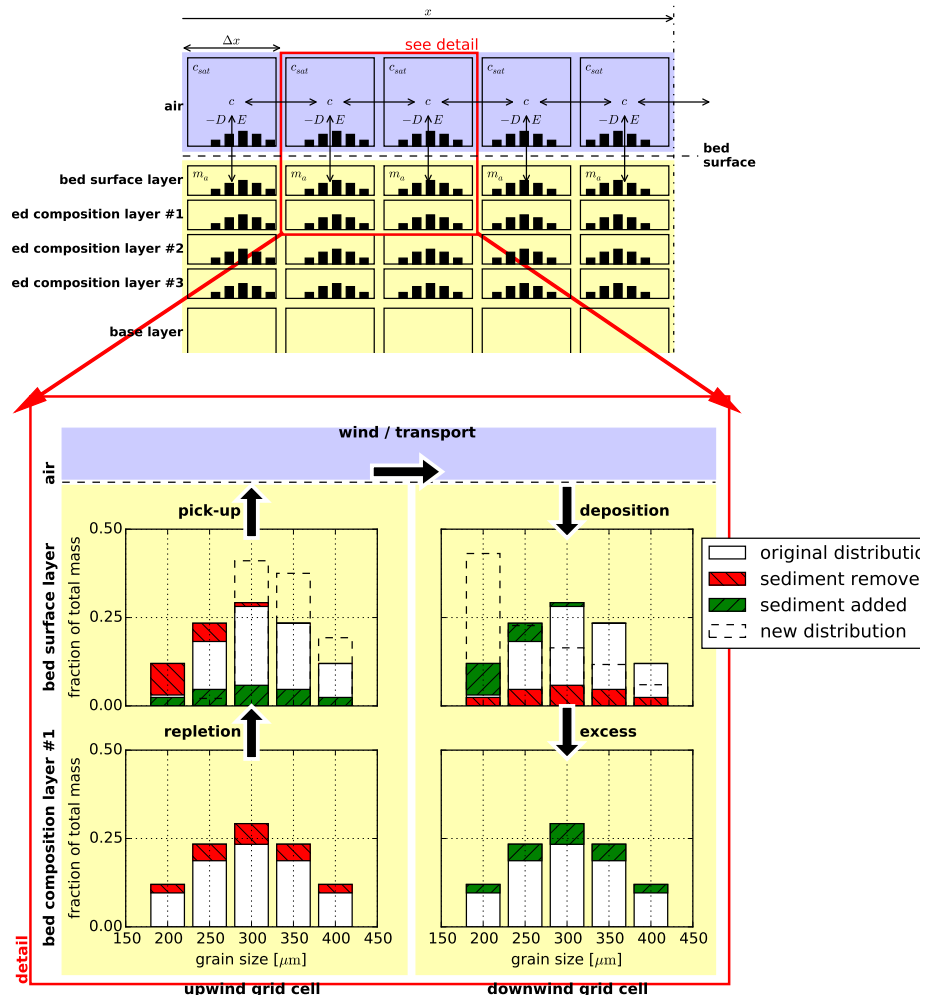
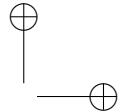
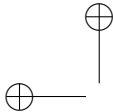


Figure 4.2: Schematic of bed composition discretisation and advection scheme. Horizontal exchange of sediment may occur solely through the air that interacts with the *bed surface layer*. The detail presents the simulation of sorting and beach armoring where the bed surface layer in the upwind grid cell becomes coarser due to non-uniform erosion over the sediment fractions, while the bed surface layer in the downwind grid cell becomes finer due to non-uniform deposition over the sediment fractions. Symbols refer to Equations 4.6 and 4.7.



1919 others on the grain size, erosion from the bed surface layer will not be uniform over  
 1920 all sediment fractions, but will tend to erode fines more easily than coarse sediment  
 1921 (Figure 4.2, detail, upper left panel). If sediment is eroded from the bed surface layer,  
 1922 the layer is repleted by sediment from the lower bed composition layers. The repleted  
 1923 sediment has a different grain size distribution than the sediment eroded from the  
 1924 bed surface layer. If more fines are removed from the bed surface layer in a grid cell  
 1925 than repleted, the median grain size increases. If erosion of fines continues the bed  
 1926 surface layer becomes increasingly coarse. Deposition of fines or erosion of coarse  
 1927 material may resume the erosion of fines from the bed.

1928 In case of deposition the process is similar. Sediment is deposited in the bed surface  
 1929 layer that then passes its excess sediment to the lower bed layers (Figure 4.2, detail,  
 1930 upper right panel). If more fines are deposited than passed to the lower bed layers  
 1931 the bed surface layer becomes increasingly fine.

#### 1932 4.4.4 *Simulation of the Emergence of Non-erodible Roughness Elements*

1933 Sediment sorting may lead to the emergence of non-erodible elements from the bed.  
 1934 Non-erodible roughness elements may shelter the erodible bed from wind erosion  
 1935 due to shear partitioning, resulting in a reduced sediment availability (Raupach et al.,  
 1936 1993). Therefore Equation 4.2 is implemented according to:

$$u_{*th,R} = u_{*th} \cdot \sqrt{\left(1 - m \cdot \sum_{k=k_0}^{n_k} w_k^{\text{bed}}\right) \left(1 + \frac{m\beta}{\sigma} \cdot \sum_{k=k_0}^{n_k} w_k^{\text{bed}}\right)} \quad (4.13)$$

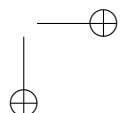
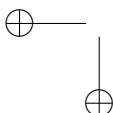
1937 in which  $\sigma$  is the ratio between the frontal area and the basal area of the roughness  
 1938 elements and  $\beta$  is the ratio between the drag coefficients of the roughness elements  
 1939 and the bed without roughness elements.  $m$  is a factor to account for the difference  
 1940 between the mean and maximum shear stress and is usually chosen 1.0 in wind tunnel  
 1941 experiments and may be lowered to 0.5 for field applications. The roughness density  
 1942  $\lambda$  in the original equation of Raupach et al. (1993, Equation 4.2) is obtained from the  
 1943 mass fraction in the bed surface layer  $w_k^{\text{bed}}$  (Equation 4.11) according to:

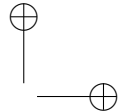
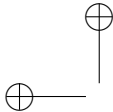
$$\lambda = \frac{\sum_{k=k_0}^{n_k} w_k^{\text{bed}}}{\sigma} \quad (4.14)$$

1944 in which  $k_0$  is the index of the smallest non-erodible sediment fraction in current  
 1945 conditions and  $n_k$  is the total number of sediment fractions. It is assumed that the  
 1946 sediment fractions are ordered by increasing size. Whether a fraction is erodible  
 1947 depends on the sediment transport capacity.

#### 1948 4.4.5 *Simulation of the Hydraulic Mixing, Infiltration and Evaporation*

1949 As sediment sorting due to aeolian processes can lead to armoring of a beach sur-  
 1950 face, mixing of the beach surface or erosion of course material may undo the effects  
 1951 of armoring. To ensure a proper balance between processes that limit and enhance  
 1952 sediment availability in the model both types of processes need to be sufficiently repre-  
 1953 sented when simulating spatiotemporal varying bed surface properties and sediment  
 1954 availability.





1955 A typical upwind boundary in coastal environments during onshore winds is the  
 1956 water line. For aeolian sediment transport the water line is a zero-transport bound-  
 1957 ary. In the presence of tides, the intertidal beach is flooded periodically. Hydraulic  
 1958 processes like wave breaking mix the bed surface layer of the intertidal beach, break  
 1959 the beach armoring and thereby influence the availability of sediment. Moreover, the  
 1960 hydraulic processes periodically wet the intertidal beach temporally increasing the  
 1961 shear velocity threshold. Infiltration and evaporation subsequently dry the beach.

1962 In the model the mixing of sediment is simulated by averaging the sediment dis-  
 1963 tribution over the depth of disturbance ( $\Delta z_d$ ). The depth of disturbance is linearly  
 1964 related to the breaker height (e.g. King, 1951; Williams, 1971; Masselink et al., 2007).  
 1965 Masselink et al. (2007) proposes an empirical factor  $f_{\Delta z_d}$  [-] that relates the depth of  
 1966 disturbance directly to the local breaker height according to:

$$\Delta z_d = f_{\Delta z_d} \cdot \min(H ; \gamma \cdot d) \quad (4.15)$$

1967 in which the offshore wave height  $H$  [m] is taken as the local wave height maximized  
 1968 by a maximum wave height over depth ratio  $\gamma$  [-].  $d$  [m] is the water depth that is  
 1969 provided to the model through an input time series of water levels. Typical values for  
 1970  $f_{\Delta z_d}$  are 0.05 to 0.4 and 0.5 for  $\gamma$ .

1971 The drying of the beach is simulated by simplified functions for infiltration and  
 1972 evaporation. Infiltration is represented by an exponential decay function that is gov-  
 1973 erned by a drying time scale  $T_{dry}$ . Evaporation is simulated using an adapted version  
 1974 of the Penman-Monteith equation (Shuttleworth, 1993) that is governed by meteoro-  
 1975 logical time series of solar radiation, temperature and humidity.

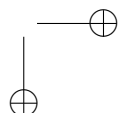
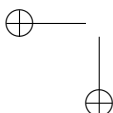
#### 1976 4.5 RESULTS

1977 The model is applied to a series of prototype cases to illustrate the processes de-  
 1978 scribed by the model, two wind tunnel experiments to illustrate the capabilities of the  
 1979 model to simulate spatiotemporal variations in bed surface properties and sediment  
 1980 availability and a sensitivity analysis.

##### 1981 4.5.1 Prototype cases

1982 The four prototype cases P<sub>1</sub> to P<sub>4</sub> are intended to illustrate the capabilities of the  
 1983 presented model to simulate processes of sediment sorting (van der Wal, 2000; Arens  
 1984 et al., 2002) and beach armoring (van der Wal, 1998). The prototype cases are con-  
 1985 structed using a 120 m schematized linear beach with a 1:20 slope, a wind velocity  
 1986 of 12 or 30 m/s, a drying time scale  $T_{dry}$  of 3 h, constant evaporation and a simula-  
 1987 tion time of 30 days. The prototype cases are initialized with lognormally distributed  
 1988 sediment with  $d_{50} = 335 \mu\text{m}$  ( $\Phi$  – scale = 1.6,  $\sigma_\Phi = 0.4$ ), which is representative  
 1989 for nourished poorly sorted beaches along the Dutch coast. Parameterizations for  
 1990 shells and shell fragments in Equation 4.13 are based on experiments described by  
 1991 McKenna Neuman et al. (2012) and chosen as  $m = 0.5$ ,  $\sigma = 4.2$  and  $\beta = 130$ . The four  
 1992 scenarios described by the prototype cases are:

1993 P<sub>1</sub> This scenario is used as reference for normalization and involves sand only and no  
 1994 tidal movement. The model is forced by a constant wind of 12 m/s. Sediment



1995 sorting occurs due to the presence of a wide range of sediment fractions. How-  
 1996 ever, beach armoring does not occur due to the absence of shells, resulting in an  
 1997 almost constant sediment transport rate at the downwind end of the domain.

- 1998 p2 This scenario involves 5% of shells and shell fragments ranging from 2 to 30 mm  
 1999 and no tidal movement. The model is forced by a constant wind of 12 m/s. The  
 2000 presence of shells means that beach armoring occurs that causes spatiotemporal  
 2001 variations in sediment availability and a decrease in sediment transport.
- 2002 p3 This scenario involves 5% of shells and shell fragments and a sinusoidal tide with  
 2003 a 2 m tidal range and a tidal period of 12 h. The tide periodically floods a 40 m  
 2004 intertidal beach area. The model is forced by a constant wind of 12 m/s. The  
 2005 tidal movement causes mixing of the bed surface layer in the intertidal beach  
 2006 area reducing the effects of beach armoring.
- 2007 p4 This scenario is equal to scenario P<sub>3</sub>, but the model is forced by a wind of 12  
 2008 m/s that is increased twice to 30 m/s to simulate the effect of higher energy  
 2009 wind events that (partially) reset the composition of the bed surface layer and  
 2010 temporarily increase the sediment availability in the dry beach area.

2011 Figure 4.3 presents the simulated aeolian sediment transport rates at the downwind  
 2012 end of the domain for cases P<sub>2</sub> to P<sub>4</sub> over the course of 30 days of simulation time.  
 2013 The results are normalized using the transport rate in case P<sub>1</sub>. The reference case  
 2014 P<sub>1</sub> shows an almost constant transport rate over the entire course of the simulation.  
 2015 The presence of shells in case P<sub>2</sub> results in a reduction of sediment availability. As  
 2016 a result, the transport rates in case P<sub>2</sub> are lower compared to case P<sub>1</sub>. The transport  
 2017 rate decreases as more shells emerge from the bed and a beach armor layer develops.  
 2018 In case P<sub>2</sub> there are no processes that break the armoring and the transport rates  
 2019 asymptotically reach zero. The beach armor layer develops in direction of the wind.  
 2020 Therefore, the relative contribution of the downwind part of the beach ( $x \geq 40$ ) to the  
 2021 total sediment transport increases over time.

2022 Case P<sub>3</sub> includes tidal movement and hydraulic mixing. At the high water line the  
 2023 sediment transport is zero during high tide and maximized during low tide. Initially,  
 2024 transport is not saturated at the high water line and entrainment of sediment contin-  
 2025 ues over the dry beach. As shells emerge from the bed, a beach armor layer develops  
 2026 that reduces sediment availability. The reduction of sediment availability progresses  
 2027 slower at the intertidal beach compared to the dry beach due to hydraulic mixing.  
 2028 After 8 days the sediment transport rates at the high water line start to exceed the  
 2029 sediment transport rates at the dune foot during low water. Sediment that is eroded  
 2030 from the intertidal beach during low water is partially trapped at the dry beach due to  
 2031 differences in roughness. During subsequent high water, when the sediment supply  
 2032 from the intertidal beach ceases, these deposits are again entrained and blown down-  
 2033 wind. The net erosion from the dry beach ultimately approaches zero as armoring  
 2034 of the dry beach progresses. At this point all sediment deposited downwind origi-  
 2035 nates directly from the intertidal beach. However, due to the spatial differences in  
 2036 roughness, sediment is temporally deposited at the dry beach and cause the sediment  
 2037 transport rates at the dune foot to be only weakly correlated with the tidal movement.

2038 Case P<sub>4</sub> shows a pattern similar to case P<sub>3</sub>, but after 8 and 16 days a relatively high-  
 2039 energy wind event passes for 24 hours. As a result, the transport rate spikes, but an

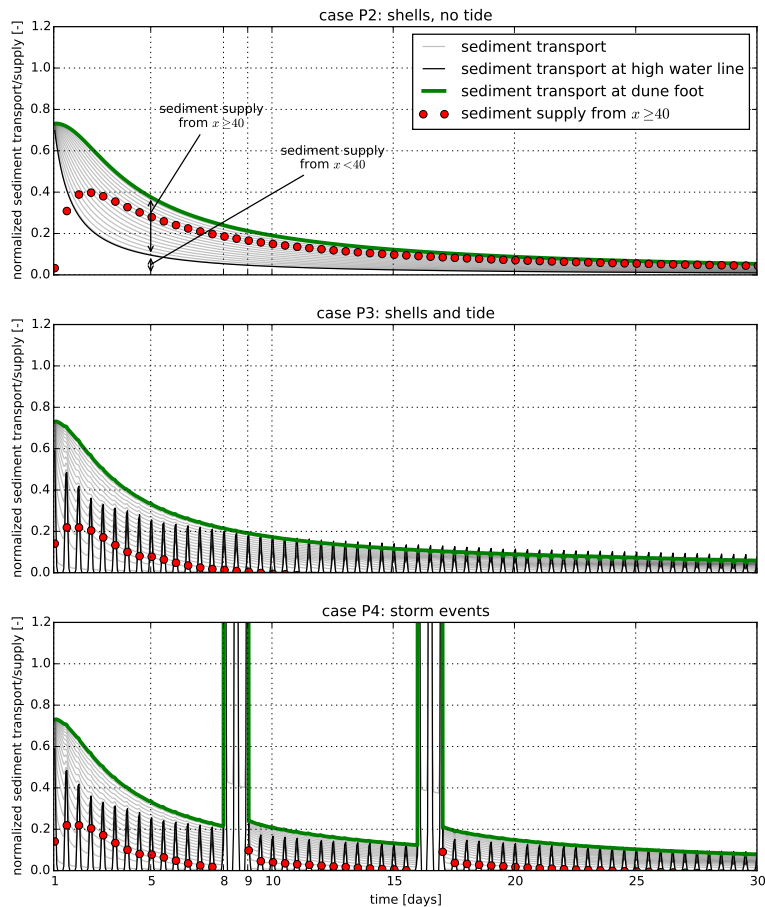


Figure 4.3: Sediment transport in time and over the model domain for three scenarios with constant wind. Each line depicts a different location along the beach, starting from  $x = 40$  m, which coincides with the high water line in cases P<sub>3</sub> and P<sub>4</sub>, and ends at the dune foot. Results are normalized using the transport rate in case P<sub>1</sub> with almost constant transport (not shown). The difference between the sediment transport at dune foot (green) and the sediment transport at  $x = 40$  m is visualized by the red dots and represents the sediment supply from the dry beach. In cases P<sub>3</sub> and P<sub>4</sub> the sediment transport at the high water line periodically exceeds the sediment transport at the dune foot, indicating local deposition of sediments originating from the intertidal beach.

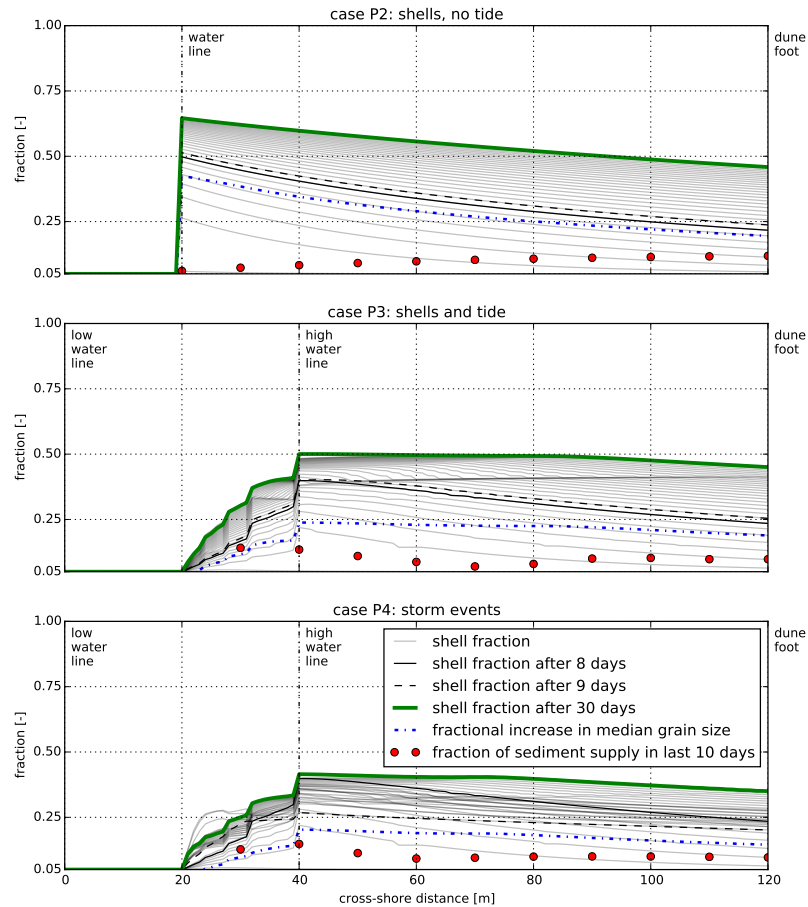


Figure 4.4: Distribution of the shell fraction over the model domain and in time. Sediment supply is inversely related to the degree of beach armoring, indicated by the shell fraction. Median grain size increases with the increase in shell fraction indicating erosion of predominantly fines. High-energy wind events in case P<sub>4</sub> even mobilize shell fractions resulting in a decrease in beach armoring and an increase in sediment availability.

2040 elevated transport rate is also visible after the wind velocity drops. During the high-  
 2041 energy wind event even small shell fragments are mobilized. The beach armoring  
 2042 is therefore (partially) removed and more sediment is available for transportation  
 2043 afterwards. This leads to a prolonged peak in sediment transport and an increase of  
 2044 the relative contribution of the dry beach to the total sediment transport at the dune  
 2045 foot. After the beach armoring is re-established over time the transport rates approach  
 2046 the rates of case P3 again.

2047 The differences in transport rate between the prototype cases are directly related  
 2048 to sediment availability, since the wind is constant in all cases but case P4. Figure  
 2049 4.4 shows the fractions of shells and shell fragments in the bed surface layer for case  
 2050 P2 to P4. The shell fraction increases over time in all simulations. In case P2 the  
 2051 shell fraction peaks at the water line as the beach armor layer develops in downwind  
 2052 direction. Consequently, at the end of the simulation most sediment originates from  
 2053 the downwind end of the beach where the beach armoring is least developed. In  
 2054 case P3 and P4 hydraulic mixing causes the shell fraction in the intertidal beach to  
 2055 remain low resulting in a different distribution of shells compared to case P2 and  
 2056 hence a difference in sediment availability. Consequently, at the end of the simulation  
 2057 most sediment originates from the intertidal beach. In reality, the contribution of the  
 2058 intertidal beach to the total sediment transport is likely to be higher as more marine  
 2059 processes counteract the local development of a beach armor layer than currently  
 2060 simulated, like marine deposits and buoyancy of shells. In case P4 the drop in shell  
 2061 fraction from day 8 to day 9 is related to the first high-energy wind event. At the end  
 2062 of the simulation, the fraction of sediment that originates from the intertidal beach is  
 2063 relatively low compared to case P3. In all cases also the median grain size in the bed  
 2064 surface layer increases, indicating that predominantly fine sediment is eroded from  
 2065 the bed. The unbalanced sediment transport over the fractions cause sediment sorting  
 2066 in downwind direction.

2067 The contribution to the instantaneous sediment transport of the specific processes  
 2068 described by the model can be distinguished in the prototype cases P1 to P4 because  
 2069 a constant wind velocity is imposed. If a more realistic variable wind velocity time  
 2070 series is used, the contributions of the specific processes are obscured by the wind-  
 2071 related variance. To show that the simulation of spatiotemporal bed surface properties  
 2072 and sediment are also important in variable wind conditions, prototype cases P1 to  
 2073 P3 are repeated using an synthetic variable wind time series (P1b to P3b). The time  
 2074 series is generated using a Markov Chain Monte Carlo (MCMC) simulation following  
 2075 a Weibull distribution with a mean wind velocity of 12 m/s.

2076 Figure 4.5 shows the sediment transport rate in case P3b normalized by the sedi-  
 2077 ment transport rate in case P1b depending on the hourly averaged wind velocity. To  
 2078 remove the influence of the wind variability, the normalized sediment transport time  
 2079 series obtained from the simulations are binned according to the hourly averaged  
 2080 wind velocity in 0.5 m/s bins. The median transport rate in each bin is subsequently  
 2081 determined to obtain a relation between instantaneous normalized sediment transport  
 2082 and wind velocity. The reduction is close to 100% up to wind velocities of 5 m/s and  
 2083 subsequently decreases according to an exponential function. The median reduction  
 2084 for 12 m/s wind velocity is 74%, which is less than the maximum reduction of 95.0%  
 2085 with a constant 12 m/s wind velocity in case P3. The reduction tends to increase  
 2086 during the simulation as beach armoring progresses.

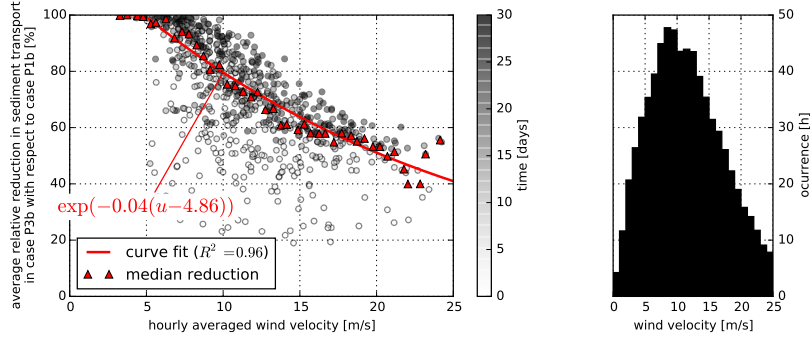


Figure 4.5: Average reduction in sediment transport in prototype case P3b compared to case P1b depending on the hourly averaged wind velocity (left panel). The results are obtained using an synthetic variable wind time series following a Weibull distribution with a mean wind velocity of 12 m/s (right panel). The sediment transport reduction (scatter) is binned according to the wind velocity using 0.5 m/s bins. The median reduction per bin (triangles) is used to fit an exponential curve (line). The reduction tends to increase during the simulation (scatter colors).

#### 2087 4.5.2 Wind tunnel experiments

2088 To illustrate the applicability of the model approach, two unrelated wind tunnel experiments  
 2089 obtained from literature are simulated that involve either temporal ([Nickling](#)  
 2090 and [McKenna Neuman, 1995](#)) or spatial ([Dong et al., 2004b](#)) variations in bed surface  
 2091 properties as discussed in section 4.2.

2092 [Nickling and McKenna Neuman \(1995\)](#) describe an experiment in a wind tunnel  
 2093 with a 4.5 m working section in which a grid of 18 mm marbles was buried in sandy  
 2094 material with  $d_{50} = 270 \mu\text{m}$ . During the experiment with constant wind of 8 m/s,  
 2095 measured at 25 cm above the bed, the sand is winnowed from in between the marbles  
 2096 resulting in the emergence of the marbles over time. The emergence of the marbles  
 2097 cause the bed to become armored. The effect of armoring of a marble extends beyond  
 2098 the marble dimensions due to shadowing effects in the lee of the marble described  
 2099 by Equation 4.13. All parameter values, including  $z'$ , are obtained from [Nickling and](#)  
 2100 [McKenna Neuman \(1995\)](#) and hence no further calibration of parameters is performed  
 2101 for this simulation.

2102 Figure 4.6 shows the modeled normalized sediment transport rate in comparison  
 2103 with the measurements described in [Nickling and McKenna Neuman \(1995\)](#). Where  
 2104 the measurements start with a relatively constant transport and even a slight increase  
 2105 in transport, the model predicts an immediate decrease in transport. The marbles  
 2106 are modeled as a large sediment fraction for which its presence in a bed composition  
 2107 layer is described by a mass fraction rather than a location. Therefore, it is possible  
 2108 to define the marble density, but not the exact marble locations. Consequently, from  
 2109 the start of the simulation marbles start to emerge from the bed resulting in an im-  
 2110 mediate decrease in sediment transport. In contrast, in the wind tunnel the marbles

2111 are covered with a thin layer of sand that was removed first before the marbles start  
 2112 to emerge. The initial emergence of the marbles coincided with a slight increase in  
 2113 sediment transport. Nickling and McKenna Neuman (1995) attributes this rise to a  
 2114 pronounced change in boundary conditions and turbulence. Since these small scale  
 2115 variations in the wind shear are not represented in the model the rise in transport  
 2116 is not visible in the model results. However, the decrease in sediment transport due  
 2117 to the emergence of the marbles for the three different grid spacings described in  
 2118 Nickling and McKenna Neuman (1995), is qualitatively represented by the model.

2119 Dong et al. (2004b) describe an experiment in a wind tunnel with a 21 m working  
 2120 section in which a patch of gravel with diameter 10 – 40 mm was positioned down-  
 2121 wind of a sandy bed with  $d_{50} = 180 \mu\text{m}$ . The length of the gravel patch was varied  
 2122 between the experiments from 0.5 – 12 m and the wind velocity from 8 – 22 m/s,  
 2123 measured at 60 cm above the bed. The free-flow wind velocities are converted to  
 2124 shear velocities assuming  $z' = 6 \text{ mm}$ . The gravel patch traps saltating grains. In the  
 2125 model the entrapment of grains is simulated as an exchange of momentum between  
 2126 the sandy fractions and the immobile gravel fraction. This exchange is governed by  
 2127 the bed interaction parameter, which is calibrated for this simulation and found to be  
 2128 0.05.

2129 Figure 4.7 shows the modeled sediment transport rate in comparison with the mea-  
 2130 surements described in Dong et al. (2004b). The increase in sediment transport with  
 2131 increasing wind velocity is well represented by the model given the uniform RMSE  
 2132 among the different wind velocities. The decrease in sediment transport rate with in-  
 2133 creasing gravel patch length is represented by the model with a relative RMSE of less  
 2134 than 10% for all except the lowest and highest wind velocities. Significant surpassing  
 2135 of sediment over the sediment trap during the measurements with 22 m/s wind veloc-  
 2136 ity is reported by Dong et al. (2004b), which explains the consistent overprediction of  
 2137 the sediment fluxes by the model. The discrepancy between the model and the mea-  
 2138 surements for the 8 and 10 m/s wind velocities is less consistent and is expected to  
 2139 be a result of a low signal-to-noise ratio related to the small sediment fluxes. Also for  
 2140 short gravel patch lengths the model deviates from the measurements. The relatively  
 2141 high variability over the 0.5 to 2 m gravel patch lengths is attributed to a change in  
 2142 transport characteristics (Dong et al., 2004b) due to fully elastic collisions between the  
 2143 sand grains and the gravel. A bed interaction parameter that is not constant is needed  
 2144 to capture this behavior in the model.

#### 2145 4.5.3 Sensitivity

2146 The sensitivity of the model to four newly introduced parameters and the wind veloc-  
 2147 ity is determined to obtain insight in the importance of these parameters to the model  
 2148 results. The newly introduced parameters are the bed interaction parameter, depth of  
 2149 disturbance factor, the drying time scale and the grain size distribution standard devi-  
 2150 ation. Case P3 as presented in section 4.5.1 is used as starting point for the sensitivity  
 2151 analysis. Figure 4.8 shows the change in normalized total sediment transport given  
 2152 variations of each of the four model parameters and the wind velocity.

2153 The bed interaction parameter, the depth of disturbance factor and the drying time  
 2154 scale affect the source area of aeolian sediment (Figure 4.8a, b and c). In absence  
 2155 of bed interaction all sediment entrained in the intertidal beach area is being trans-

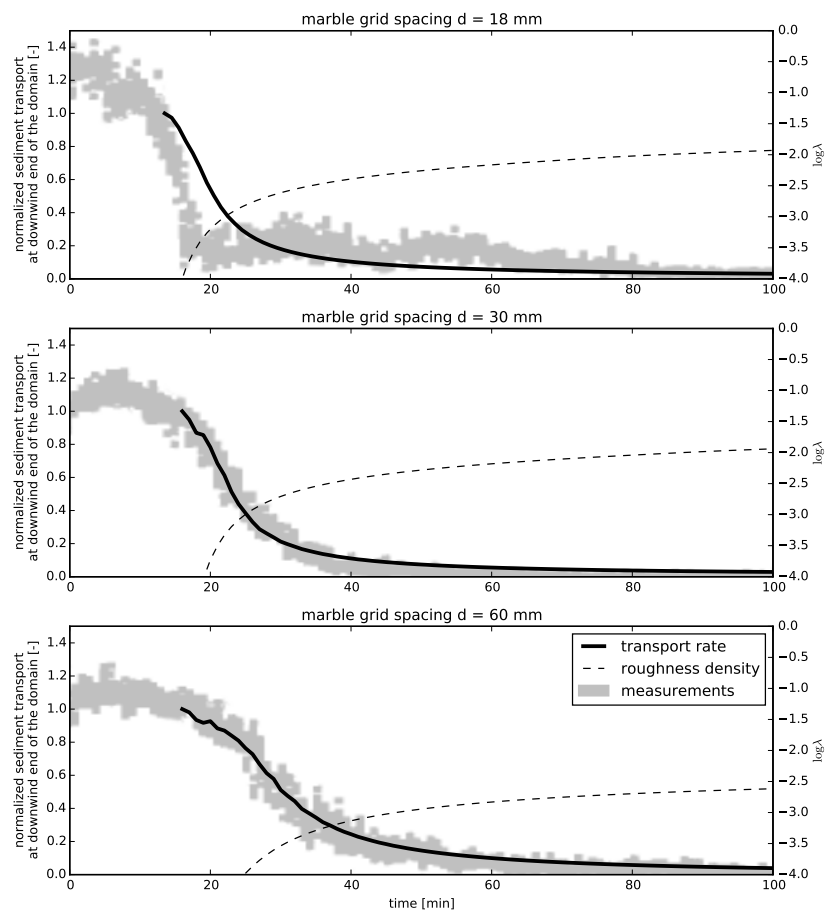


Figure 4.6: Comparison between modeled and measured normalized sediment transport rates from wind tunnel experiments described in [Nickling and McKenna Neuman \(1995\)](#). The dashed line depicts the emergence of marbles in terms of increasing roughness density. The visualization of the measurement results is copied from Figure 4 in the original publication without digitization.

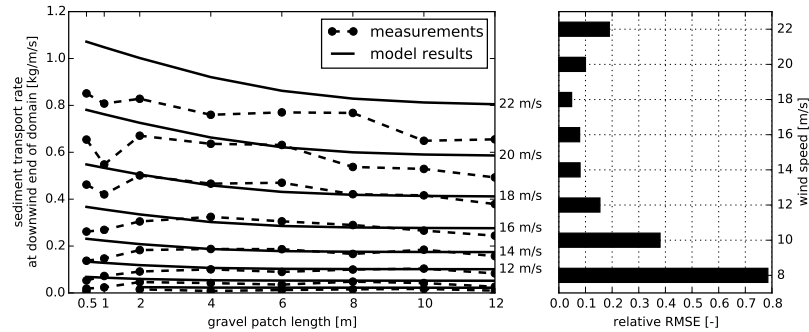


Figure 4.7: Comparison between model results and measurements from wind tunnel experiments described in Dong et al. (2004b) (left panel) and RMS errors relative to the mean measured transport rate (right panel). The measured transport rates with a wind velocity of 22 m/s are underestimated due to surpassing of sediment over the sediment trap (Dong et al., 2004b).

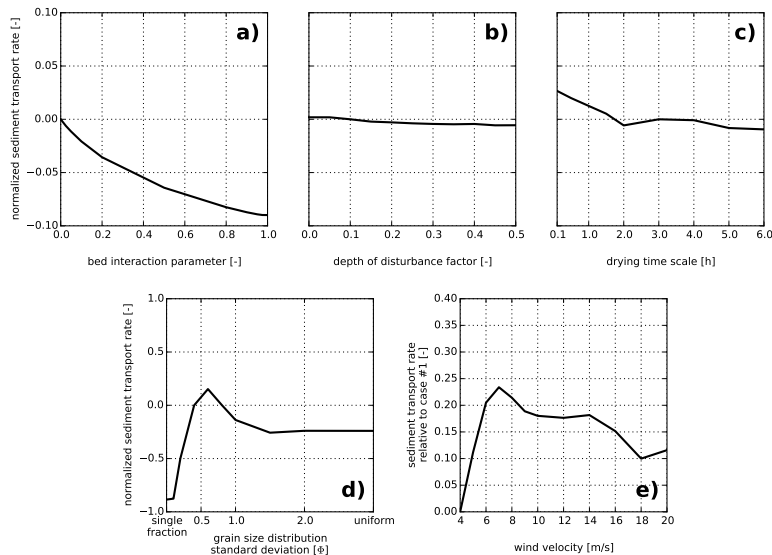


Figure 4.8: Sensitivity of the total normalized sediment transport with respect to case P3 for four newly introduced parameters and the wind velocity. The sensitivity of the wind velocity is expressed with respect to the transport rate in case P1.

2156 ported to the downwind end of the domain unhindered. In contrast, in the presence  
2157 of bed interaction sediment from the intertidal beach area may be trapped in the beach  
2158 armor layer that is being developed in the dry beach area during the simulation. Con-  
2159 sequently, the total sediment transport reduces with increasing bed interaction. The  
2160 bed interaction parameter parameterizes the exchange between sediment fractions,  
2161 which is an aspect of saltation that is still poorly understood. In particular situations  
2162 with a large spatial variability in bed surface properties the bed interaction parameter  
2163 is expected to show a more significant sensitivity (e.g. Dong et al., 2004b). Therefore  
2164 calibration of the bed interaction parameter is necessary in such situations.

2165 The depth of disturbance factor shows no significant sensitivity as aeolian sediment  
2166 supply from the intertidal beach is concentrated close to the water line where wave  
2167 heights are negligible. Lower parts of the intertidal beach are continuously too moist  
2168 for sediment to be entrained. The sensitivity to the depth of disturbance factor in-  
2169 creases with decreasing drying time scale, but typically only for values smaller than  
2170 0.5 m. The sensitivity to the drying time scale shows that for time scales larger than  
2171 several hours the intertidal beach is continuously too moist for sediment to be en-  
2172 trained. For small drying time scales the intertidal beach supplies aeolian sediment  
2173 that contains relatively many fines, resulting in a slight increase in total sediment  
2174 transport.

2175 From the sensitivity of the grain size distribution width, represented by the grain  
2176 size distribution standard deviation and strictly speaking not a model parameter, it  
2177 can be concluded that the introduction of multiple sediment fractions has a signifi-  
2178 cant impact on the sediment transport rate (Figure 4.8d). However, for poorly sorted  
2179 sediments the sensitivity of the model to the distribution width is limited. Beyond a  
2180 standard deviation of  $\sigma_\Phi = 1.5$  the development of the sediment rate is similar to the  
2181 transport rate with a uniform distribution.

2182 The rate of armoring depends on the presence of non-erodible sediment fractions.  
2183 Whether a sediment fraction is erodible depends on the wind transport capacity.  
2184 Therefore the rate of armoring and consequently the instantaneous sediment avail-  
2185 ability depends on the wind velocity. Figure 4.8e depicts the sediment transport rate  
2186 in case P3 with respect to the almost constant transport rate in case P1 for different  
2187 wind velocities. For low wind velocities all shell fractions can contribute to the es-  
2188 tablishment of a beach armor layer, but the beach armor layer develops slowly as  
2189 the winnowing of fines is dependent on the entrainment rate. For high wind veloci-  
2190 ties even shell fragments may be mobilized, but the beach armor layer consisting of  
2191 larger shells is developed quickly. Consequently, the reduction of sediment transport  
2192 is present over all wind velocities and 83% on average.

2193 4.6 DISCUSSION

2194 Process-based simulation of bed surface properties and sediment supply provides  
2195 an alternative for complex spatiotemporal parameterizations. Nevertheless, process-  
2196 based simulation itself requires parameterization, calibration and validation. These  
2197 parameterizations are generally less complex as they describe static properties rather  
2198 than spatiotemporal varying processes.

2199 4.6.1 *Parameterization*

2200 Compared to existing models for availability-limited aeolian sediment transport the  
2201 need for complex parameterization has been reduced in the presented model. The  
2202 adoption of the advection model of [de Vries et al. \(2014b\)](#) makes parameterization of  
2203 spatiotemporal variations in the shear velocity threshold, like attempted by [Nickling](#)  
2204 and [McKenna Neuman \(1995\)](#), [Dong et al. \(2004b\)](#) and others, unnecessary. In addi-  
2205 tion, process-based simulation of bed surface properties makes parameterization of  
2206 the inherently time-varying sediment availability  $m_a$  unnecessary. Existing parame-  
2207 terizations for the shear velocity threshold under influence of moisture, vegetation,  
2208 sediment sorting and other bed surface properties are still valid for the instantaneous  
2209 shear velocity threshold.

2210 Despite the efforts to minimize complex parameterizations that are difficult to gen-  
2211 eralize, the model also introduces new parameterizations that are specifically related  
2212 to the process-based simulation of sediment availability, i.e. the bed interaction pa-  
2213 rameter, depth of disturbance and soil drying time scale. The depth of disturbance  
2214 and soil drying time scale could easily be replaced by process-based simulation as  
2215 there is thorough knowledge on near-shore morphodynamics and beach hydrology.  
2216 Moreover, the presented model framework allows for spatiotemporal variations of pa-  
2217 rameters that are known not to be constant (e.g.  $z'$ ). However, these considerations  
2218 are outside the scope of this paper and will be part of future research.

2219 4.6.2 *Calibration*

2220 The calibration of the parameters involved in process-based simulation of sediment  
2221 availability is a relatively new field of research. In this paper a pragmatic approach  
2222 to calibration of these parameters is adopted, but there are various opportunities for  
2223 improvement. For example, the depth of disturbance is used to approximate the  
2224 mixing of the intertidal beach surface by waves. [Masselink et al. \(2007\)](#) shows how  
2225 the depth of disturbance can be determined based on a linear relation with the local  
2226 wave height. The mixing of the intertidal beach surface is particularly important as it  
2227 breaks beach armoring. The depth of disturbance does not provide any information  
2228 about how the bed is disturbed, just over which depth. Moreover, aspects like ma-  
2229 rine deposits and shell buoyancy also affect the sediment availability in the intertidal  
2230 beach area. [Gallagher et al. \(2011\)](#) presented detailed measurements of spatiotemporal  
2231 variations in the bed surface grain size at Truc Vert, France. The intertidal beach ap-  
2232 pears to be consistently finer than the upper beach. The measurements are obtained  
2233 using macrophotography ([Buscombe et al., 2010](#)) ensuring that the measurements  
2234 solely involve the beach surface. These type of measurements may provide a much  
2235 more detailed calibration of the hydraulic mixing simulated in the model, although it  
2236 might be questioned if such detailed hydraulic calibration is still within the scope of  
2237 an aeolian sediment transport model. Alternatively, the calibration of the hydraulic  
2238 mixing could be left to dedicated near-shore models (e.g. XBeach; [Roelvink et al.,](#)  
2239 [2009; Reniers et al., 2013](#)) and online model coupling could be used to incorporate  
2240 detailed near-shore hydro- and morphodynamics in the proposed aeolian modeling  
2241 framework.

2242 Similarly, an exponential decay function with a constant drying time scale is cur-  
2243 rently used to approximate the influence of the hydrological process of infiltration.  
2244 The exponential decay is a simplified approach that was adopted after it appeared to  
2245 be a reasonable approximation of numerical model results obtained with the HYDRUS  
2246 model (Simének et al., 1998) that simulates the soil moisture contents in the unsatu-  
2247 rated zone following van Genuchten (1978). Detailed measurements for calibration  
2248 of the instantaneous soil moisture can be obtained relatively easy using either in-situ  
2249 or remote infra-red or microwave measurements (e.g. Edwards et al., 2013; Hoonhout  
2250 et al., 2014a). Again, it might be questioned if the amount of detail involved in using  
2251 these kind of data for estimates of the bed surface moisture is still within the scope of  
2252 an aeolian sediment transport model.

2253 In contrast to the depth of disturbance and the drying rate, the bed interaction  
2254 parameter has little relation with existing literature. In essence, the bed interaction  
2255 parameter describes the exchange of momentum between grain size fractions along  
2256 the fetch distance. Specifically it describes whether impacting grains eject other grains  
2257 from the bed or that they are rebounded due to fully elastic collisions with large, non-  
2258 erodible elements. A low value for the bed interaction parameter would indicate a  
2259 large number of rebounding grains, while a high value would indicate a low num-  
2260 ber of rebounding grains. Typically, the number of rebounded grains increases with  
2261 an increasing number of non-erodible, large elements in the bed. Consequently, the  
2262 bed interaction parameter is not uniform over the fractions. Moreover, due to beach  
2263 armoring the bed interaction is neither constant over time nor in space. In this paper  
2264 the bed interaction parameter is pragmatically assumed to be uniform and constant  
2265 since no basis for differentiation of the parameter is currently available. Thorough  
2266 calibration of the bed interaction parameter would require detailed, spatiotemporal  
2267 measurements of grain size distributions in the bed and the saltation cascade. It  
2268 would require a series of sediment traps along the fetch that are regularly emptied  
2269 and sieved as to determine the change of the grain size distribution in the saltation  
2270 cascade in space and over time. Concurrently the grain size distribution at the bed  
2271 surface over the entire fetch needs to be monitored without disturbing the bed sig-  
2272 nificantly. In a laboratory environment the change in grain size distribution could  
2273 be monitored using sediment that is colored per fraction. Visual observation of the  
2274 change in coloring then provides insight in the change in grain size distribution. How-  
2275 ever, the experiment should be performed at such scale that the trapping of sediment  
2276 by upwind traps does not significantly influence the saltation cascade downwind over  
2277 the period that the armor layer develops.

2278 4.6.3 Validation

2279 Validation of the proposed model is ongoing. Initially, validation will be focused on  
2280 gross sediment transport rates in availability-limited systems. Few holistic measure-  
2281 ments are available that monitor both the spatiotemporal variations in the sediment  
2282 transport rate and the availability-limiting factors like moisture content and beach ar-  
2283 moring concurrently (e.g. Delgado-Fernandez et al., 2012; Hoonhout et al., 2013). Sites  
2284 with detailed and frequent topographic measurements and hydrodynamic boundary  
2285 conditions available can be found worldwide. These sites would be a good starting  
2286 point for assessing the performance of the model compared to existing models. Using

2287 simplified, but generic descriptions of the hydraulic mixing and drying rate the model  
2288 should already provide time series of aeolian sediment transport that adhere much  
2289 better to the true nature of aeolian sediment transport events than existing models.  
2290 [Delgado-Fernandez and Davidson-Arnott \(2011\)](#) and [de Vries et al. \(2014a\)](#) already  
2291 indicated that the true nature of these events is not solely related to wind velocity  
2292 and direction, but also to surges, seasons, spring/neap cycles, rain showers and other  
2293 events that influence sediment availability. The variations in aeolian sediment trans-  
2294 port due to these event-driven changes in sediment availability are not well captured  
2295 by models that rely solely on the wind transport capacity. The model has added value  
2296 if it improves the prediction of transport rates under such circumstances.

2297 4.7 CONCLUSIONS

2298 The AEOLIS model presented in this paper is the first aeolian sediment transport  
2299 model that simulates spatiotemporal variations in bed surface properties and sedi-  
2300 ment availability. Simulation of sediment availability is necessary as sediment avail-  
2301 ability cannot be determined a-priori due to its recurrence relation with sediment  
2302 transport. The presented model approach is a generalization of existing modeling  
2303 concepts for aeolian sediment transport that include the influence of bed surface  
2304 properties and limitations in sediment availability, like the shear velocity threshold  
2305 and critical fetch, and is compatible with these concepts. The model uses an ad-  
2306 vvection scheme following [de Vries et al. \(2014b\)](#) and a bed composition module that  
2307 discretizes the bed in horizontal grid cells and vertical bed layers to account for spatial  
2308 variations in bed surface properties. Temporal variations in sediment availability are  
2309 not parameterized, but simulated using the bed composition module. The simulation  
2310 of sediment availability reduces the need for complex spatiotemporal parameteriza-  
2311 tions and consequently calibration. In this paper the influence of sediment sorting  
2312 and beach armoring and the reversed process of hydraulic mixing on aeolian sedi-  
2313 ment transport are illustrated using four prototype cases. The model can reproduce  
2314 patterns in aeolian sediment availability and transport as observed in wind tunnel  
2315 experiments that involve spatiotemporal variations in bed surface properties ([Nick-](#)  
2316 [ling and McKenna Neuman, 1995; Dong et al., 2004b](#)). Further, the model provides a  
2317 generic framework to incorporate additional spatiotemporal varying processes that ei-  
2318 ther influence sediment availability or the wind transport capacity with a minimum of  
2319 parameterization. The framework allows relatively straightforward implementation  
2320 of the effects of infiltration, evaporation, vegetation, buildings, and morphological  
2321 feedback with the wind.

2322 From this paper the following conclusions can be drawn:

- 2323 1. A model for aeolian sediment transport was presented that simulates the pro-  
2324 cesses of sediment sorting and beach armoring, the reversed process of hy-  
2325 draulic mixing, interaction between sediment fractions in the air with sediment  
2326 fractions in the bed and thereby the influence of spatiotemporal variations in  
2327 sediment availability;
- 2328 2. The model can be seen as a generalization of existing approaches to incorporate  
2329 limitations in sediment availability and the wind transport capacity in aeolian

2330 transport estimates and is compatible with approaches based on either shear  
2331 velocity thresholds or critical fetch;

- 2332 3. The process of beach armoring can be a governing factor in aeolian sediment  
2333 transport modeling and may reduce the estimated transport rates significantly  
2334 and up to 95.0% in the presented prototype cases;
- 2335 4. The model can reproduce typical patterns in aeolian sediment transport with  
2336 spatiotemporal variations in sediment availability obtained from measure-  
2337 ments from the unrelated wind tunnel experiments described in [Nickling and](#)  
2338 [McKenna Neuman \(1995\)](#) and [Dong et al. \(2004b\)](#), with a minimum parameteri-  
2339 zation and calibration.

# 5

2340

2341

---

## 2342 SAND MOTOR HINDCAST

---

2343 *This chapter is intended to be published separately and was written accordingly, but has not*  
2344 *been submitted to a particular journal yet.*

2345 **5.1 INTRODUCTION**

2346 In availability-limited coastal systems, the aeolian sediment transport rate is governed  
2347 by the sediment availability rather than the wind transport capacity. Aeolian sediment  
2348 transport models typically incorporate the sediment availability through the shear  
2349 velocity threshold. However, the determination of appropriate threshold values in  
2350 practice appears to be challenging as the shear velocity threshold tends to vary both  
2351 spatially and temporally (Barchyn et al., 2014b). For example, soil moisture in the  
2352 intertidal beach area fluctuates with the tidal phase and causes a local modulation of  
2353 the shear velocity threshold. Moreover, a recurrence relation between sediment avail-  
2354 ability, and thus the shear velocity threshold, and sediment transport exists that com-  
2355 plicates the a-priori determination of an appropriate threshold value. Consequently,  
2356 aeolian sediment transport models tend to perform poorly in availability-limited sys-  
2357 tems.

2358 Sherman et al. (1998) and Sherman and Li (2012) summarized the performance  
2359 of eight aeolian sediment transport models compared to field measurements on a  
2360 sandy beach. Although it is unknown whether this coastal system was availability-  
2361 limited, all models systematically overpredicted the measured aeolian sediment trans-  
2362 port rates. This finding is in correspondence with an abundance of coastal field stud-  
2363 ies in which aeolian sediment transport rates are overestimated by numerical models  
2364 (e.g. Jackson and Cooper, 1999; Lynch et al., 2008; Davidson-Arnott and Bauer, 2009;  
2365 Aagaard, 2014).

2366 In an attempt to explain the poor performance of aeolian sediment transport mod-  
2367 els in coastal environments, many authors emphasized the importance of sediment  
2368 availability and bed surface properties. Typical bed surface properties that are found  
2369 along the coast and known to affect sediment availability are high moisture contents  
2370 (e.g. Wiggs et al., 2004; Davidson-Arnott et al., 2008; Darke and McKenna Neuman,  
2371 2008; McKenna Neuman and Sanderson, 2008; Udo et al., 2008; Bauer et al., 2009; Ed-  
2372 wards and Namikas, 2009; Namikas et al., 2010; Scheidt et al., 2010), salt crusts (e.g.  
2373 Nickling and Ecclestone, 1981), vegetation (e.g. Arens, 1996; Lancaster and Baas, 1998;  
2374 Okin, 2008; Li et al., 2013; Dupont et al., 2014), shell pavements (e.g. van der Wal, 1998;  
2375 McKenna Neuman et al., 2012) and sorted and armored beach surfaces (e.g. Gillette  
2376 and Stockton, 1989; Gillies et al., 2006; Tan et al., 2013; Cheng et al., 2015). The influ-

ence of these bed surface properties on aeolian sediment availability and transport has been investigated and typically resulted in relations between bed surface properties and the shear velocity threshold (e.g. Howard, 1977; Dyer, 1986; Belly, 1964; Johnson, 1965; Hotta et al., 1984; Nickling and Ecclestone, 1981; Arens, 1996; King et al., 2005).

Modeling rather than parameterization of spatiotemporal variations in aeolian sediment availability can improve coastal aeolian sediment transport estimates. As tides only affect the intertidal beach area, lag deposits and salt crusts typically emerge from the dry beach area, and vegetation is often restricted to the dune area, sediment availability varies spatially. In addition, temporal variations in sediment availability are induced by tidal spring/neap cycles, rain showers, storm surges, seasonal variations in vegetation and progressive armoring of the beach. Due to self-grading of the sediment, progressive beach armoring creates a recurrence relation between sediment availability and transport that challenges the a-priori determination of the spatiotemporal variations in sediment availability. Process-based modeling of the instantaneous shear velocity threshold field can address these challenges and improve coastal aeolian sediment transport estimates.

This paper presents the first application of a two-dimensional (2DH) aeolian sediment availability and transport model (Hoonhout and de Vries, 2016d) to hindcast the development of the sub-aerial topography of an availability-limited coastal system. The model is unique in that it describes both spatial and temporal variations in aeolian sediment availability induced by the combined influence of sediment sorting, beach armoring and soil moisture content. The influence of spatiotemporal variations in aeolian sediment availability and the model performance are illustrated by a comparison between model results and a large scale sediment budgets analysis that identifies and quantifies the main sources and sinks for aeolian sediment in the coastal system (Hoonhout and de Vries, 2016a).

## 5.2 FIELD SITE

The Sand Motor (or Sand Engine) is an artificial  $21 \text{ Mm}^3$  sandy peninsula protruding into the North Sea off the Delfland coast in The Netherlands (Figure 5.1, Stive et al., 2013). The Sand Motor was constructed in 2011 and its bulged shoreline initially extended about 1 km seaward and stretched over approximately 2 km along the original coastline. The original coast was characterized by an alongshore uniform profile with a vegetated dune with an average height of 13 m and a linear beach with a 1:40 slope. The dune foot is located at a height of approximately 5 m+MSL.

Due to natural sediment dynamics the Sand Motor distributes about  $1 \text{ Mm}^3$  of sand per year to the adjacent coasts (Figure 5.1). The majority of this sand volume is transported by tides and waves. However, the Sand Motor is constructed up to 5 m+MSL and locally up to 7 m+MSL, which is in either case well above the maximum surge level of 3 m+MSL (Figure 5.2c). Therefore, the majority of the Sand Motor area is uniquely shaped by wind.

The Sand Motor comprises both a dune lake and a lagoon that act as large traps for aeolian sediment (Figure 5.1). The lagoon is affected by tidal forcing, although the tidal amplitude quickly diminished over time as the entry channel elongated. The tidal range of about 2 m that is present at the Sand Motor periphery (Figure 5.2c), is nowadays damped to less than 20 cm inside the lagoon (de Vries et al., 2015). Con-

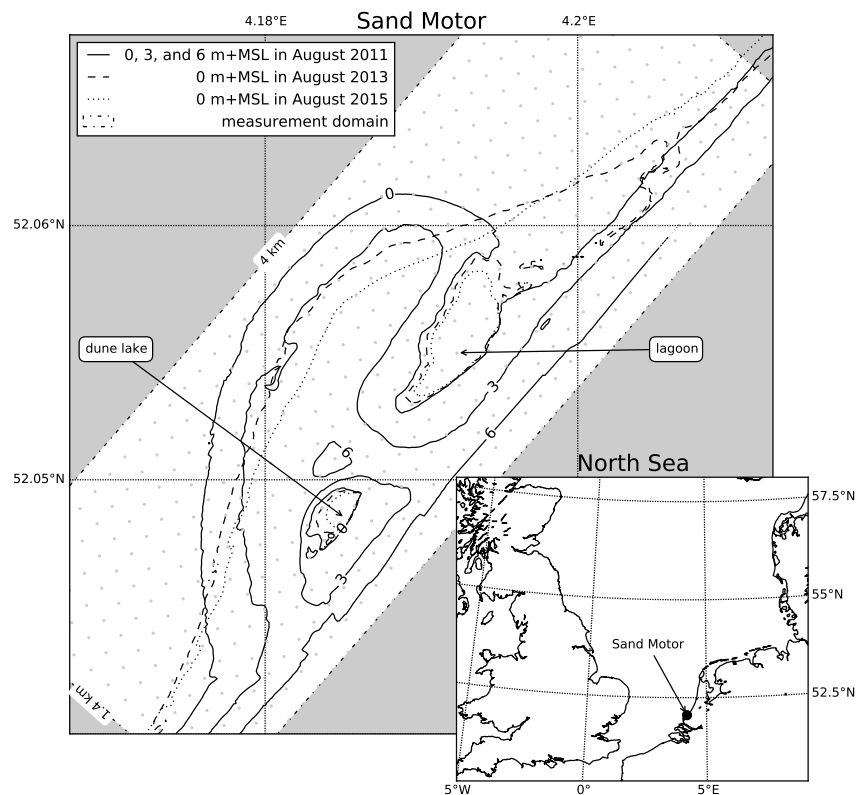


Figure 5.1: Location, orientation, appearance and evolution of the Sand Motor between construction in 2011 and 2015. The box indicates the measurement domain used in the remainder of this paper. A 100 x 100 m grid aligned with the measurement domain is plotted in gray as reference.

2422 subsequently, the tidal currents at the closed end of the lagoon, where most aeolian  
 2423 sediment is trapped, are negligible.

2424 The dominant wind direction at the Sand Motor is south to southwest (Figure 5.2a).  
 2425 However, during storm conditions the wind direction tends to be southwest to northwest.  
 2426 During extreme storm conditions the wind direction tends to be northwest.  
 2427 Northwesterly storms are typically accompanied by significant surges as the fetch is  
 2428 virtually unbounded to the northwest, while surges from the southwest are limited  
 2429 due to the presence of the narrowing of the North Sea at the Strait of Dover (Figure  
 2430 5.1, inset).

2431 5.3 MODEL APPROACH

2432 A two-dimensional (2DH) model of the Sand Motor that includes limitations in sediment  
 2433 availability is constructed and calibrated based on four years of field measurements  
 2434 on wind, tides, waves and topography. The calibrated model is used to investigate  
 2435 the influence of spatiotemporal variations in aeolian sediment availability on  
 2436 sediment accumulation in the Sand Motor domain.

2437 To test that the Sand Motor mega nourishment is indeed an availability-limited  
 2438 coastal system, the measured long-term sediment accumulation volumes (Hoonhout  
 2439 and de Vries, 2016a) are first compared to a reference model that assumes no limitations  
 2440 in sediment availability exist.

2441 5.3.1 Reference model

2442 A selection of equilibrium sediment transport formulations is used as reference model.  
 2443 An equilibrium sediment transport formulation describes the wind transport capacity  
 2444 in given conditions. In conjunction with a shear velocity threshold based on only a  
 2445 constant uniform median grain size, an estimate of the potential aeolian sediment  
 2446 accumulation in absence of availability-limitations can be obtained. The potential  
 2447 aeolian sediment accumulation or cumulative wind transport capacity  $Q$  [ $m^3$ ] in the  
 2448 Sand Motor domain is estimated based on hourly averaged time series of the wind  
 2449 speed  $u_z$  [ $m/s$ ] and direction  $\theta_u$  [ $^\circ$ ] obtained from the KNMI meteorological station  
 2450 in Hoek van Holland following:

$$Q = \sum q \cdot \frac{\Delta t \cdot \Delta y}{(1-p) \cdot \rho_p} \cdot f_{\theta_u} \quad (5.1)$$

2451 where the temporal resolution  $\Delta t = 1$  h, the alongshore span of the domain  $\Delta y = 4$   
 2452 km, the porosity  $p = 0.4$ , the particle density  $\rho_p = 2650 \text{ kg/m}^3$ , the sediment transport  
 2453 rate  $q$  is given by the equilibrium sediment transport formulation (Table 5.1) and  $f_{\theta_u}$   
 2454 is a factor to account for the wind direction. The wind direction can be accounted for  
 2455 by only including the onshore wind component with respect to the original coastline  
 2456 orientation. However, given the typical Sand Motor geometry (Figure 5.1), sediment  
 2457 is likely to be trapped in the dune lake and lagoon even with alongshore wind. There-  
 2458 fore it can be assumed that the onshore wind component will provide a lower limit of  
 2459 the cumulative wind transport capacity. Similarly, an upper limit can be obtained by  
 2460 assuming that all onshore wind directions contribute equally to the cumulative wind  
 2461 transport capacity. For the upper limit the factor  $f_{\theta_u}$  is defined as:

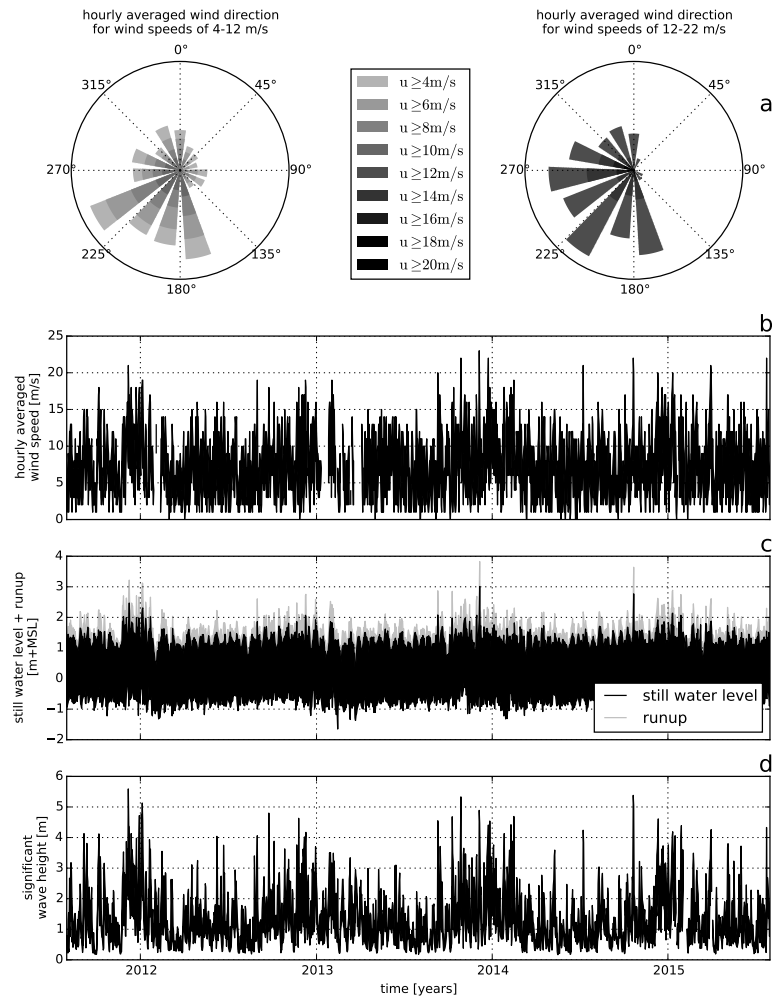


Figure 5.2: Wind and hydrodynamic time series from 2011 to 2015. Hourly averaged wind speeds and directions are obtained from the KNMI meteorological station in Hoek van Holland (upper panels). Offshore still water levels, wave heights and wave periods are obtained from the Europlatform (lower panels). Runup levels are estimated following Stockdon et al. (2006).

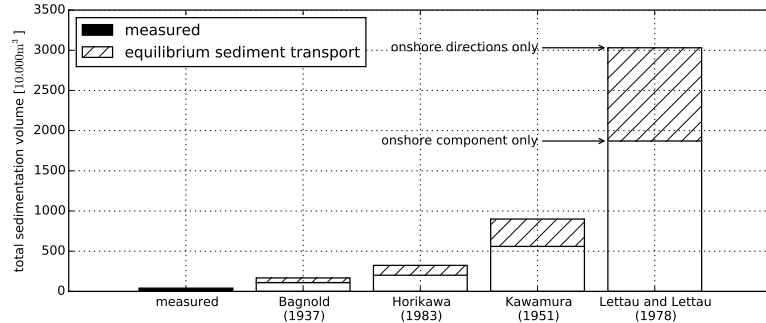


Figure 5.3: Comparison of the cumulative wind transport capacity according to a selection of equilibrium sediment transport formulations and measured total sedimentation in the Sand Motor domain. The equilibrium sediment transport is based on an hourly averaged wind speed and direction time series from September 1, 2011 until September 1, 2015. Offshore wind directions are discarded. For the upper boundary of each estimate all wind directions are weighted equally. For the lower boundary of each estimate the wind directions are weighted according to the magnitude of the onshore component.

$$f_{\theta_u} = \begin{cases} 1 & \text{if } \cos(312^\circ - \theta_u) \geq 0 \\ 0 & \text{if } \cos(312^\circ - \theta_u) < 0 \end{cases} \quad (5.2)$$

while for the lower limit the factor  $f_{\theta_u}$  is defined as:

$$f_{\theta_u} = \max(0 ; \cos(312^\circ - \theta_u)) \quad (5.3)$$

where  $312^\circ$  accounts for orientation of the original coastline. Figure 5.3 presents an overview of the cumulative wind transport capacity in the Sand Motor domain over the period between September 1, 2011 and September 1, 2015 according to a selection of equilibrium sediment transport formulations and in comparison with the measured accumulation volumes. The estimates of the wind transport capacity show a large variation between formulations that are mainly due to the incorporation of the shear velocity threshold. However, all formulations overestimate the measured sediment accumulation in the Sand Motor domain with at least a factor 3 – 4. The large variation and consistent overestimation is in accordance with the review of aeolian sediment transport models presented by Sherman and Li (2012). The consistent overestimation of the measured sedimentation volumes in the Sand Motor domain suggest that the Sand Motor is indeed an availability-limited coastal system.

### 5.3.2 Schematization

A two-dimensional (2DH) aeolian sediment availability and transport model for the Sand Motor mega nourishment is constructed for the four years between September

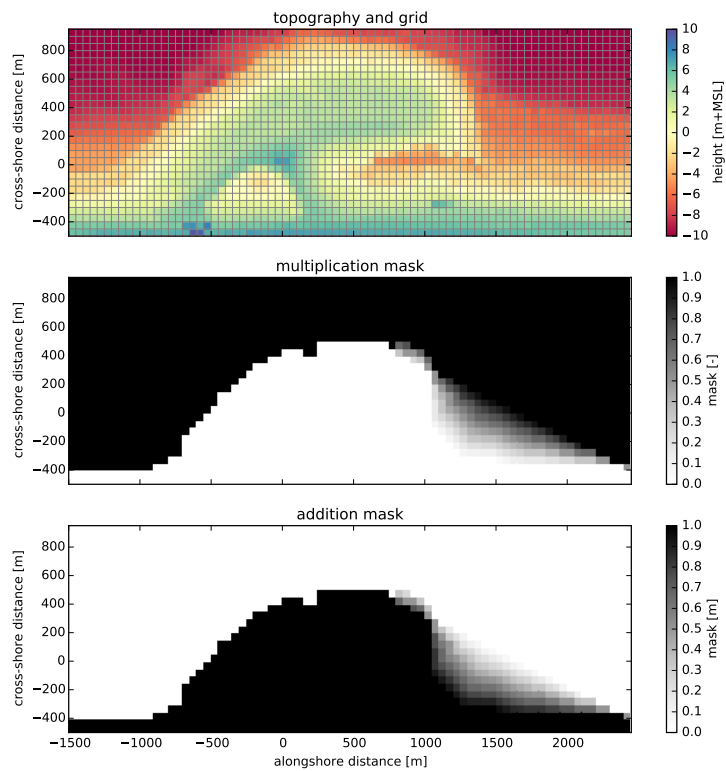


Figure 5.4: Model grid and topography based on the topographic survey of August 3, 2011 (upper panel) and hydrodynamic mask used to limit tidal and wave motions in the dune lake and lagoon (middle and lower panels). Water levels and wave heights are uniformly imposed to the model and multiplied by the multiplication mask and subsequently increased with the addition mask.

Table 5.1: Equilibrium sediment transport formulations, coefficient values\* and the ratio between measurements and model results.

Reference	Equation	C	Ratio
Bagnold (1937b)	$q = C \frac{\rho_a}{g} \sqrt{\frac{d_n}{D_n}} (u_* - u_{*th})^3$	1.8	3 – 4
Horikawa et al. (1983)	$q = C \frac{\rho_a}{g} (u_* + u_{*th})^2 (u_* - u_{*th})$	1.0	5 – 8
Kawamura (1951)	$q = C \frac{\rho_a}{g} (u_* - u_{*th})^2 (u_* - u_{*th})$	2.78	14 – 22
Lettau and Lettau (1978)	$q = C \frac{\rho_a}{g} \sqrt{\frac{d_n}{D_n}} (u_* - u_{*th}) u_*^2$	6.7	46 – 75

\* Other values are the shear velocity  $u_* = \alpha \cdot u_z$  m/s, the shear velocity threshold  $u_{*th} = \alpha \cdot 3.87$  m/s, the conversion factor from free-flow wind velocity to shear velocity  $\alpha = 0.058$ , the air density  $\rho_a = 1.25$  kg/m<sup>3</sup>, the particle density  $\rho_p = 2650.0$  kg/m<sup>3</sup>, the gravitational constant  $g = 9.81$  m/s<sup>2</sup>, the nominal grain size  $d_n = 335$  µm, a reference grain size  $D_n = 250$  µm and the height above the bed of the wind measurement  $z = 10$  m.

2478 1, 2011 and September 1, 2015, which is shortly after the nourishment was placed.  
2479 The model's topography and grid are based on the measured topographies of August  
2480 3, 2011 and later. The topographies are rotated 48° and interpolated to a 50 × 50 m  
2481 grid spanning 1.5 km cross-shore and 4 km alongshore with respect to the original  
2482 coastline, not including the dunes (Figure 5.4, upper panel).

2483 Four years of hourly wind speed and direction data measured at 10 m above the bed  
2484 is obtained from the KNMI meteorological station at Hoek van Holland (Figure 5.2a,b).  
2485 Hourly offshore water levels and wave heights are obtained from the Europlatform  
2486 for the same period (Figure 5.2c,d).

2487 An average lognormal grain size distribution with a median diameter  $d_{50} = 335$  µm  
2488 is used as measured at the Sand Motor field site. The sand fractions cover a range  
2489 from 0.1 to 2 mm. The amount of shells and other roughness elements in the origi-  
2490 nally nourished sand is estimated to be 5%. The estimate is based on three sediment  
2491 samples obtained from the field site 0.5 m below the bed surface. Additional fractions  
2492 ranging from 2 to 32 mm are added according to a lognormal distribution to account  
2493 for the presence of roughness elements in the bed. The grain size distribution is used  
2494 to populate the initial bed that consists of 10 bed composition layers with a thickness  
2495 of 1 cm each.

2496 The hindcast aims at the large scale and long term sedimentation volumes as pre-  
2497 sented by Hoonhout et al. (2016a). Therefore an efficient, but diffusive, implicit Euler  
2498 Backward scheme with a timestep of 1 h is used that does not resolve high frequency  
2499 variations in wind or sediment transport. Consequently, the model produces smooth  
2500 solutions that describe hourly steady states based on the instantaneous average wind  
2501 speed and sediment availability.

2502 Bagnold (1937b) is selected as equilibrium sediment transport formulation as it is  
2503 derived separately for different grain sizes and therefore suitable for multi-fraction  
2504 aeolian sediment transport. Alternative formulations (Table 5.1) are derived for wider  
2505 grain size distributions that do not necessarily result in a monotonic relation between  
2506 the grain size and the sediment transport rate (e.g. Kawamura, 1951; Horikawa et al.,  
2507 1983). Such non-monotonic relation is unrealistic in a multi-fraction context as it  
2508 would result in a preference to transport both fine sediment and large elements that  
2509 are considered non-erodible. Moreover, the formulation of Bagnold (1937b) overesti-

2510 mates the measured aeolian sediment transport rates in the Sand Motor domain less  
 2511 compared to alternative formulations (Table 5.1, rightmost column).

2512 Water levels and wave heights are initially uniformly imposed to the model. Con-  
 2513 sequently, the tidal range, mean water level and wave heights that are present at the  
 2514 Sand Motor periphery are also present in the dune lake and lagoon. In reality the  
 2515 tidal range and wave heights in the dune lake and lagoon are much lower, while the  
 2516 mean water level in the dune lake and lagoon is elevated compared to mean sea level  
 2517 (de Vries et al., 2015). To account for these spatial differences in hydrodynamics a  
 2518 hydrodynamic mask is applied (Figure 5.4, middle and lower panel; Appendix B.3.4)

2519 Subtidal changes in topography are not simulated by the model. The subtidal  
 2520 changes can be important to aeolian sediment transport as the location and size of  
 2521 aeolian sediment erosion and deposition areas might change. To account for these  
 2522 changes, measured topographies are imposed to the model through a Basic Model  
 2523 Interface (BMI, Peckham et al., 2013, Appendix B.4).

2524 All measured topographies in the period between September 1, 2011 and Septem-  
 2525 ber 1, 2015 are linearly interpolated in time as to obtain daily updates of the Sand  
 2526 Motor’s topography. The hydrodynamic mask is updated along with the topography.  
 2527 The presented aeolian sediment transport rates are based on the time-integrated en-  
 2528 trainment and deposition rates that are computed by the model rather than differences  
 2529 in topography.

### 2530 5.3.3 Calibration

2531 The model is calibrated on the shape of roughness elements that emerge from the bed  
 2532 and shelter the sand surface from wind erosion, the drying rate of the soil and the  
 2533 time needed for the sediment transport to adapt to changing wind conditions. These  
 2534 processes are represented in the model by parameters for which data or literature can  
 2535 only provide approximate values:

- 2536 1.  $\sigma$ , as used in the formulation of Raupach et al. (1993, Equation 4.2), is the ratio  
 2537 between the basal and frontal area of the roughness elements that constitute the  
 2538 beach armor layer.
- 2539 2.  $T_{dry}$  is the time scale at which the beach dries out after flooding (Equation B.26).  
 2540 It represents the time in which the soil moisture content halves in case the beach  
 2541 is not inundated and no evaporation occurs.
- 2542 3.  $T$  is the adaptation time scale in the right-hand side of the advection equation  
 2543 (Equation 4.7). It represents the time scale to which the sediment transport  
 2544 adapts to variations in the wind conditions and sediment availability.

2545 The implementation of roughness elements is characterized by three calibration pa-  
 2546 rameters:  $m$ ,  $\beta$  and  $\sigma$  (Equation 4.13).  $m$  is a factor to account for the difference  
 2547 between the mean and maximum shear stress and is usually chosen as 0.5 for field  
 2548 applications (Raupach et al., 1993; McKenna Neuman et al., 2012). Numerically it is  
 2549 irrelevant if  $\beta$  or  $\sigma$  is calibrated as they only appear as a ratio  $\frac{\beta}{\sigma}$  in the model imple-  
 2550 mentation. As  $\beta$  is the ratio between the drag coefficient of the roughness elements  
 2551 alone and the drag coefficient of the unarmored sandy bed, the value can be assumed

2552 to be reasonably generic. In contrast,  $\sigma$  depends on the shape and protrusion of the  
 2553 roughness elements and therefore depends on the field site and varies in time. For  
 2554 example, a spherical object placed on top of the bed would be represented by  $\sigma = 1$ ,  
 2555 while a spherical object protruding halfway through the bed (hemisphere) would be  
 2556 represented by  $\sigma = 2$ . Consequently, calibration of  $\sigma$  seems to be preferable as it is  
 2557 less certain. Wind tunnel experiments presented by McKenna Neuman et al. (2012)  
 2558 investigated the influence of a lag deposits, consisting of shells and shell fragments,  
 2559 on aeolian sediment transport. Values for the calibration coefficients  $m$  and  $\beta$  were  
 2560 found to be 0.5 and 130 respectively and are adopted for the Sand Motor hindcast. An  
 2561 optimal average value for  $\sigma$  is obtained by systematic variation between 2 and 20.

2562 The drying rate of the beach ( $T_{dry}$ ) depends on many factors, like grain size, soil  
 2563 moisture content, groundwater level, wind speed and solar radiation. The use of  
 2564 a single time scale as aggregate for these processes is an oversimplification of reality.  
 2565 Therefore a wide range of parameter values is covered in the calibration.  $T_{dry}$  is varied  
 2566 between 0.1 and 10 hours where the former results in virtually instant drying and the  
 2567 latter results in an intertidal beach that is permanently too moist for aeolian sediment  
 2568 transport to be initiated.

2569 The adaptation time scale ( $T$ ), that represents the swiftness of aeolian sediment  
 2570 transport to adapt to changing wind conditions, is in the order of seconds (Davidson-  
 2571 Arnott et al., 2008; de Vries et al., 2014b). As the model time step is orders of mag-  
 2572 nitude larger, the model effectively solves steady states and the value for  $T$  will not  
 2573 affect temporal variations in sediment transport. However, the adaptation time scale  
 2574 also affects the development of the saltation cascade in space. Sediment transport  
 2575 increases in downwind direction from a zero-flux boundary, like the water line in  
 2576 case of onshore wind, with a rate that is governed by the value of  $T$ . Consequently,  $T$   
 2577 influences the width of the source area in case of abundant sediment availability.  $T$  is  
 2578 varied between 1 and 10 seconds.

2579 The calibration is performed based on the bi-monthly erosion and deposition vol-  
 2580 umes as measured in the Sand Motor domain (Hoonhout and de Vries, 2016a). The  
 2581 erosion and deposition volumes are determined within seven predefined zones (Fig-  
 2582 ure 5.5) that aim to separate areas with marine influences from areas without marine  
 2583 influences, and separate areas with net aeolian erosion from areas with net aeolian de-  
 2584 position. The zonation is based on the 0, 3 and 5 m+MSL contour lines that roughly  
 2585 correspond with the mean water level, maximum runup level or berm edge and the  
 2586 dune foot respectively. The average  $R^2$  value of the time series for erosion and deposi-  
 2587 tion is used as benchmark. The  $R^2$  value represents the fraction of explained variance  
 2588 and is defined as:

$$R^2 = \frac{\sum_n [V_{\text{measured}}^n - \bar{V}_{\text{measured}}^n]^2}{\sum_n [V_{\text{measured}}^n - \bar{V}_{\text{measured}}^n]^2} \quad (5.4)$$

2589 where  $V^n$  is the measured or modeled sediment volume in time period  $n$ . The overbar  
 2590 denotes time-averaging. In addition the root-mean-square error (RMSE) is presented  
 2591 as absolute measure for the model accuracy, which is defined as:

$$\text{RMSE} = \sqrt{\sum_n [V_{\text{measured}}^n - V_{\text{model}}^n]^2} \quad (5.5)$$

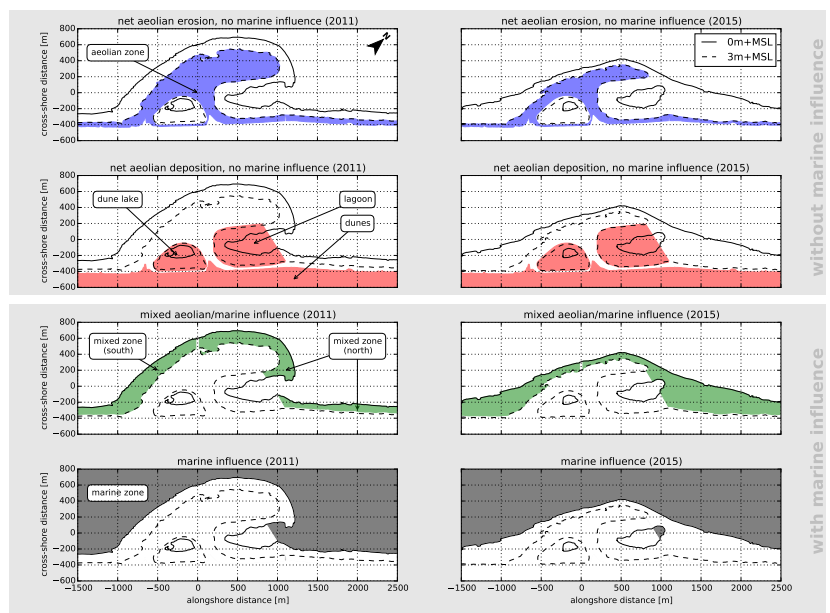


Figure 5.5: Zonation of the Sand Motor domain into zones with net aeolian erosion and no marine influence, net aeolian deposition and no marine influence, mixed aeolian/marine influence and marine influence. Zonation is based on the 0, 3 and 5 m+MSL contour lines that roughly correspond with the mean water level, maximum runup level or berm edge and the dune foot respectively. Left panels: 2011. Right panels: 2015. Source: [Hoonhout and de Vries \(2016a\)](#).

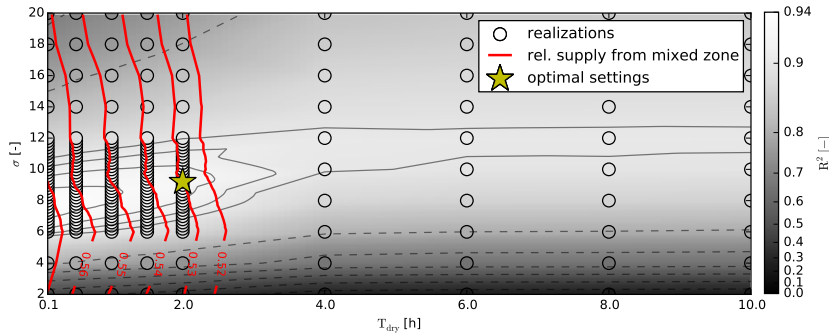


Figure 5.6: Systematic variation of calibration parameters  $\sigma$  and  $T_{\text{dry}}$  with  $T = 1$  s. The circles indicate the realizations made. The colored background depicts a linear interpolation of the  $R^2$  values with respect to the data presented in Figure 2.6. The solid isolines depict  $R^2$  values from 0.90 to 0.93, while the dashed isolines depict  $R^2$  values from 0.0 to 0.9. The red lines depict the relative supply from the mixed zones ranging from 52% to 57%. The yellow star indicates the optimal value model settings.

2592 The calibration itself is performed in three steps:

- 2593 1. A coarse calibration on  $\sigma$  and  $T_{\text{dry}}$ .  
 2594 2. A calibration on  $T$  using the provisional optimal settings for  $\sigma$  and  $T_{\text{dry}}$ .  
 2595 3. A fine calibration on  $\sigma$  and  $T_{\text{dry}}$  using the optimal setting for  $T$ .

2596 5.4 RESULTS

2597 The optimal model settings were chosen from 150 realizations (Figure 5.6). The opti-  
 2598 mal realization has an  $R^2$  value of 0.92 and a RMSE of  $3 \cdot 10^4$  m<sup>3</sup>. The corresponding  
 2599 optimal parameter settings are found to be  $\sigma = 9.2$ ,  $T_{\text{dry}} = 2$  h and  $T = 1$  s. These  
 2600 settings were ultimately selected from a cluster of realizations with comparable  $R^2$   
 2601 values based on the relative sediment supply from the mixed zones (Figure 5.5, third  
 2602 row) at the end of the simulation. An overview of all model settings for the calibrated  
 2603 model is given in Appendix C.

2604 Figure 5.7 shows that erosion from the aeolian zone (Figure 5.5, first row) is most  
 2605 pronounced in the first year and least in the second year in both the measurements  
 2606 and the model results. Also the deposition of aeolian sediment in the dune lake and  
 2607 lagoon (Figure 5.5, second row) is observed in both the measurements and model  
 2608 results, although the model underestimates these deposited volumes. The deposition  
 2609 in the dune lake and lagoon is also more localized in the measurements than in the  
 2610 model results. The spatial variability in the erosion of the aeolian zone is larger in the  
 2611 measurements than in the model results. The large variability measured in the mixed  
 2612 zone is not present in the model results as hydrodynamic sediment transport is not  
 2613 simulated.

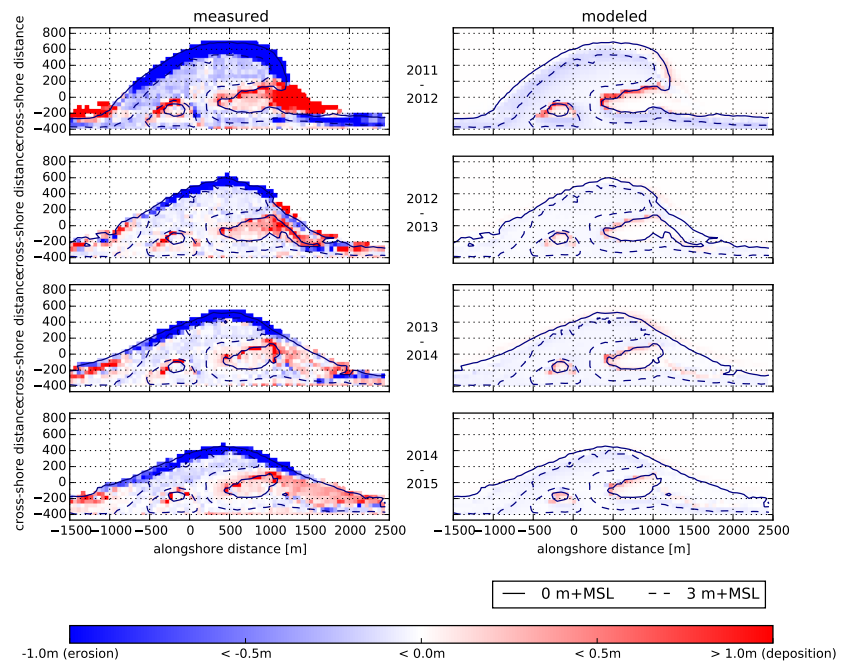


Figure 5.7: Measured and modeled yearly sedimentation and erosion above 0 m+MSL. Model results only include aeolian sediment transport as hydrodynamic sediment transport is not computed. Comparisons are made between the September surveys of each year.

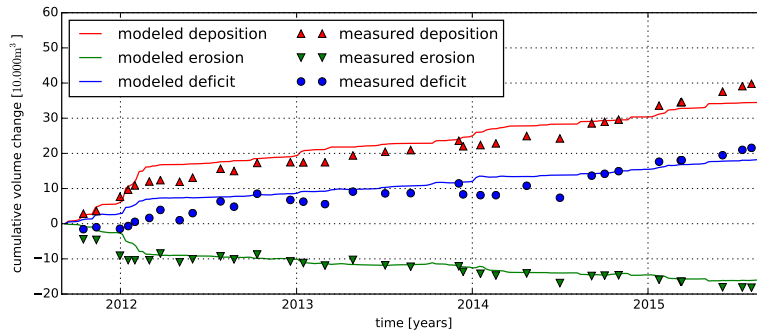


Figure 5.8: Measured and simulated net volume change of erosion and deposition volumes as presented in Figure 2.6.

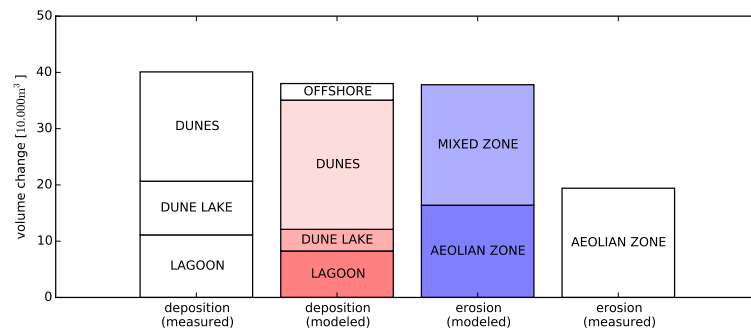


Figure 5.9: Total erosion and deposition volumes at the end of the simulation and measured total erosion and deposition volumes as presented in Figure 2.5.

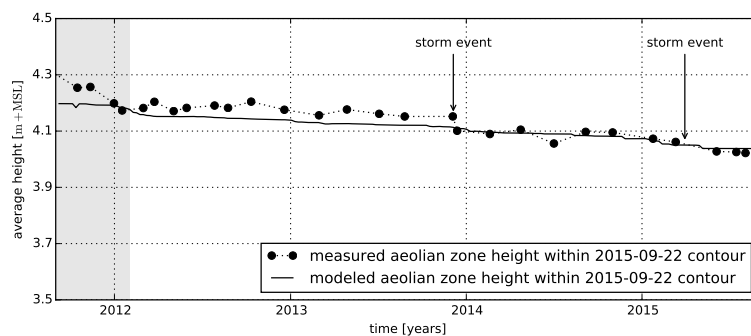


Figure 5.10: Measured and simulated average beach height in the aeolian zone as presented in Figure 2.8.

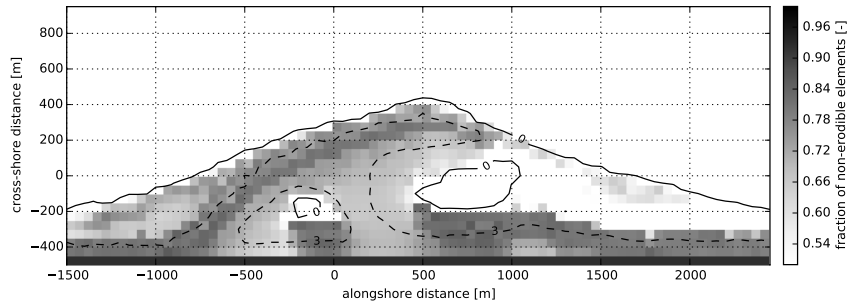


Figure 5.11: Simulated shell fraction in the aeolian zone at the end of the simulation.

2614 The development of the total erosion and deposition volumes in the Sand Motor  
 2615 domain in the four year period is represented well by the model (Figure 5.8). The  
 2616 dune accumulation volume is overestimated at the expense of the sediment volumes  
 2617 deposited in the dune lake and lagoon (Figure 5.9). As the dune area is not included in  
 2618 the model domain, the sediment flux over the onshore boundary is assumed to settle  
 2619 in the dunes entirely. The total sediment accumulation at the end of the simulation is  
 2620 underestimated by 12% as the offshore sediment deposits are not included in the large  
 2621 scale sediment budget analysis that are used for comparison. The underestimation is  
 2622 unique for the last nine months of the simulation as the model overestimates the total  
 2623 sediment accumulation with 5% on average (Figure 5.8). The relative importance of  
 2624 the mixed zone as supplier of aeolian sediment is well captured.

2625 The change in beach height within the most recent 3 m+MSL contour, that marks  
 2626 the aeolian zone, is represented by the model as the R<sup>2</sup> value is 0.71 and the RMSE  
 2627 is about 4 cm or 12% of the average bed level change (Figure 5.10). As the change in  
 2628 beach height is computed within the most recent 3 m+MSL contour, the discrepancy is  
 2629 illustrative for the differences in spatial variability in erosion between measurements  
 2630 and model results. The lowering of the beach in the aeolian zone in the first half year  
 2631 of the simulation is particularly underestimated, while the accelerated erosion in this  
 2632 period is well captured in the total sediment transport. This indicates that sediment  
 2633 is eroded from outside the most recent 3 m+MSL contour.

2634 The coverage of non-erodible elements  $\sigma\lambda$  [-] (Equation 4.14) in the aeolian zone  
 2635 varies between 60% and 80% at the end of the simulation (Figure 5.11). The coverage  
 2636 is high compared to the 10% – 20% shell coverage estimated to be present at the Sand  
 2637 Motor above 3 m+MSL based on gridded photographs.

2638 Both the spatial and temporal variations in aeolian sediment availability are crucial  
 2639 for an accurate description of total sedimentation and erosion volumes as well as an  
 2640 accurate prediction of the aeolian sediment source and deposition areas. Figure 5.12  
 2641 compares the total sedimentation volume according to measurements, the calibrated  
 2642 model and additional simulations, that are variations of the calibrated model in which  
 2643 spatial and/or temporal variations in the shear velocity threshold are averaged out.  
 2644 During these additional simulations the shear velocity threshold is not computed by  
 2645 the model, but space- and/or time-averaged thresholds based on the model results

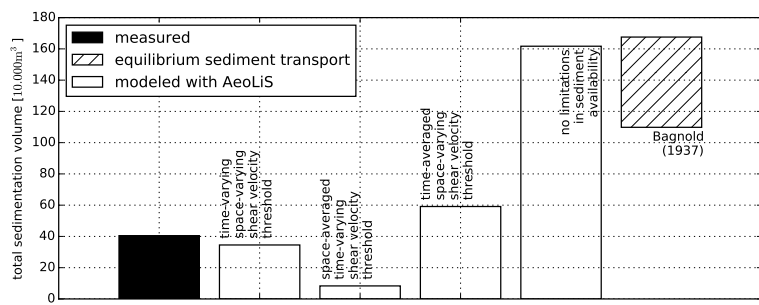


Figure 5.12: The influence of time-varying and space-varying shear velocity thresholds on the total sedimentation volume. The two leftmost bars depict the measured and modeled sedimentation volume as obtained from the calibrated model (Figure 5.9). The middle two bars depict results from two separate model simulations in which a space-averaged threshold time series or a time-averaged threshold field is imposed respectively. The threshold averages are based on the result from the calibrated model. The two rightmost columns depict a result from a separate model simulation with a constant uniform threshold based on only a constant uniform median grain size and the estimated equilibrium sediment transport following [Bagnold \(1937b\)](#) respectively (Table 5.1).

2646 of the calibrated model are imposed. Negligence of the spatial variations results in  
2647 a 79% underestimation of the total sedimentation volume and a relative contribution  
2648 of 8% of the mixed zones. The negligence of the temporal variations results in a 46%  
2649 overestimation of the total sedimentation volume and a relative contribution of 86%  
2650 of the mixed zones. In addition, a simulation without limitations in sediment avail-  
2651 ability overestimates the measured total sedimentation volumes with 400%, which is  
2652 comparable to the wind transport capacity following [Bagnold \(1937b, Figure 5.3\)](#).

2653 **5.5 DISCUSSION**

2654 The model results show that multi-annual aeolian sediment erosion and deposition  
2655 volumes, and the relative importance of the mixed zones as source of aeolian sedi-  
2656 ment are reproduced with reasonable accuracy. This suggests that indeed significant  
2657 limitations in sediment availability, due to soil moisture content and beach armoring,  
2658 govern aeolian sediment transport in the Sand Motor domain. A comparison with a  
2659 simulation without limitation in sediment availability suggests that aeolian sediment  
2660 availability in the Sand Motor domain is limited to about 25% – 35% of the wind  
2661 transport capacity.

2662 The negligence of spatial variations causes the model to underestimate the mea-  
2663 sured total sedimentation volume. The sediment supply from the relatively small  
2664 mixed zone is marginalized as the imposed space-averaged shear velocity threshold  
2665 is relatively high. In contrast, the negligence of temporal variations causes the model  
2666 to overestimate the measured total sedimentation volume. The sediment supply from  
2667 the mixed zones is increased as the effect of its periodic flooding is averaged out. At  
2668 the same time, the sediment supply from the aeolian zone is decreased as the influ-  
2669 ence of beach armoring affects sediment availability from the start of the simulation  
2670 rather than after the development of the beach armor layer. Therefore, the total sed-  
2671 imentation volume is not only overestimated, but also the importance of the mixed  
2672 zones as supplier of aeolian sediment.

2673 **5.5.1 Seasonal and local variations in sedimentation and erosion**

2674 The model can reproduce multi-annual trends in sedimentation volume, which is the  
2675 aim of the hindcast, but seasonal and local variations are sometimes not represented  
2676 by the model. An analysis of these variations is interesting as they influence the  
2677 accuracy of specific model results.

2678 Average wind speeds tend to be elevated in December and January (Figure 5.2),  
2679 which leads to short periods of accelerated sediment accumulation in the beginning  
2680 of 2012, 2013 and 2015 that are captured well by the model. Early 2014 no accelerated  
2681 sediment accumulation is measured, while the model simulation shows an increase  
2682 in sediment accumulation originating from the mixed zones similar to other years.

2683 The discrepancy early 2014 might be explained by topographic changes induced  
2684 by hydrodynamic forces. On December 5th, 2013 an exceptional storm hit the Dutch  
2685 coast. During this storm a significant decrease in aeolian deposits in the lagoon was  
2686 observed, while deposits in the dunes and dune lake increased only marginally. The  
2687 assumption that the closed end of the lagoon is mainly governed by aeolian sediment  
2688 transport might be violated in these exceptional conditions. At the same time, the

2689 erosion of the aeolian zone that day equaled the total erosion of the aeolian zone  
2690 that year. Consequently, the total subaerial sediment volume decreased that day with  
2691 about  $1 \cdot 10^4 \text{ m}^3$ , possibly caused by hydrodynamic forces. This suggests that the sim-  
2692 plified hydrodynamics, despite the use of a hydrodynamic mask, are a limiting factor  
2693 in describing the Sand Motor's subaerial morphodynamics during extreme storms.

2694 In the first months of the simulation, the total sediment accumulation is well repre-  
2695 sented, but erosion of the aeolian zone is underestimated. As beach armoring is the  
2696 most important availability limitation in the aeolian zone, this suggests that the ar-  
2697 moring rate is overestimated by the model. The armoring rate is mainly influenced by  
2698 initial shell fraction of 5%, which might be overestimated. Alternatively, the initially  
2699 uniform distribution of shells in the bed is not an accurate representation of reality.

2700 Measured erosion and deposition rates exceed modeled erosion and deposition  
2701 rates in the final nine months of the simulation. In this period dune growth seems to  
2702 accelerate, while neither the deposition in the dune lake and lagoon did accelerate nor  
2703 did the wind speed increase. The apparent acceleration is therefore solely found in  
2704 the half yearly lidar measurements of the dune area (Hoonhout and de Vries, 2016a)  
2705 and is consequently based on a single data point. Despite the uncertainty involved in  
2706 the measured acceleration, also precipitation rates, that were up to 70% lower in this  
2707 period compared to the same period in other years, might explain the discrepancy  
2708 at the end of the simulation (Jackson and Nordstrom, 1998). For the hindcast no  
2709 precipitation time series are imposed as the effect on the aeolian sediment transport  
2710 rate is not properly understood yet. Consequently, the calibration of the model might  
2711 have resulted in an overestimated importance of beach armoring to compensate for  
2712 the negligence of precipitation.

2713 The distribution of the aeolian sediment deposits over the dune lake, lagoon and  
2714 dunes is not represented well as deposits in the dune lake and lagoon are underes-  
2715 timated. Additional hydrodynamic and hydrologic processes, like wind setup and  
2716 groundwater seepage, might cause the entrapment area in reality to be larger than  
2717 modeled. But more importantly, the dune lake and lagoon are positioned in the lee  
2718 of the Sand Motor crest with respect to the predominant southwesterly wind direc-  
2719 tion. The height difference between the Sand Motor crest and the water level in the  
2720 lagoon and dune lake is several meters, which is likely to influence the local wind  
2721 field significantly. The probable decrease in wind shear in the lee of the Sand Mo-  
2722 tor crest promotes deposition of aeolian sediment and likely hampers supply to the  
2723 dunes. These local variations in wind shear are not included in the simulations.

### 2724 5.5.2 Beach armoring, sediment availability and the shear velocity threshold

2725 The influence of beach armoring is reflected in the model by both  $\sigma$  and the rough-  
2726 ness density  $\lambda$  (Equation 4.13 and 4.14). The optimal value for  $\sigma$  was found to be 9.2,  
2727 which is high compared to the value of 4.2 found by McKenna Neuman et al. (2012).  
2728 The difference suggests that the roughness elements at the Sand Motor protrude less  
2729 from the bed compared to what was found in the wind tunnel experiments. Conse-  
2730 quently, the importance of beach armoring would be relatively low at the Sand Motor.  
2731 However, the low  $\sigma$  value is largely compensated by the roughness density  $\lambda$  reflected  
2732 in a shell coverage  $\sigma\lambda$  that is high compared to what was found in the wind tunnel  
2733 experiments (12% – 43% on average) and what is found at the Sand Motor field site

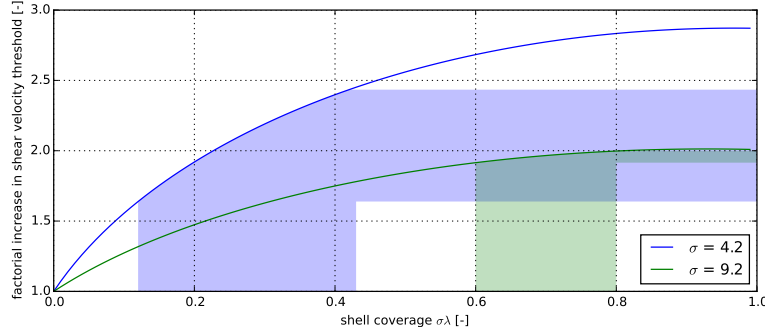


Figure 5.13: Relation between shear velocity threshold, shell coverage and  $\sigma$  according to Raupach et al. (1993, Equation 4.13). The shaded areas indicate the relevant parameter ranges from McKenna Neuman et al. (2012) (blue) and the model results (green).

(10% – 20%). Figure 5.13 shows that the combination of high shell coverage and  $\sigma$  value results in a very similar increase of the shear velocity threshold compared to the wind tunnel experiments presented by McKenna Neuman et al. (2012).

The reason that the model calibration resulted in this particular value for  $\sigma$  is that the model does not differentiate between the fluid and impact velocity threshold. Therefore, the roughness elements in the model affect the initiation of sediment transport equal to the continuation of sediment transport. The potential reduction in sediment availability increases with a decreasing value for  $\sigma$  (if  $m = 0.5$ , Figure 5.13) and is implemented through an increase in shear velocity threshold. The shear velocity threshold also affects aeolian sediment already in transport and originating from upwind, unarmored beach areas, like the mixed zones. Sediments from upwind areas are therefore partially deposited in the aeolian zone as soon a beach armor layer develops. For low values for  $\sigma$  the local deposition of sediment from upwind areas is already significant with low shell coverage. Low  $\sigma$  values therefore reduce the total sediment accumulation in the dunes quickly. In order for the model to provide reasonable total sediment transport rates, a higher value for  $\sigma$  was found in the calibration that ultimately induces a higher shell coverage. The value for  $\sigma$  therefore does not only represent a spatiotemporal averaged emergence of roughness elements, but also a compromise between its effect on the fluid and impact velocity threshold.

## 5.6 CONCLUSIONS

The Sand Motor hindcast shows that the reduction of aeolian sediment availability due to soil moisture and beach armoring can largely explain the low accumulation volumes in the Sand Motor domain. The AeOLiS model has shown to be quantitatively valuable and practically applicable. The model provides a framework for the description of complex spatiotemporal variations in aeolian sediment availability and its relation to sediment transport that has not yet been exploited in full.

2760 From the hindcast the following conclusions can be drawn:

- 2761 • The AEOLiS model is able to reproduce multi-annual aeolian sediment transport  
2762 rates in the Sand Motor domain in the four years after its construction with a  
2763 RMSE of  $3 \cdot 10^4$  m<sup>3</sup> and R<sup>2</sup> of 0.92 when time series of measured and modeled  
2764 total aeolian sediment transport volumes are compared.
- 2765 • The AEOLiS model is able to reproduce large scale spatial patterns in aeolian  
2766 sediment transport in the Sand Motor domain in the four years after its con-  
2767 struction, but underestimates the deposition in the dune lake and lagoon.
- 2768 • The AEOLiS model overestimates the total sedimentation volume with 5% on  
2769 average, but underestimates the total sedimentation volume with 12% at the end  
2770 of the simulation. The discrepancy at the end of the simulation might be caused  
2771 by a particularly dry season as precipitation is not included in the simulations.
- 2772 • The AEOLiS model is able to capture the seasonal variations in sediment trans-  
2773 port in all years, except for early 2014 when significant morphological change is  
2774 possibly related to hydrodynamic sediment transport that is not included in the  
2775 simulations.
- 2776 • The AEOLiS model overestimates the shell coverage, which compensates the  
2777 high value for σ. The high σ value is a compromise between the fluid and  
2778 impact threshold that are currently assumed to be equal.
- 2779 • The combination of spatial and temporal variations in aeolian sediment avail-  
2780 ability, due to the combined influence of soil moisture, sediment sorting and  
2781 beach armoring, and the feedback between aeolian sediment availability and  
2782 transport is essential for an accurate estimate of the total sedimentation volume  
2783 and the corresponding aeolian sediment source areas in the Sand Motor domain.

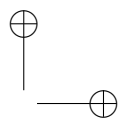
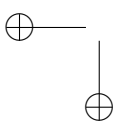
2784

## Part III

2785

### DISCUSSION AND CONCLUSIONS

2786





# 6

2787  
2788

---

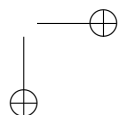
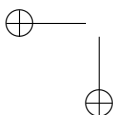
## 2789 DISCUSSION

---

2790 This thesis explored the nature of aeolian sediment availability. Aeolian sediment  
2791 availability is generally associated with the shear velocity threshold. Alternatively,  
2792 sediment availability can be expressed in terms of critical fetch (Bauer and Davidson-  
2793 Arnott, 2002) or explicitly following de Vries et al. (2014a). The latter two approaches  
2794 deviate rather radically from the legacy of aeolian research. Both discard the abun-  
2795 dantly available relations between bed surface properties, sediment availability and  
2796 the shear velocity threshold. Instead, they describe sediment availability in new terms  
2797 for which no quantification is known. In Chapter 4 it is argued that the new ap-  
2798 proaches have a right to exist as they allow for an increased complexity in situations  
2799 that can be described by models. Ultimately, the approach of de Vries et al. (2014a)  
2800 is adopted for this thesis and adapted to support multi-fraction sediment transport  
2801 in order to simulate sediment sorting and beach armoring that introduces feedback  
2802 between aeolian sediment availability and transport in aeolian sediment transport  
2803 modeling.

2804 The model approach presented in this thesis is a unification of the classic approach  
2805 based on the shear velocity threshold and the approach of de Vries et al. (2014a).  
2806 Whereas de Vries et al. (2014a) use a user-defined value for the sediment availabil-  
2807 ity  $m_a$  (or  $S_e$ ) to truncate the instantaneous sediment transport in their model, the  
2808 approach presented in this thesis uses simulation to determine the local sediment  
2809 availability  $m_{a,k}$ . The weighting factor  $\hat{w}_k$  is subsequently adapted to the local sedi-  
2810 ment availability (Equation 4.9). Since the weighting factor  $\hat{w}_k$  is essentially a space-  
2811 and time-dependent modification to the shear velocity threshold, this new approach  
2812 connects the field of availability-limited aeolian sediment transport modeling with the  
2813 long history of aeolian research.

2814 Availability-limited aeolian sediment transport modeling can be further improved  
2815 by distinguishing between the fluid and impact threshold in future versions of the pre-  
2816 sented model. The presented model provides a framework in which such distinction  
2817 can be made rather naturally. The bed interaction parameter essentially implements  
2818 this distinction already for armored beach surfaces, but a more generic implemen-  
2819 tation is required for coastal systems with large spatial variations in sediment avail-  
2820 ability. A key issue is still that relations between bed surface properties, sediment  
2821 availability and the shear velocity threshold are typically derived as bulk formula-  
2822 tion for the fluid and impact threshold together. A proper implementation of the  
2823 fluid and impact threshold in the presented model therefore depends on a substantial  
2824 investment in data collection (e.g. Martin and Kok, 2016).



2825 The presented model for availability-limited aeolian sediment transport can also be  
2826 applied to availability-abundant coastal systems. However, much of the complexity in  
2827 coastal aeolian sediment transport modeling is related to aeolian sediment availabil-  
2828 ity. The approach might be considered too complex for more regular situations where  
2829 sediment availability is abundant. A key issue is that assessing whether a coastal  
2830 environment is availability-limited or not is not trivial. In this thesis established for-  
2831 mulations for equilibrium aeolian sediment transport are used to roughly estimate the  
2832 sediment availability of coastal systems. However, if the presented model is proven  
2833 to be sufficiently accurate in availability-abundant coastal systems, it might be used  
2834 to formulate rules of thumb to assess coastal systems on their sediment availabil-  
2835 ity more accurately. Subsequently, the model might be used to assess these coastal  
2836 systems that are found to be availability-limited or facilitate the formulation of aggre-  
2837 gated relations between aeolian sediment availability and transport that would serve  
2838 a more rapid assessment.

2839 In hindsight, the chapters in this thesis reveal a certain chronology in understand-  
2840 ing the phenomenon of aeolian sediment availability. Deducing the significance of  
2841 sediment availability from the large scale sediment budget analysis or the small scale  
2842 sediment transport measurements was not trivial as sediment availability appeared  
2843 to be rather intangible. This started with the slightly ambiguous use of terminology  
2844 in literature where, for example, *sediment supply* is often mistaken to be equal to *sediment*  
2845 *availability* or the *shear velocity threshold*. In addition, various aeolian, marine and  
2846 meteorological processes affect aeolian sediment availability and/or the shear veloc-  
2847 ity threshold differently and on various temporal and spatial scales. Consequently,  
2848 significant time was spent to narrow down the essence of sediment availability and  
2849 define a distinctive terminology accordingly. The phenomenon of aeolian sediment  
2850 availability was made tangible in a numerical model for aeolian sediment availability  
2851 and transport that is unique in that it describes aspects essential to aeolian sediment  
2852 availability and transport modeling that have previously been subject to research, but  
2853 never been combined in a comprehensive model approach. The main contribution of  
2854 the model is the *combined* simulation of:

- 2855 1. Temporal variations in aeolian sediment availability and transport.
- 2856 2. Spatial variations in aeolian sediment availability and transport.
- 2857 3. Recurrence relation between aeolian sediment availability and transport through  
2858 self-grading of sediment.
- 2859 4. Simulation of multiple availability-limiting processes and their combined influ-  
2860 ence on aeolian sediment transport.
- 2861 5. Natural differentiation between fluid and impact shear velocity threshold (not  
2862 implemented).

2863 As illustrated by the Sand Motor hindcast presented in Chapter 5, the combined  
2864 influence of various aspects of aeolian sediment availability is essential to obtain reli-  
2865 able estimates of aeolian sediment transport and dune growth for which the presented  
2866 model provides a general framework. Notwithstanding that model development just  
2867 started and needs further extension, calibration and validation to make it generally  
2868 applicable.

2869 Based on the Sand Motor hindcast several opportunities for future model improvement  
 2870 have been identified:

- 2871 • Support for local variations in wind shear due to morphological feedback.

2872 Neither deposition in front of the dunes nor deposition in the lee of the Sand  
 2873 Motor crest is currently simulated as morphological feedback with the wind  
 2874 is not taken into account. Given the discrepancy in the spatial distribution of  
 2875 aeolian sediment deposits between measurements and model result, it seems  
 2876 advisable to provide the model with local variations in wind shear. The model  
 2877 of Kroy et al. (2002) based on the derivation of the local wind field by Weng  
 2878 et al. (1991) might provide a description of the local variations in wind shear for  
 2879 which the computational effort relates well to the presented model.

- 2880 • Support for the effect of wind gusts.

2881 The calibrated model is forced by an hourly averaged wind time series. The use  
 2882 of hourly averaged values for wind speed neglects the gustiness of the wind.  
 2883 Wind gusts might influence sediment transport significantly as the relation be-  
 2884 tween wind speed and sediment transport is nonlinear. However, providing  
 2885 the model with high resolution wind time series would not be beneficial in  
 2886 combination with the diffusive implicit numerical scheme. To solve for the ef-  
 2887 fect of gustiness an explicit or semi-implicit numerical scheme can be used, but  
 2888 such scheme would not be computationally feasible for long-term simulations.  
 2889 Moreover, since saltation is not purely an advective mode of transport, the as-  
 2890 sumption of advection might be violated for very short time scales as interaction  
 2891 with the bed becomes dominant.

2892 As an alternative, the influence of gusts can be parameterized. It can be argued  
 2893 that some persistence is needed for gusts to influence sediment transport, re-  
 2894 sulting in a lower boundary of the temporal resolution of the wind time series.  
 2895 The distribution of the wind speed with respect to the hourly average can then  
 2896 provide a basis for a gustiness factor that increases the global wind shear.

- 2897 • Support for differentiation between the fluid and impact shear velocity thresh-  
 2898 olds.

2899 The sediment transport capacity is currently implemented identical for the initia-  
 2900 tion and continuation of motion as no distinction between the fluid and impact  
 2901 threshold is made. The Sand Motor hindcast illustrates how this restriction af-  
 2902 fects the influence of roughness elements on aeolian sediment availability. Sim-  
 2903 ilar to the implementation of the bed interaction parameter, that distinguishes  
 2904 between the grain size distribution in the bed and the air, a distinction between  
 2905 fluid and impact threshold can be implemented.

2906 The right-hand side of the advection equation (Equation 4.9) can be modified  
 2907 according to:

$$E_k - D_k = \min \left( \frac{\partial m_{a,k}}{\partial t} ; \frac{\hat{w}_k}{T} \cdot [(1 - S_k) \cdot c_{sat,k}^{fluid} + S_k \cdot c_{sat,k}^{impact} - c_k] \right) \quad (6.1)$$

2908 where  $c_{sat,k}^{\text{fluid}}$  [kg/m<sup>2</sup>] and  $c_{sat,k}^{\text{fluid}}$  [kg/m<sup>2</sup>] are the sediment transport capacity associated with the fluid and impact threshold respectively and  $S_k$  [-] is the degree of saturation defined as:

$$S_k = \sum_{k=1}^{n_k} \frac{c_k}{c_{sat,k}^{\text{impact}}} \quad (6.2)$$

2911 Note that the weighting factor  $\hat{w}_k$  already distinguishes between sediment in  
 2912 the air and in the bed, depending on the saturation and the bed interaction  
 2913 parameter and therefore appears outside the brackets.

2914 Although the presented model conceptually allows to differentiate between the  
 2915 impact and fluid threshold, empirical data to quantify the differentiation is lack-  
 2916 ing. This model improvement is therefore hypothetical at the current stage of  
 2917 development.

- 2918 • Support for independent definition of the active bed layer.

2919 The top bed composition layer currently acts as active bed layer, but at the same  
 2920 time defines the vertical resolution of the sorting and armoring processes. As  
 2921 these are two fundamentally different properties of the model, it is advisable  
 2922 to define the active bed layer separate from the numerical resolution. A prob-  
 2923 ability distribution can be defined that describes the probability of sediment to  
 2924 be eroded from a specific layer, which would logically decrease with the depth.  
 2925 The bed composition layer thickness would than uniquely determine the vertical  
 2926 resolution of sorting and armoring.

- 2927 • Online model coupling

2928 The Sand Motor hindcast showed the importance of an accurate description of  
 2929 the hydrodynamics for accurate estimates of the development of the aeolian sed-  
 2930 imentation and erosion volumes. Similarly, groundwater seepage might influ-  
 2931 ence the aeolian sediment deposition around the lagoon and dune lake, which  
 2932 would require a description of the groundwater level to be implemented.

2933 It can be questioned if such detailed descriptions of hydrodynamic and hydro-  
 2934 logical processes are still within the scope of an aeolian sediment transport  
 2935 model. Alternatively, online model coupling with dedicated models for near-  
 2936 shore hydrodynamics and hydrology through the Basic Model Interface (BMI)  
 2937 can be pursued.

# 7

2938

2939

---

## 2940 CONCLUSIONS

---

2941 This thesis concludes with addressing the research questions formulated in the intro-  
2942 ductory chapter (Chapter 1). Each question is addressed with relevant references to  
2943 the four main chapters 2 to 5.

2944 **RESEARCH OBJECTIVE #1** Identify the main sources for aeolian sediment in coastal  
2945 environments and particularly at the Sand Motor mega nourishment.

2946 The research questions and answers related to objective #1 are:

2947 1.1 What is the total aeolian sediment supply at the Sand Motor mega nour-  
2948 ishment?

2949 The total aeolian sediment supply accumulated to 400.000 m<sup>3</sup> in the first  
2950 four years after construction of the Sand Motor (Section 2.4.2). About  
2951 120.000 m<sup>3</sup> accumulated in the first half year after construction. From  
2952 January 2012 the accumulation rate of aeolian sediment reduced with two-  
2953 third to about 80.000 m<sup>3</sup>/yr.

2954 1.2 What are the main deposition areas of aeolian sediment at the Sand Motor  
2955 mega nourishment?

2956 Aeolian sediment in the Sand Motor region is deposited in the dunes (50%),  
2957 dune lake (25%) and lagoon (25%, Section 2.4.1). The deposits in the dunes  
2958 increased with respect to the dune lake and lagoon over the course of four  
2959 years since construction of the Sand Motor. In addition, aeolian sediment  
2960 is likely to be deposited offshore as well. The associated sediment volume  
2961 is unknown, but estimated by the numerical model as 10% of the measured  
2962 deposition volume (Section 5.4).

2963 1.3 What are the main source areas of aeolian sediment at the Sand Motor  
2964 mega nourishment?

2965 Aeolian sediment in the Sand Motor region originates from the dry beach  
2966 area (aeolian zone, 33%) and the intertidal and low-lying supratidal beach  
2967 areas (mixed zones, 67%, Section 2.5). The relative importance of the mixed  
2968 zones is notable as it is periodically flooded and the majority of the north-  
2969 ern mixed zone is oriented unfavorable with respect to the wind.

2970 1.4 What bed surface characteristics can explain any spatial variations in aeo-  
2971 lian sediment supply at the Sand Motor mega nourishment?

2972 Aeolian sediment supply from the Sand Motor's dry beach area (aeolian  
2973 zone) is likely to be reduced due to beach armoring. However, beach ar-  
2974 moring is probably not the only relevant bed surface characteristic as the  
2975 formation of salt crusts has a similar limiting effect on aeolian sediment  
2976 supply (Section 2.5.2).

2977 The reduction of aeolian sediment supply from the aeolian zone makes the  
2978 intertidal and low-lying supratidal beach areas (mixed zones) relatively  
2979 important as supplier of aeolian sediment. The periodic flooding and high  
2980 moisture contents are known to limit aeolian sediment supply, but appar-  
2981 ently to a lesser extent than beach armoring (Section 2.5.2).

2982 1.5 What is the relevance of these bed surface characteristics for coastal sys-  
2983 tems in general?

2984 While high moisture contents are found at any tidal beach, beach armor-  
2985 ing is especially relevant to large scale nourishments constructed above  
2986 storm surge level. Sand borrowed from the sea bottom and used to widen  
2987 or strengthen the coast tends to contain many shells and other roughness  
2988 elements. As these elements tend to emerge from the bed due to win-  
2989 nowing of fine sediment, beach armoring is an inherent process on such  
2990 beaches. In case beach armoring occurs, aeolian sediment supply from  
2991 the intertidal and low-lying supratidal beach areas (mixed zones) becomes  
2992 more important and consequently also soil moisture content, infiltration  
2993 and evaporation rates.

2994 1.6 What characteristics of a coastal system determine aeolian sediment supply  
2995 and dune growth?

2996 The intertidal and low-lying supratidal beach areas seem to be a more reli-  
2997 able indicator for aeolian sediment supply and dune growth along coasts  
2998 with beach armoring than (dry) beach fetch (Section 3.4.2).

2999 RESEARCH OBJECTIVE #2 Identify the main processes that govern aeolian sediment  
3000 availability and supply in coastal environments and particularly at the Sand  
3001 Motor mega nourishment.

3002 The research questions and answers related to objective #2 are:

3003 2.1 What bed surface characteristics are related to aeolian sediment supply?

3004 Significant changes in spatial gradients in aeolian sediment transport at  
3005 the Sand Motor coincide with the presence of a beach armor layer. This  
3006 suggests that beach armoring is a dominant process in the reduction of ae-  
3007 olian sediment supply (Section 3.4.3). Spatial gradients in aeolian sediment  
3008 transport also seem to be related to topographic features, like the transition  
3009 from berm slope to berm flat. Such features seem to promote deposition  
3010 of aeolian sediment (negative supply).

3011 2.2 What processes govern the supply of aeolian sediment from the source  
3012 areas?

Aeolian sediment supply at the Sand Motor is governed by the development of a beach armor layer (Section 3.5). The reduction of aeolian sediment supply from the dry beach area increases the importance of aeolian sediment supply from the intertidal beach areas. Aeolian sediment supply from the mixed zone is governed by the periodic flooding of the intertidal beach. The timescales involved in the flooding and drying of the intertidal beach seems to be short, resulting in an swift response of the sediment supply to the instantaneous waterline position. Local deposits on the berm flat seem to act as temporary sediment source during high water or high moisture contents resulting in a continuous supply from the intertidal beach (Section 3.5).

2.3 What processes govern the deposition of aeolian sediment in the deposition areas?

Aeolian sediment deposits at the Sand Motor are found in typical areas with either low shear velocities, due to the presence of vegetation (dunes) or morphological feedback with the wind (lee of the Sand Motor crest), or high shear velocity threshold, due to high moisture contents or free water surfaces (dune lake, lagoon and offshore). Local deposits on the berm flat seem to act as temporary sediment source during high water or high moisture contents resulting in a continuous supply from the intertidal beach (Section 3.5). Alongshore variations in sediment deposition seem to be caused by blockage of aeolian sediment transport pathways (Section 2.4.3).

RESEARCH OBJECTIVE #3 Develop a numerical model approach to describe the influence of spatiotemporal variations in aeolian sediment availability on aeolian sediment transport and harmonize existing model approaches to aeolian sediment availability where possible.

The research questions and answers related to objective #3 are:

3.1 What are existing model approaches to describe the influence of aeolian sediment availability on aeolian sediment transport, what are the similarities and differences among them and which approaches are mutually exclusive?

Three approaches can be distinguished in literature: the shear velocity threshold, the critical fetch and the explicit formulation of sediment availability (Section 4.3). All approaches are related, but differ in the amount of spatiotemporal variability in sediment availability they can allow. The approach based on critical fetch is mutually exclusive with the approach based on the explicit formulation of sediment availability as the latter provides the critical fetch as model result. The approach based on an explicit formulation of sediment availability is, in the form presented in this thesis, a spatiotemporal advection framework for the shear velocity threshold that in addition allows for feedback between aeolian sediment availability and transport as well as differentiation between the impact and fluid threshold.

3056           3.2 What processes that were identified to be relevant to aeolian sediment  
3057           availability are not covered with sufficient accuracy by existing model ap-  
3058           proaches?

3059           Spatiotemporal variations in beach armoring is shown to be a governing  
3060           process at the Sand Motor mega nourishment and likely other nourished  
3061           beaches. Especially the spatiotemporal variations are not sufficiently accu-  
3062           rately described in existing models for aeolian sediment transport (Section  
3063           4.2).

3064           3.3 What are the requirements for a model approach that harmonizes existing,  
3065           mutual inclusive model approaches and is conceptually able to describe all  
3066           processes relevant to aeolian sediment availability and transport?

3067           The approach is based on the legacy of aeolian research, being the abun-  
3068           dantly available relations between aeolian sediment availability and trans-  
3069           port. It describes feedback between wind and transport as well as sediment  
3070           availability and transport (Section 4.3). It distinguishes between the fluid  
3071           and impact threshold (Section 6).

3072           **RESEARCH OBJECTIVE #4** Validate the numerical model approach to reproduce the  
3073           location and size of sources for aeolian sediment in coastal environments and  
3074           particularly at the Sand Motor mega nourishment.

3075           The research questions and answers related to objective #4 are:

3076           4.1 Can the calibrated numerical model reproduce the total aeolian sediment  
3077           supply at the Sand Motor mega nourishment with any statistical signifi-  
3078           cance?

3079           Yes. The total aeolian sediment supply over the course of 4 years is rep-  
3080           resented with an  $R^2$  value of 0.93 and an RMSE of  $3 \cdot 10^4 \text{ Mm}^3$  (Section  
3081           5.4).

3082           4.2 Can the calibrated numerical model reproduce the main source and depo-  
3083           sition areas at the Sand Motor mega nourishment?

3084           Yes. the relative contribution of the intertidal beach was estimated to be  
3085           55% based on the large scale sediment budget analysis, which is well rep-  
3086           resented by the calibrated model.

3087           4.3 What implemented processes are in retrospect significant to the model re-  
3088           sult?

3089           Both the drying of the intertidal beach and sediment sorting and beach  
3090           armoring are crucial for the model result. Moreover, both the spatial and  
3091           temporal variations affect the model result significantly (Section 5.4).

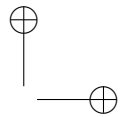
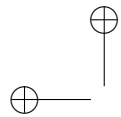
3092

## Part IV

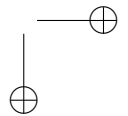
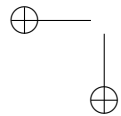
3093

### APPENDICES

3094



"thesis" — 2016/11/15 — 10:57 — page 104 — #134



# A

3095

3096

---

## 3097 THEORETICAL SEDIMENT TRANSPORT VOLUMES

---

3098 The cumulative theoretical sediment transport volume  $Q$  [ $\text{m}^3$ ] in the Sand Motor do-  
 3099 main between September 1, 2011 and September 1, 2015 is estimated from hourly  
 3100 averaged measured wind speed  $u_{10}$  [ $\text{m}/\text{s}$ ] and direction  $\theta_u$  [ $^\circ$ ] measured at 10 m  
 3101 height by the KNMI meteorological station in Hoek van Holland (Figure 2.2). The  
 3102 wind time series are used in conjunction with the formulation of [Bagnold \(1937b\)](#) to  
 3103 obtain the instantaneous theoretical sediment transport rate  $q$  [ $\text{kg}/\text{m}/\text{s}$ ] following:

$$3104 q = C \frac{\rho_a}{g} \sqrt{\frac{d_n}{D_n}} (u_* - u_{*th})^3 \quad (\text{A.1})$$

3105 with the shear velocity  $u_* = \alpha \cdot u_{10}$   $\text{m}/\text{s}$ , the shear velocity threshold  $u_{*th} = \alpha \cdot 3.87$   
 3106  $\text{m}/\text{s}$ , the conversion factor from free-flow wind velocity to shear velocity  $\alpha = 0.058$ ,  
 3107 the air density  $\rho_a = 1.25 \text{ kg}/\text{m}^3$ , the particle density  $\rho_p = 2650.0 \text{ kg}/\text{m}^3$ , the gravita-  
 3108 tional constant  $g = 9.81 \text{ m}/\text{s}^2$ , the nominal grain size  $d_n = 335 \mu\text{m}$  and a reference  
 3109 grain size  $D_n = 250 \mu\text{m}$ .

3110 The cumulative theoretical sediment transport volumes in onshore ( $Q_{os}$  [ $\text{m}^3$ ]) and  
 3111 alongshore ( $Q_{as}$  [ $\text{m}^3$ ]) direction are computed by time integration and conversion  
 3112 from mass to volume following:

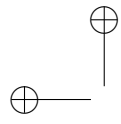
$$3113 Q_{os} = \sum q \cdot \frac{\Delta t \cdot \Delta y}{(1-p) \cdot \rho_p} \cdot f_{\theta_u, os} = 110 \cdot 10^4 \text{ m}^3 \\ Q_{as} = \sum q \cdot \frac{\Delta t \cdot \Delta x}{(1-p) \cdot \rho_p} \cdot f_{\theta_u, as} = 3 \cdot 10^4 \text{ m}^3 \quad (\text{A.2})$$

3114 where the temporal resolution  $\Delta t = 1 \text{ h}$ , the alongshore span of the measurement  
 3115 domain  $\Delta y = 4 \text{ km}$ , the approximate lateral beach width  $\Delta x = 100 \text{ m}$ , the porosity  
 3116  $p = 0.4$  and  $f_{\theta_u, os}$  and  $f_{\theta_u, as}$  are factors to account for respectively the onshore and  
 3117 alongshore wind directions only, defined as:

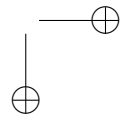
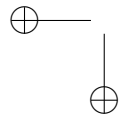
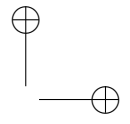
$$3118 f_{\theta_u, os} = \max(0 ; \cos(312^\circ - \theta_u)) \\ f_{\theta_u, as} = \sin(312^\circ - \theta_u) \quad (\text{A.3})$$

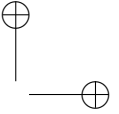
3119 where  $\theta_u$  [ $^\circ$ ] is the hourly averaged wind direction and  $312^\circ$  accounts for orientation  
 3120 of the original coastline.

3121 Note that the difference between the onshore and alongshore cumulative theoretical  
 3122 sediment transport volumes (Equation A.2) of a factor 40 is determined solely by  
 3123 the difference between the onshore and alongshore cross-sections of 4 km and 100  
 3124 m respectively. The sediment transport volumes per meter width in onshore and  
 3125 alongshore direction are of the same order of magnitude ( $275 \text{ m}^3/\text{m}$  and  $267 \text{ m}^3/\text{m}$   
 3126 respectively).



"thesis" — 2016/11/15 — 10:57 — page 106 — #136





# B

3124

3125

---

## 3126 NUMERICAL IMPLEMENTATION

---

3127 The numerical implementation of the equations presented in Chapter 4 is explained  
 3128 in this appendix. The implementation is available as Python package through the  
 3129 OpenEarth GitHub repository at: [github.com/openearth/aeolis-python/](https://github.com/openearth/aeolis-python/)

3130 **B.1 ADVECTION EQUATION**

3131 The advection equation (Equation 4.6) is implemented in two-dimensional form fol-  
 3132 lowing:

$$\frac{\partial c}{\partial t} + u_{z,x} \frac{\partial c}{\partial x} + u_{z,y} \frac{\partial c}{\partial y} = \frac{c_{\text{sat}} - c}{T} \quad (\text{B.1})$$

3133 in which  $c$  [ $\text{kg}/\text{m}^2$ ] is the sediment mass per unit area in the air,  $c_{\text{sat}}$  [ $\text{kg}/\text{m}^2$ ] is the  
 3134 maximum sediment mass in the air that is reached in case of saturation,  $u_{z,x}$  and  $u_{z,y}$   
 3135 are the x- and y-component of the wind velocity at height  $z$  [m],  $T$  [s] is an adaptation  
 3136 time scale,  $t$  [s] denotes time and  $x$  [m] and  $y$  [m] denote cross-shore and alongshore  
 3137 distances respectively.

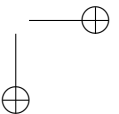
3138 The formulation is discretized following a first order upwind scheme assuming that  
 3139 the wind velocity  $u_z$  is positive in both x-direction and y-direction:

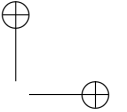
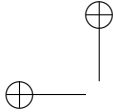
$$\begin{aligned} \frac{c_{i,j,k}^{n+1} - c_{i,j,k}^n}{\Delta t^n} + u_{z,x}^n \frac{c_{i,j,k}^n - c_{i-1,j,k}^n}{\Delta x_{i,j}} + u_{z,y}^n \frac{c_{i,j,k}^n - c_{i,j-1,k}^n}{\Delta y_{i,j}} \\ = \frac{\hat{w}_{i,j,k}^n \cdot c_{\text{sat},i,j,k}^n - c_{i,j,k}^n}{T} \end{aligned} \quad (\text{B.2})$$

3140 in which  $n$  is the time step index,  $i$  and  $j$  are the cross-shore and alongshore spatial  
 3141 grid cell indices and  $k$  is the grain size fraction index.  $w$  [-] is the weighting factor de-  
 3142 fined in Equation 4.10a and used for the weighted addition of the saturated sediment  
 3143 concentrations over all grain size fractions.

3144 The discretization can be generalized for any wind direction as:

$$\begin{aligned} \frac{c_{i,j,k}^{n+1} - c_{i,j,k}^n}{\Delta t^n} + u_{z,x+}^n c_{i,j,k,x-}^n + u_{z,y+}^n c_{i,j,k,y-}^n \\ + u_{z,x-}^n c_{i,j,k,x+}^n + u_{z,y-}^n c_{i,j,k,y+}^n = \frac{\hat{w}_{i,j,k}^n \cdot c_{\text{sat},i,j,k}^n - c_{i,j,k}^n}{T} \end{aligned} \quad (\text{B.3})$$





3145 in which:

$$\begin{aligned} u_{z,x+}^n &= \max(0, u_{z,x}^n) & ; \quad u_{z,y+}^n &= \max(0, u_{z,y}^n) \\ u_{z,x-}^n &= \min(0, u_{z,x}^n) & ; \quad u_{z,y-}^n &= \min(0, u_{z,y}^n) \end{aligned} \quad (\text{B.4})$$

3146 and

$$\begin{aligned} c_{i,j,k,x+}^n &= \frac{c_{i+1,j,k}^n - c_{i,j,k}^n}{\Delta x} & ; \quad c_{i,j,k,y+}^n &= \frac{c_{i,j+1,k}^n - c_{i,j,k}^n}{\Delta y} \\ c_{i,j,k,x-}^n &= \frac{c_{i,j,k}^n - c_{i-1,j,k}^n}{\Delta x} & ; \quad c_{i,j,k,y-}^n &= \frac{c_{i,j,k}^n - c_{i,j-1,k}^n}{\Delta y} \end{aligned} \quad (\text{B.5})$$

3147 Equation B.3 is explicit in time and adheres to the Courant-Friedrich-Lewis (CFL) condition for numerical stability. Alternatively, the advection equation can be discretized implicitly in time for unconditional stability:

$$\begin{aligned} \frac{c_{i,j,k}^{n+1} - c_{i,j,k}^n}{\Delta t^n} + u_{z,x+}^{n+1} c_{i,j,k,x-}^{n+1} + u_{z,y+}^{n+1} c_{i,j,k,y-}^{n+1} \\ + u_{z,x-}^{n+1} c_{i,j,k,x+}^{n+1} + u_{z,y-}^{n+1} c_{i,j,k,y+}^{n+1} = \frac{\hat{w}_{i,j,k}^{n+1} \cdot c_{\text{sat},i,j,k}^{n+1} - c_{i,j,k}^{n+1}}{\Gamma} \end{aligned} \quad (\text{B.6})$$

3150 Equation B.3 and B.6 can be rewritten as:

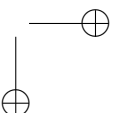
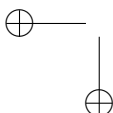
$$\begin{aligned} c_{i,j,k}^{n+1} &= c_{i,j,k}^n - \Delta t^n \left[ u_{z,x+}^n c_{i,j,k,x-}^n + u_{z,y+}^n c_{i,j,k,y-}^n \right. \\ &\quad \left. + u_{z,x-}^n c_{i,j,k,x+}^n + u_{z,y-}^n c_{i,j,k,y+}^n - \frac{\hat{w}_{i,j,k}^n \cdot c_{\text{sat},i,j,k}^n - c_{i,j,k}^n}{\Gamma} \right] \end{aligned} \quad (\text{B.7})$$

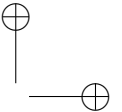
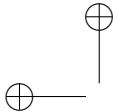
3151 and

$$\begin{aligned} c_{i,j,k}^{n+1} + \Delta t^n \left[ u_{z,x+}^{n+1} c_{i,j,k,x-}^{n+1} + u_{z,y+}^{n+1} c_{i,j,k,y-}^{n+1} \right. \\ \left. + u_{z,x-}^{n+1} c_{i,j,k,x+}^{n+1} + u_{z,y-}^{n+1} c_{i,j,k,y+}^{n+1} - \frac{\hat{w}_{i,j,k}^{n+1} \cdot c_{\text{sat},i,j,k}^{n+1} - c_{i,j,k}^{n+1}}{\Gamma} \right] = c_{i,j,k}^n \end{aligned} \quad (\text{B.8})$$

3152 and combined using a weighted average:

$$\begin{aligned} c_{i,j,k}^{n+1} + \Gamma \Delta t^n \left[ u_{z,x+}^{n+1} c_{i,j,k,x-}^{n+1} + u_{z,y+}^{n+1} c_{i,j,k,y-}^{n+1} \right. \\ \left. + u_{z,x-}^{n+1} c_{i,j,k,x+}^{n+1} + u_{z,y-}^{n+1} c_{i,j,k,y+}^{n+1} - \frac{\hat{w}_{i,j,k}^{n+1} \cdot c_{\text{sat},i,j,k}^{n+1} - c_{i,j,k}^{n+1}}{\Gamma} \right] \\ = c_{i,j,k}^n - (1 - \Gamma) \Delta t^n \left[ u_{z,x+}^n c_{i,j,k,x-}^n + u_{z,y+}^n c_{i,j,k,y-}^n \right. \\ \left. + u_{z,x-}^n c_{i,j,k,x+}^n + u_{z,y-}^n c_{i,j,k,y+}^n - \frac{\hat{w}_{i,j,k}^n \cdot c_{\text{sat},i,j,k}^n - c_{i,j,k}^n}{\Gamma} \right] \end{aligned} \quad (\text{B.9})$$





3153 in which  $\Gamma$  is a weight that ranges from 0 – 1 and determines the implicitness of the  
 3154 scheme. The scheme is implicit with  $\Gamma = 0$ , explicit with  $\Gamma = 1$  and semi-implicit  
 3155 otherwise.  $\Gamma = 0.5$  results in the semi-implicit Crank-Nicolson scheme.

3156 Equation B.5 is back-substituted in Equation B.9:

$$\begin{aligned} c_{i,j,k}^{n+1} + \Gamma \Delta t^n & \left[ u_{z,x+}^{n+1} \frac{c_{i,j,k}^{n+1} - c_{i-1,j,k}^{n+1}}{\Delta x} + u_{z,y+}^{n+1} \frac{c_{i,j,k}^{n+1} - c_{i,j-1,k}^{n+1}}{\Delta y} \right. \\ & \left. + u_{z,x-}^{n+1} \frac{c_{i+1,j,k}^{n+1} - c_{i,j,k}^{n+1}}{\Delta x} + u_{z,y-}^{n+1} \frac{c_{i,j+1,k}^{n+1} - c_{i,j,k}^{n+1}}{\Delta y} - \frac{\hat{w}_{i,j,k}^{n+1} \cdot c_{\text{sat},i,j,k}^{n+1} - c_{i,j,k}^{n+1}}{\Gamma} \right] \\ & = c_{i,j,k}^n - (1 - \Gamma) \Delta t^n \left[ u_{z,x+}^n \frac{c_{i,j,k}^n - c_{i-1,j,k}^n}{\Delta x} + u_{z,y+}^n \frac{c_{i,j,k}^n - c_{i,j-1,k}^n}{\Delta y} \right. \\ & \left. + u_{z,x-}^n \frac{c_{i+1,j,k}^n - c_{i,j,k}^n}{\Delta x} + u_{z,y-}^n \frac{c_{i,j+1,k}^n - c_{i,j,k}^n}{\Delta y} - \frac{\hat{w}_{i,j,k}^n \cdot c_{\text{sat},i,j,k}^n - c_{i,j,k}^n}{\Gamma} \right] \quad (\text{B.10}) \end{aligned}$$

3157 and rewritten:

$$\begin{aligned} & \left[ 1 + \Gamma \left( u_{z,x+}^{n+1} \frac{\Delta t^n}{\Delta x} + u_{z,y+}^{n+1} \frac{\Delta t^n}{\Delta y} - u_{z,x-}^{n+1} \frac{\Delta t^n}{\Delta x} - u_{z,y-}^{n+1} \frac{\Delta t^n}{\Delta y} + \frac{\Delta t^n}{\Gamma} \right) \right] c_{i,j,k}^{n+1} \\ & - \Gamma \left( u_{z,x+}^{n+1} \frac{\Delta t^n}{\Delta x} c_{i-1,j,k}^{n+1} + u_{z,y+}^{n+1} \frac{\Delta t^n}{\Delta y} c_{i,j-1,k}^{n+1} - u_{z,x-}^{n+1} \frac{\Delta t^n}{\Delta x} c_{i+1,j,k}^{n+1} - u_{z,y-}^{n+1} \frac{\Delta t^n}{\Delta y} c_{i,j+1,k}^{n+1} \right) \\ & = \left[ 1 - (1 - \Gamma) \left( u_{z,x+}^n \frac{\Delta t^n}{\Delta x} + u_{z,y+}^n \frac{\Delta t^n}{\Delta y} - u_{z,x-}^n \frac{\Delta t^n}{\Delta x} - u_{z,y-}^n \frac{\Delta t^n}{\Delta y} + \frac{\Delta t^n}{\Gamma} \right) \right] c_{i,j,k}^n \\ & + (1 - \Gamma) \left( u_{z,x+}^n \frac{\Delta t^n}{\Delta x} c_{i-1,j,k}^n + u_{z,y+}^n \frac{\Delta t^n}{\Delta y} c_{i,j-1,k}^n - u_{z,x-}^n \frac{\Delta t^n}{\Delta x} c_{i+1,j,k}^n - u_{z,y-}^n \frac{\Delta t^n}{\Delta y} c_{i,j+1,k}^n \right) \\ & \quad + \Gamma \hat{w}_{i,j,k}^{n+1} \cdot c_{\text{sat},i,j,k}^{n+1} \frac{\Delta t^n}{\Gamma} + (1 - \Gamma) \hat{w}_{i,j,k}^n \cdot c_{\text{sat},i,j,k}^n \frac{\Delta t^n}{\Gamma} \quad (\text{B.11}) \end{aligned}$$

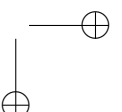
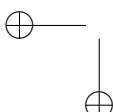
3158 and simplified:

$$a_{i,j}^{0,0} c_{i,j,k}^{n+1} + a_{i,j}^{1,0} c_{i+1,j,k}^{n+1} + a_{i,j}^{0,1} c_{i,j+1,k}^{n+1} - a_{i,j}^{-1,0} c_{i-1,j,k}^{n+1} - a_{i,j}^{0,-1} c_{i,j-1,k}^{n+1} = y_{i,j,k} \quad (\text{B.12})$$

3159 where the implicit coefficients are defined as:

$$\begin{aligned} a_{i,j}^{0,0} &= \left[ 1 + \Gamma \left( u_{z,x+}^{n+1} \frac{\Delta t^n}{\Delta x} + u_{z,y+}^{n+1} \frac{\Delta t^n}{\Delta y} - u_{z,x-}^{n+1} \frac{\Delta t^n}{\Delta x} - u_{z,y-}^{n+1} \frac{\Delta t^n}{\Delta y} + \frac{\Delta t^n}{\Gamma} \right) \right] \\ a_{i,j}^{1,0} &= \Gamma u_{z,x+}^{n+1} \frac{\Delta t^n}{\Delta x} \\ a_{i,j}^{0,1} &= \Gamma u_{z,y+}^{n+1} \frac{\Delta t^n}{\Delta y} \\ a_{i,j}^{-1,0} &= \Gamma u_{z,x-}^{n+1} \frac{\Delta t^n}{\Delta x} \\ a_{i,j}^{0,-1} &= \Gamma u_{z,y-}^{n+1} \frac{\Delta t^n}{\Delta y} \end{aligned} \quad (\text{B.13})$$

3160 and the explicit right-hand side as:



$$\begin{aligned}
 y_{i,j,k}^n = & \left[ 1 - (1 - \Gamma) \left( u_{z,x+} \frac{\Delta t^n}{\Delta x} + u_{z,y+} \frac{\Delta t^n}{\Delta y} - u_{z,x-} \frac{\Delta t^n}{\Delta x} - u_{z,y-} \frac{\Delta t^n}{\Delta y} + \frac{\Delta t^n}{\Gamma} \right) \right] c_{i,j,k}^n \\
 & + (1 - \Gamma) \left( u_{z,x+} \frac{\Delta t^n}{\Delta x} c_{i-1,j,k}^n + u_{z,y+} \frac{\Delta t^n}{\Delta y} c_{i,j-1,k}^n - u_{z,x-} \frac{\Delta t^n}{\Delta x} c_{i+1,j,k}^n - u_{z,y-} \frac{\Delta t^n}{\Delta y} c_{i,j+1,k}^n \right) \\
 & + \Gamma \hat{w}_{i,j,k}^{n+1} \cdot c_{\text{sat},i,j,k}^{n+1} \frac{\Delta t^n}{\Gamma} + (1 - \Gamma) \hat{w}_{i,j,k}^n \cdot c_{\text{sat},i,j,k}^n \frac{\Delta t^n}{\Gamma} \quad (\text{B.14})
 \end{aligned}$$

3161 The offshore boundary is defined to be zero-flux, the onshore boundary has a constant  
3162 transport gradient and the lateral boundaries are circular:

$$\begin{aligned}
 c_{1,j,k}^{n+1} &= 0 \\
 c_{n_x+1,j,k}^{n+1} &= 2c_{n_x,j,k}^{n+1} - c_{n_x-1,j,k}^{n+1} \\
 c_{i,1,k}^{n+1} &= c_{i,n_y+1,k}^{n+1} \\
 c_{i,n_y+1,k}^{n+1} &= c_{i,1,k}^{n+1}
 \end{aligned} \quad (\text{B.15})$$

3163 These boundary conditions can be combined with Equation [B.12](#), [B.13](#) and [B.14](#) into a  
3164 linear system of equations:

$$\left[ \begin{array}{cccccc} A_1^0 & A_1^1 & \mathbf{0} & \cdots & \mathbf{0} & A_1^{n_y+1} \\ A_2^{-1} & A_2^0 & \ddots & \ddots & & \mathbf{0} \\ \mathbf{0} & \ddots & \ddots & \ddots & & \vdots \\ \vdots & \ddots & \ddots & \ddots & & \mathbf{0} \\ \mathbf{0} & \ddots & \ddots & & A_{n_y}^0 & A_{n_y}^1 \\ A_{n_y+1}^{-n_y-1} & \mathbf{0} & \cdots & \mathbf{0} & A_{n_y+1}^{-1} & A_{n_y+1}^0 \end{array} \right] \left[ \begin{array}{c} \vec{c}_1 \\ \vec{c}_2 \\ \vdots \\ \vdots \\ \vec{c}_{n_y} \\ \vec{c}_{n_y+1} \end{array} \right] = \left[ \begin{array}{c} \vec{y}_1 \\ \vec{y}_2 \\ \vdots \\ \vdots \\ \vec{y}_{n_y} \\ \vec{y}_{n_y+1} \end{array} \right] \quad (\text{B.16})$$

3165 where each item in the matrix is again a matrix  $A_j^l$  and each item in the vectors is  
3166 again a vector  $\vec{c}_j$  and  $\vec{y}_j$  respectively. The form of the matrix  $A_j^l$  depends on the  
3167 diagonal index  $l$  and reads:

$$A_j^0 = \left[ \begin{array}{ccccccc} 0 & 0 & 0 & 0 & \cdots & \cdots & 0 \\ a_{2,j}^{0,-1} & a_{2,j}^{0,0} & a_{2,j}^{0,1} & \ddots & & & \vdots \\ 0 & a_{3,j}^{0,-1} & a_{3,j}^{0,0} & a_{3,j}^{0,1} & \ddots & & \vdots \\ \vdots & \ddots & \ddots & \ddots & \ddots & \ddots & \vdots \\ \vdots & & \ddots & a_{n_x-1,j}^{0,-1} & a_{n_x-1,j}^{0,0} & a_{n_x-1,j}^{0,1} & 0 \\ \vdots & & & 0 & a_{n_x,j}^{0,-1} & a_{n_x,j}^{0,0} & a_{n_x,j}^{0,1} \\ 0 & \cdots & \cdots & 0 & 1 & -2 & 1 \end{array} \right] \quad (\text{B.17})$$

3168 for  $l = 0$  and

$$A_j^l = \begin{bmatrix} 1 & 0 & \cdots & \cdots & \cdots & \cdots & 0 \\ 0 & a_{2,j}^{l,0} & \ddots & & & & \vdots \\ \vdots & \ddots & a_{3,j}^{l,0} & \ddots & & & \vdots \\ \vdots & & \ddots & \ddots & \ddots & & \vdots \\ \vdots & & & \ddots & a_{n_x-1,j}^{l,0} & \ddots & \vdots \\ \vdots & & & & \ddots & a_{n_x,j}^{l,0} & 0 \\ 0 & \cdots & \cdots & \cdots & \cdots & 0 & 1 \end{bmatrix} \quad (B.18)$$

for  $l \neq 0$ . The vectors  $\vec{c}_{j,k}$  and  $\vec{y}_{j,k}$  read:

$$\vec{c}_{j,k} = \begin{bmatrix} c_{1,j,k}^{n+1} \\ c_{2,j,k}^{n+1} \\ c_{3,j,k}^{n+1} \\ \vdots \\ c_{n_x-1,j,k}^{n+1} \\ c_{n_x,j,k}^{n+1} \\ c_{n_x+1,j,k}^{n+1} \end{bmatrix} \quad \text{and} \quad \vec{y}_{j,k} = \begin{bmatrix} 0 \\ y_{2,j,k}^n \\ y_{3,j,k}^n \\ \vdots \\ y_{n_x-1,j,k}^n \\ y_{n_x,j,k}^n \\ 0 \end{bmatrix} \quad (B.19)$$

$n_x$  and  $n_y$  denote the number of spatial grid cells in x- and y-direction.

## 3171 B.2 IMPLICIT SOLVER

3172 The linear system defined in Equation B.16 is solved by a sparse matrix solver for each  
 3173 sediment fraction separately in ascending order of grain size. Initially, the weights  
 3174  $\hat{w}_{i,j,k}^{n+1}$  are chosen according to the grain size distribution in the bed and the air fol-  
 3175 lowing Equation 4.10b. The sediment availability constraint based on Equation 4.9 is  
 3176 checked after each solve:

$$m_{a,k} \geq \frac{\hat{w}_{i,j,k}^{n+1} c_{sat,i,j,k}^{n+1} - c_{i,j,k}^{n+1}}{\Delta t^n} \quad (B.20)$$

3177 If the constraint is violated, a new estimate for the weights is back-calculated follow-  
 3178 ing:

$$\hat{w}_{i,j,k}^{n+1} = \frac{c_{i,j,k}^{n+1} + m_{a,k} \frac{\Delta t^n}{\Gamma}}{c_{sat,i,j,k}^{n+1}} \quad (B.21)$$

3179 The system is solved again using the new weights. This procedure is repeated until  
 3180 a weight is found that does not violate the sediment availability constraint. If the  
 3181 time step is not too large, the procedure typically converges in only a few iterations.  
 3182 Finally, the weights of the larger grains are increased proportionally as to ensure that  
 3183 the sum of all weights remains unity. If no larger grains are defined, not enough  
 3184 sediment is available for transport and the grid cell is truly availability-limited. This

3185 situation should only occur occasionally as the weights in the next time step are com-  
 3186 puted based on the new bed composition and thus will be skewed towards the large  
 3187 fractions. If the situation occurs regularly, the time step is chosen too large compared  
 3188 to the rate of armoring.

3189 **B.3 SHEAR VELOCITY THRESHOLD**

3190 The shear velocity threshold represents the influence of bed surface properties in the  
 3191 saturated sediment transport equation (Equation 4.8). The shear velocity threshold  
 3192 is computed for each grid cell and sediment fraction separately based on local bed  
 3193 surface properties, like moisture, roughness elements and salt content. For each bed  
 3194 surface property supported by the model a factor is computed to increase the initial  
 3195 shear velocity threshold:

$$u_{*th} = f_{u_{*th},M} \cdot f_{u_{*th},R} \cdot f_{u_{*th},S} \cdot u_{*th,o} \quad (\text{B.22})$$

3196 The initial shear velocity threshold  $u_{*th,o}$  [m/s] is computed based on the grain size  
 3197 following [Bagnold \(1937a\)](#):

$$u_{*th,o} = A \sqrt{\frac{\rho_p - \rho_a}{\rho_a}} \cdot g \cdot d_n \quad (\text{B.23})$$

3198 where  $A$  [-] is an empirical constant,  $\rho_p$  [kg/m<sup>3</sup>] is the grain density,  $\rho_a$  [kg/m<sup>3</sup>] is the  
 3199 air density,  $g$  [m/s<sup>2</sup>] is the gravitational constant and  $d_n$  [m] is the nominal grain size  
 3200 of the sediment fraction.

3201 **B.3.1 Moisture content**

3202 The shear velocity threshold is updated based on moisture content following [Belly](#)  
 3203 ([1964](#)):

$$f_{u_{*th},M} = \max(1 ; 1.8 + 0.6 \cdot \log(p_g)) \quad (\text{B.24})$$

3204 where  $f_{u_{*th},M}$  [-] is a factor in Equation B.22,  $p_g$  [-] is the geotechnical mass content of  
 3205 water, which is the percentage of water compared to the dry mass. The geotechnical  
 3206 mass content relates to the volumetric water content  $p_V$  [-] according to:

$$p_g = \frac{p_V \cdot \rho_w}{\rho_p \cdot (1 - p)} \quad (\text{B.25})$$

3207 where  $\rho_w$  [kg/m<sup>3</sup>] and  $\rho_p$  [kg/m<sup>3</sup>] are the water and particle density respectively and  
 3208  $p$  [-] is the porosity. Values for  $p_g$  smaller than 0.005 do not affect the shear velocity  
 3209 threshold ([Pye and Tsoar, 1990](#)). Values larger than 0.064 (or 10% volumetric content)  
 3210 cease transport ([Delgado-Fernandez, 2010](#)), which is implemented as an infinite shear  
 3211 velocity threshold.

3212 Exploratory model runs of the unsaturated soil with the HYDRUS1D ([Šimůnek](#)  
 3213 [et al., 1998](#)) hydrology model show that the increase of the volumetric water content  
 3214 to saturation is almost instantaneous with rising tide. The drying of the beach surface  
 3215 through infiltration shows an exponential decay. In order to capture this behavior the  
 3216 volumetric water content is implemented according to:

$$p_V^{n+1} = \begin{cases} p & \text{if } \eta > z_b \\ p_V^n \cdot e^{\frac{\log(0.5)}{T_{dry}} \cdot \Delta t^n} - E_v \cdot \frac{\Delta t^n}{\Delta z} & \text{if } \eta \leq z_b \end{cases} \quad (\text{B.26})$$

3217 where  $\eta$  [m+MSL] is the instantaneous water level,  $z_b$  [m+MSL] is the local bed elevation  
 3218  $p_V^n$  [-] is the volumetric water content in time step  $n$ ,  $\Delta t^n$  [s] is the model time  
 3219 step and  $\Delta z$  is the bed composition layer thickness.  $T_{dry}$  [s] is the beach drying time  
 3220 scale, defined as the time in which the beach moisture content halves.  $E_v$  [m/s] is  
 3221 the evaporation rate that is implemented through an adapted version of the Penman  
 3222 equation (Shuttleworth, 1993):

$$E_v = \frac{m_v \cdot R_n + 6.43 \cdot \gamma_v \cdot (1 + 0.536 \cdot u_2) \cdot \delta e}{\lambda_v \cdot (m_v + \gamma_v)} \cdot 9 \cdot 10^7 \quad (\text{B.27})$$

3223 where  $m_v$  [kPa/K] is the slope of the saturation vapor pressure curve,  $R_n$   
 3224 [MJ/m<sup>2</sup>/day] is the net radiance,  $\gamma_v$  [kPa/K] is the psychrometric constant,  $u_2$  [m/s]  
 3225 is the wind speed at 2 m above the bed,  $\delta e$  [kPa] is the vapor pressure deficit (related  
 3226 to the relative humidity) and  $\lambda_v$  [MJ/kg] is the latent heat vaporization. To obtain an  
 3227 evaporation rate in [m/s], the original formulation is multiplied by  $9 \cdot 10^7$ .

### 3228 B.3.2 Roughness elements

3229 The shear velocity threshold is updated based on the presence of roughness elements  
 3230 following Raupach et al. (1993):

$$f_{u_{th,R}} = \sqrt{(1 - m \cdot \sum_{k=k_0}^{n_k} \hat{w}_k^{\text{bed}})(1 + \frac{m\beta}{\sigma} \cdot \sum_{k=k_0}^{n_k} \hat{w}_k^{\text{bed}})} \quad (\text{B.28})$$

3231 by assuming:

$$\lambda = \frac{\sum_{k=k_0}^{n_k} \hat{w}_k^{\text{bed}}}{\sigma} \quad (\text{B.29})$$

3232 where  $f_{u_{th,R}}$  [-] is a factor in Equation B.22,  $k_0$  is the sediment fraction index of the  
 3233 smallest non-erodible fraction in current conditions and  $n_k$  is the number of sediment  
 3234 fractions defined. The implementation is discussed in detail in section 4.4.4.

### 3235 B.3.3 Salt content

3236 The shear velocity threshold is updated based on salt content following Nickling and  
 3237 Ecclestone (1981):

$$f_{u_{th,S}} = 1.03 \cdot \exp(0.1027 \cdot p_s) \quad (\text{B.30})$$

3238 where  $f_{u_{th,S}}$  [-] is a factor in Equation B.22 and  $p_s$  [-] is the salt content [mg/g].  
 3239 Currently, no model is implemented that predicts the instantaneous salt content. The  
 3240 spatial varying salt content needs to be specified by the user, for example through the  
 3241 BMI interface.

3242 B.3.4 Masks

3243 To account for spatial differences in hydrodynamics without the necessity to run a sep-  
 3244 arate hydrodynamic model, the model supports hydrodynamic masks. Without such  
 3245 mask the model imposes the still water levels and offshore wave heights uniformly  
 3246 to all grid cells where the bed level is below the instantaneous water level. The tidal  
 3247 range and mean water level are therefore uniform throughout the model domain. In  
 3248 addition, the still water level underestimates the local water level as wave runup is  
 3249 not taken into account. Only wave heights are maximized by a constant and uniform  
 3250 ratio between wave height and water depth (Equation 4.15).

3251 For cases where the assumption of uniform hydrodynamics hydrodynamics, the  
 3252 uniformly imposed instantaneous still water level  $\eta$  [m+MSL] and offshore wave  
 3253 height  $H$  [m] can be converted to a local water level  $\hat{\eta}$  [m+MSL] and wave height  
 3254  $\hat{H}$  [m] using a hydrodynamic mask, following:

$$\begin{aligned}\hat{H} &= H \cdot K^x \\ \hat{\eta} &= \eta \cdot K^x + K^+ + R\end{aligned}\quad (\text{B.31})$$

3255 where  $K$  is the hydrodynamic mask, consisting of a multiplication mask ( $K^x$  [-]) and  
 3256 an addition mask ( $K^+$  [m]). The multiplication mask can be used to reduce the tidal  
 3257 range and the addition mask can subsequently be used to elevate the mean water  
 3258 level. The hydrodynamic mask is applied before the wave height is maximized by the  
 3259 maximum ratio between wave height and water depth (Equation 4.15).  $R$  [m] is an  
 3260 estimate for the wave runup height following Battjes (1974):

$$\frac{R}{H} = \xi \quad (\text{B.32})$$

3261 where  $\xi$  [-] is the surf similarity parameter with a value between 1.0 and 2.3.

3262 B.4 BASIC MODEL INTERFACE (BMI)

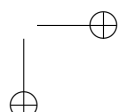
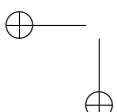
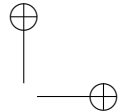
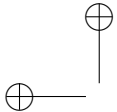
3263 A Basic Model Interface (BMI, Peckham et al., 2013) is implemented that allows inter-  
 3264 action with the model during run time. The model can be implemented as a library  
 3265 within a larger framework as the interface exposes the initialization, finalization and  
 3266 time stepping routines. As a convenience functionality the current implementation  
 3267 supports the specification of a callback function. The callback function is called at the  
 3268 start of each time step and can be used to exchange data with the model, e.g. update  
 3269 the topography from measurements.

3270 An example of a callback function, that is referenced in the model input file or  
 3271 through the model command-line options as "callback.py:update", is:

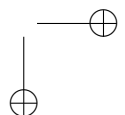
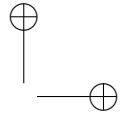
callback.py

```
3272 import numpy as np
3273
3274 def update(model):
3275     val = model.get_var('zb')
3276     val_new = val.copy()
3277     val_new[:, :] = np.loadtxt('measured_topography.txt')
```

327 | model.set\_var('zb', val\_new)



"thesis" — 2016/11/15 — 10:57 — page 116 — #146



# C

3281

3282

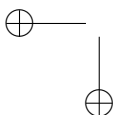
---

## 3283 MODEL SETTINGS

---

3284 Unless stated otherwise, the model schematizations presented in chapter 5 used the  
3285 settings listed below. Some model settings belong to experimental features of the  
3286 model and are not discussed in this thesis. These settings are listed for complete-  
3287 ness only and marked with an asterisk (\*). The model settings are chosen such that  
3288 experimental features are disabled.

Parameter	Value
A	0.085
CFL	1.0
Cb	1.5
T	1.0
Tdry	5400.0
Tsalt*	0.0
accfac	1.0
bedupdate	False
beta	130.0
bi	0.05
boundary_lateral	circular
boundary_offshore	noflux
boundary_onshore	gradient
callback	None
cpair	0.0010035
csalt*	0.035
dt	3600.0
eps	0.001
evaporation	True
facDOD	0.1
g	9.81
gamma	0.5
grain_dist	0.005709 0.234708 0.608887 0.099666 0.001029 0.000001 0.010486 0.028503 0.010486 0.000522 0.000004
grain_size	0.000177 0.000250 0.000354 0.000500 0.000707 0.001000 0.002000 0.004000 0.008000 0.016000 0.032000
k	0.01
layer_thickness	0.01
m	0.5



Parameter	Value	(continued)
max_error	0.000001	
max_iter	1000	
method_moist	belly_johnson	
method_transport	bagnold	
mixtoplayer	True	
nfractions	11	
nlayers	10	
output_times	604800.0	
porosity	0.4	
restart	None	
rhoa	1.25	
rhop	2650.0	
rhow	1025.0	
runup	False	
scheme	euler_backward	
sigma	11.9	
th_bedslope	False	
th_grainsize	True	
th_humidity*	False	
th_moisture	True	
th_roughness	True	
th_salt*	False	
tstart	0.0	
tstop	126230400.0	
z	10.0	

---

3289 BIBLIOGRAPHY

---

- 3290 Aagaard, T. (2014). Sediment supply to beaches: Cross-shore sand transport on the  
3291 lower shoreface. *Journal of Geophysical Research*, 119(4):913–926. 2013JF003041.
- 3292 Aagaard, T., Davidson-Arnott, R., Greenwood, B., and Nielsen, J. (2004). Sediment  
3293 supply from shoreface to dunes: linking sediment transport measurements and  
3294 long-term morphological evolution. *Geomorphology*, 60(1):205–224.
- 3295 Anthony, E. J. (2013). Storms, shoreface morphodynamics, sand supply, and the accre-  
3296 tion and erosion of coastal dune barriers in the southern north sea. *Geomorphology*,  
3297 199:8–21.
- 3298 Arens, S., Van Boxel, J., and Abuodha, J. (2002). Changes in grain size of sand in  
3299 transport over a foredune. *Earth Surface Processes and Landforms*, 27(11):1163–1175.
- 3300 Arens, S. M. (1996). Patterns of sand transport on vegetated foredunes. *Geomorphology*,  
3301 17:339–350.
- 3302 Bagnold, R. (1935). The movement of desert sand. *Geographical Journal*, pages 342–365.
- 3303 Bagnold, R. (1937a). The size-grading of sand by wind. *Proceedings of the Royal Society  
3304 of London. Series A, Mathematical and Physical Sciences*, pages 250–264.
- 3305 Bagnold, R. (1937b). The transport of sand by wind. *Geographical journal*, pages 409–  
3306 438.
- 3307 Barchyn, T. E., Hugenholtz, C. H., Li, B., McKenna Neuman, C., and Sanderson, S.  
3308 (2014a). From particle counts to flux: Wind tunnel testing and calibration of the  
3309 "wenglor" aeolian sediment transport sensor. *Aeolian Research*, 15:311–318.
- 3310 Barchyn, T. E., Martin, R. L., Kok, J. F., and Hugenholtz, C. H. (2014b). Fundamen-  
3311 tal mismatches between measurements and models in aeolian sediment transport  
3312 prediction: The role of small-scale variability. *Aeolian Research*, 15:245–251.
- 3313 Battjes, J. A. (1974). *Computation of set-up, longshore currents, run-up and overtopping due  
3314 to wind-generated waves*. PhD thesis, TU Delft, Delft University of Technology.
- 3315 Bauer, B. O. and Davidson-Arnott, R. G. D. (2002). A general framework for modeling  
3316 sediment supply to coastal dunes including wind angle, beach geometry, and fetch  
3317 effects. *Geomorphology*, 49:89–108.
- 3318 Bauer, B. O., Davidson-Arnott, R. G. D., Hesp, P. A., Namikas, S. L., Ollerhead, J., and  
3319 Walker, I. J. (2009). Aeolian sediment transport on a beach: Surface moisture, wind  
3320 fetch, and mean transport. *Geomorphology*, 105:106–116.
- 3321 Belly, P. Y. (1964). Sand movement by wind. Technical Report 1, U.S. Army Corps of  
3322 Engineers CERC, Vicksburg, MS. 38 pp.

- 3323 Borsje, B. W., van Wesenbeeck, B. K., Dekker, F., Paalvast, P., Bouma, T. J., van Katwijk,  
3324 M. M., and de Vries, M. B. (2011). How ecological engineering can serve in coastal  
3325 protection. *Ecological Engineering*, 37(2):113–122.
- 3326 Buscombe, D., Rubin, D. M., and Warrick, J. A. (2010). A universal approximation  
3327 of grain size from images of noncohesive sediment. *Journal of Geophysical Research*,  
3328 115(F2). F02015.
- 3329 Cheng, H., Liu, C., Zou, X., Li, J., He, J., Liu, B., Wu, Y., Kang, L., and Fang, Y. (2015).  
3330 Aeolian creeping mass of different grain sizes over sand beds of varying length.  
3331 *Journal of Geophysical Research*. 2014JF003367.
- 3332 Darke, I. and McKenna Neuman, C. (2008). Field study of beach water content as a  
3333 guide to wind erosion potential. *Journal of Coastal Research*, 24(5):1200–1208.
- 3334 Davidson-Arnott, R. G. and Law, M. N. (1990). *Seasonal patterns and controls on sediment*  
3335 *supply to coastal foredunes, Long Point, Lake Erie*, pages 177–200. Wiley Chichester.
- 3336 Davidson-Arnott, R. G., White, D. C., and Ollerhead, J. (1997). The effects of artificial  
3337 pebble concentrations on eolian sand transport on a beach. *Canadian Journal of Earth*  
3338 *Sciences*, 34(11):1499–1508.
- 3339 Davidson-Arnott, R. G. D. and Bauer, B. O. (2009). Aeolian sediment transport on  
3340 a beach: Thresholds, intermittency, and high frequency variability. *Geomorphology*,  
3341 105:117–126.
- 3342 Davidson-Arnott, R. G. D., MacQuarrie, K., and Aagaard, T. (2005). The effect of wind  
3343 gusts, moisture content and fetch length on sand transport on a beach. *Geomorphology*,  
3344 68:115–129.
- 3345 Davidson-Arnott, R. G. D., Yang, Y., Ollerhead, J., Hesp, P. A., and Walker, I. J. (2008).  
3346 The effects of surface moisture on aeolian sediment transport threshold and mass  
3347 flux on a beach. *Earth Surface Processes and Landforms*, 33(1):55–74.
- 3348 De Schipper, M., De Vries, S., Ranasinghe, R., Reniers, A., and Stive, M. (2013). Along-  
3349 shore topographic variability at a nourished beach. In *Coastal Dynamics 2013: 7th*  
3350 *International Conference on Coastal Dynamics, Arcachon, France, 24–28 June 2013*. Bor-  
3351 deauve University.
- 3352 de Schipper, M. A., de Vries, S., Ruessink, G., de Zeeuw, R. C., Rutten, J., van Gelder-  
3353 Maas, C., and Stive, M. J. (2016). Initial spreading of a mega feeder nourishment:  
3354 Observations of the sand engine pilot project. *Coastal Engineering*, 111:23–38.
- 3355 de Vriend, H. J., van Koningsveld, M., Aarninkhof, S. G., de Vries, M. B., and Bap-  
3356 tist, M. J. (2015). Sustainable hydraulic engineering through building with nature.  
3357 *Journal of Hydro-environment Research*, 9(2):159–171.
- 3358 de Vries, S., Arens, S. M., de Schipper, M. A., and Ranasinghe, R. (2014a). Aeolian  
3359 sediment transport on a beach with a varying sediment supply. *Aeolian Research*,  
3360 15:235–244.

- 3361 de Vries, S., Radermacher, M., de Schipper, M., and Stive, M. (2015). Tidal dynamics  
3362 in the sand motor lagoon. In *E-proceedings of the 36th IAHR World Congress*.
- 3363 de Vries, S., van Thiel de Vries, J. S. M., van Rijn, L. C., Arens, S. M., and Ranasinghe,  
3364 R. (2014b). Aeolian sediment transport in supply limited situations. *Aeolian Research*,  
3365 12:75–85.
- 3366 Delft3D-FLOW Manual (2014). *Delft3D - 3D/2D modelling suite for integral water solu-*  
3367 *tions - Hydro-Morphodynamics*. Deltares, Delft. Version 3.15.34158.
- 3368 Delgado-Fernandez, I. (2010). A review of the application of the fetch effect to mod-  
3369 elling sand supply to coastal foredunes. *Aeolian Research*, 2:61–70.
- 3370 Delgado-Fernandez, I., Davidson-Arnott, R., Bauer, B. O., Walker, I. J., Ollerhead, J.,  
3371 and Rhew, H. (2012). Assessing aeolian beach-surface dynamics using a remote  
3372 sensing approach. *Earth Surface Processes and Landforms*, 37(15):1651–1660.
- 3373 Delgado-Fernandez, I. and Davidson-Arnott, R. A. (2011). Meso-scale aeolian sedi-  
3374 ment input to coastal dunes: The nature of aeolian transport events. *Geomorphology*,  
3375 126(1):217–232.
- 3376 Donchyts, G., Baart, F., Winsemius, H., Gorelick, N., Kwadijk, J., and van de Giesen, N.  
3377 (2016). Earth's surface water change over the past 30 years. *Nature Climate Change*,  
3378 6(9):810–813.
- 3379 Dong, Z., Wang, H., Liu, X., and Wang, X. (2004a). The blown sand flux over a sandy  
3380 surface: a wind tunnel investigation on the fetch effect. *Geomorphology*, 57:117–127.
- 3381 Dong, Z., Wang, H., Liu, X., and Wang, X. (2004b). A wind tunnel investigation of the  
3382 influences of fetch length on the flux profile of a sand cloud blowing over a gravel  
3383 surface. *Earth Surface Processes and Landforms*, 29(13):1613–1626.
- 3384 Dupont, S., Bergametti, G., and Simoëns, S. (2014). Modeling aeolian erosion in pres-  
3385 ence of vegetation. *Journal of Geophysical Research*, 119(2):168–187.
- 3386 Dyer, K. R. (1986). *Coastal and estuarine sediment dynamics*. Wiley, Chichester.
- 3387 Dymin (1954). quoted by Greeley and Iversen (1985).
- 3388 Edwards, B. L. and Namikas, S. L. (2009). Small-scale variability in surface moisture  
3389 on a fine-grained beach: implications for modeling aeolian transport. *Earth Surface  
3390 Processes and Landforms*, 34:1333–1338.
- 3391 Edwards, B. L., Namikas, S. L., and D'Sa, E. J. (2013). Simple infrared techniques for  
3392 measuring beach surface moisture. *Earth Surface Processes and Landforms*, 38(2):192–  
3393 197.
- 3394 Gallagher, E. L., MacMahan, J., Reniers, A., Brown, J., and Thornton, E. B. (2011).  
3395 Grain size variability on a rip-channelled beach. *Marine Geology*, 287(1):43–53.
- 3396 Gillette, D. A. and Stockton, P. H. (1989). The effect of nonerodible particles on  
3397 wind erosion of erodible surfaces. *Journal of Geophysical Research: Atmospheres*,  
3398 94(D10):12885–12893.

- 3399 Gillies, J. A., Nickling, W. G., and King, J. (2006). Aeolian sediment transport through  
3400 large patches of roughness in the atmospheric inertial sublayer. *Journal of Geophysical  
3401 Research: Earth Surface*, 111(F2). F02006.
- 3402 Grunnet, N. M. and Ruessink, B. (2005). Morphodynamic response of nearshore bars  
3403 to a shoreface nourishment. *Coastal Engineering*, 52(2):119–137.
- 3404 Hamm, L., Capobianco, M., Dette, H., Lechuga, A., Spanhoff, R., and Stive, M. (2002).  
3405 A summary of european experience with shore nourishment. *Coastal engineering*,  
3406 47(2):237–264.
- 3407 Hesp, P. A. and Smyth, T. A. G. (2016). Surfzone-beach-dune interactions: Flow and  
3408 sediment transport across the intertidal beach and backshore. *Journal of Coastal  
3409 Research*, SI 75:8–12.
- 3410 Hoonhout, B. M. (2013). Monitoring the process of aeolian transport. In *Proceedings of  
3411 the NCK-days 2013*.
- 3412 Hoonhout, B. M. (2016a). Aeolis model setups v2.0. GIT repository.
- 3413 Hoonhout, B. M. (2016b). Aeolis v1.1: A process-based model for simulating  
3414 availability-limited aeolian sediment transport. GIT repository.
- 3415 Hoonhout, B. M., Baart, F., and Van Thiel de Vries, J. S. M. (2014a). Intertidal beach  
3416 classification in infrared images. *Journal of Coastal Research*, SI 66:657–662.
- 3417 Hoonhout, B. M., Cohn, N., de Vries, S., Roelvink, J. A., Ruggiero, P., Moore, L. J.,  
3418 Durán, O., and Goldstein, E. (2016a). How tides and waves enhance aeolian sedi-  
3419 ment transport at the sand motor. In *Proceedings of the 35th International Conference  
3420 on Coastal Engineering*.
- 3421 Hoonhout, B. M., Cohn, N., de Vries, S., Roelvink, J. A., Ruggiero, P., Moore, L. J.,  
3422 Durán, O., and Goldstein, E. (2016b). How tides and waves enhance aeolian sedi-  
3423 ment transport at the sand motor. In *Proceedings of the Ocean Sciences Meeting 2016*.
- 3424 Hoonhout, B. M. and de Vries, S. (2014a). Modelling and monitoring of meso-scale  
3425 supply-limited aeolian transport. In *Proceedings of the NCK-days 2014*.
- 3426 Hoonhout, B. M. and de Vries, S. (2014b). Process-based modeling of supply-limited  
3427 aeolian transport in coastal environments. In *Proceedings of the International Confer-  
3428 ence on Aeolian Research 2014*.
- 3429 Hoonhout, B. M. and de Vries, S. (2016a). Aeolian sediment supply at a mega nour-  
3430 ishment. *Coastal Engineering*. Submitted.
- 3431 Hoonhout, B. M. and de Vries, S. (2016b). Aeolis: A new model for aeolian sediment  
3432 supply and transport. In *Proceedings of the NCK-days 2016*.
- 3433 Hoonhout, B. M. and de Vries, S. (2016c). Field measurements on spatial variations in  
3434 aeolian sediment availability at the sand motor mega nourishment. *Aeolian Research*.  
3435 Submitted.

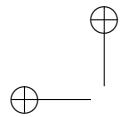
- 3436 Hoonhout, B. M. and de Vries, S. (2016d). A process-based model for aeolian sediment  
3437 transport and spatiotemporal varying sediment availability. *Journal of Geophysical*  
3438 *Research: Earth Surface*. 2015JF003692.
- 3439 Hoonhout, B. M., de Vries, S., Baart, F., van Thiel de Vries, J. S. M., van der Weerd,  
3440 L., and Wijnberg, K. M. (2013). Monitoring of beach surface properties with remote  
3441 sensing. In *Proceedings of Coastal Dynamics*, Arcachon, France.
- 3442 Hoonhout, B. M., de Vries, S., and Cohn, N. (2015a). The influence of spatially varying  
3443 supply on coastal aeolian transport: a field experiment. In *Proceedings of Coastal*  
3444 *Sediments*, San Diego, USA.
- 3445 Hoonhout, B. M., de Vries, S., and Cohn, N. (2015b). The influence of spatially varying  
3446 supply on coastal aeolian transport: A field experiment. In *Proceedings of the NCK-*  
3447 *days 2015*.
- 3448 Hoonhout, B. M., de Vries, S., and Cohn, N. (2016c). Field measurements on aeolian  
3449 sediment transport at the sand motor mega nourishment during the megapex field  
3450 campaign. OpenDAP server.
- 3451 Hoonhout, B. M. and den Heijer, C. (2010). Reliability of dune erosion assessment  
3452 along curved coastlines. In *Proceedings of the 32nd International Conference on Coastal*  
3453 *Engineering*, Shanghai, China.
- 3454 Hoonhout, B. M. and Radermacher, M. (2015a). Annotated images of the dutch coast.  
3455 FTP server.
- 3456 Hoonhout, B. M. and Radermacher, M. (2015b). Flamingo: a coastal image analysis  
3457 toolbox. GIT repository.
- 3458 Hoonhout, B. M., Radermacher, M., Baart, F., and Van der Maaten, L. J. P. (2015c). An  
3459 automated method for semantic classification of regions in coastal images. *Coastal*  
3460 *Engineering*, 105:1–12.
- 3461 Hoonhout, B. M. and van Thiel de Vries, J. S. M. (2012). Modeling dune erosion,  
3462 overwash and inundation of barrier islands. In *Proceedings of the 33rd International*  
3463 *Conference on Coastal Engineering*, Santander, Spain.
- 3464 Hoonhout, B. M., van Thiel de Vries, J. S. M., Curto, V., and Stive, M. J. F. (2014b).  
3465 Monitoring supply limiting conditions using imageing techniques. In *Proceedings of*  
3466 *the 34th International Conference on Coastal Engineering*.
- 3467 Horikawa, K., Hotta, S., Kubota, S., and Katori, S. (1983). On the sand transport rate  
3468 by wind on a beach. *Coastal Engineering in Japan*, 26:101–120.
- 3469 Hotta, S., Kubota, S., Katori, S., and Horikawa, K. (1984). Sand transport by wind on  
3470 a wet sand beach. In *Proceedings of the 19th Conference on Coastal Engineering*, pages  
3471 1264–1281, Houston, TX. ASCE.
- 3472 Houser, C. (2009). Synchronization of transport and supply in beach-dune interaction.  
3473 *Progress in Physical Geography*, 33(6):733–746.

- 3474 Howard, A. D. (1977). Effect of slope on the threshold of motion and its application  
3475 to orientation of wind ripples. *Geological Society of America Bulletin*, 88(6):853–856.
- 3476 Hsu, S.-A. (1971). Wind stress criteria in eolian sand transport. *Journal of Geophysical*  
3477 *Research*, 76(36):8684–8686.
- 3478 Iversen, J. D. and Rasmussen, K. R. (2006). The effect of surface slope on saltation  
3479 threshold. *Sedimentology*, 41(4):721–728.
- 3480 Jackson, D. W. T. and Cooper, J. A. G. (1999). Beach fetch distance and aeolian sedi-  
3481 ment transport. *Sedimentology*, 46:517–522.
- 3482 Jackson, N. L. and Nordstrom, K. F. (1998). Aeolian transport of sediment on a beach  
3483 during and after rainfall, wildwood, nj, usa. *Geomorphology*, 22(2):151–157.
- 3484 Jackson, N. L. and Nordstrom, K. F. (2011). Aeolian sediment transport and landforms  
3485 in managed coastal systems: a review. *Aeolian research*, 3(2):181–196.
- 3486 Jackson, N. L., Nordstrom, K. F., Saini, S., and Smith, D. R. (2010). Effects of nour-  
3487 ishment on the form and function of an estuarine beach. *Ecological Engineering*,  
3488 36(12):1709–1718.
- 3489 Johnson, J. W. (1965). Sand movement on coastal dunes. Technical Report 570, Symp.  
3490 3, Paper no. 75, U.S. Department of Agriculture, Washington. pp 747–755.
- 3491 Kawamura, R. (1951). Study of sand movement by wind. Technical Report HEL-2-8,  
3492 Hydraulics Engineering Laboratory, Univeristy of California, Berkeley.
- 3493 King, C. A. M. (1951). Depth of disturbance of sand on sea beaches by waves. *Journal*  
3494 *of Sedimentary Petrology*, 21(3):131–140.
- 3495 King, J., Nickling, W. G., and Gillies, J. A. (2005). Representation of vegetation and  
3496 other nonerodible elements in aeolian shear stress partitioning models for predict-  
3497 ing transport threshold. *Journal of Geophysical Research*, 110(F4). F04015.
- 3498 Kocurek, G. and Lancaster, N. (1999). Aeolian system sediment state: theory and  
3499 mojave desert kelso dune field example. *Sedimentology*, 46(3):505–515.
- 3500 Kroy, K., Sauermann, G., and Herrmann, H. J. (2002). Minimal model for sand dunes.  
3501 *Physical Review Letters*, 88(5):054301.
- 3502 Lancaster, N. and Baas, A. (1998). Influence of vegetation cover on sand transport by  
3503 wind: field studies at owens lake, california. *Earth Surface Processes and Landforms*,  
3504 23(1):69–82.
- 3505 Lettau, K. and Lettau, H. (1978). Experimental and micrometeorological field studies  
3506 of dune migration.
- 3507 Li, J., Okin, G. S., Herrick, J. E., Belnap, J., Miller, M. E., Vest, K., and Draut, A. E.  
3508 (2013). Evaluation of a new model of aeolian transport in the presence of vegetation.  
3509 *Journal of Geophysical Research*, 118(1):288–306.

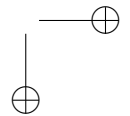
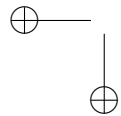
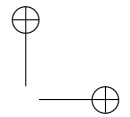
- 3510 Lynch, K., Jackson, D. W., and Cooper, J. A. G. (2016). The fetch effect on aeolian  
3511 sediment transport on a sandy beach: a case study from magilligan strand, northern  
3512 ireland. *Earth Surface Processes and Landforms*.
- 3513 Lynch, K., Jackson, D. W. T., and Cooper, J. A. G. (2008). Aeolian fetch distance  
3514 and secondary airflow effects: the influence of micro-scale variables on meso-scale  
3515 foredune development. *Earth Surface Processes and Landforms*, 33(7):991–1005.
- 3516 Martin, R. L. and Kok, J. F. (2016). Field measurements demonstrate distinct initiation  
3517 and cessation thresholds governing aeolian sediment transport flux. Submitted.
- 3518 Masselink, G., Auger, N., Russell, P., and O'Hare, T. (2007). Short-term morpholog-  
3519 ical change and sediment dynamics in the intertidal zone of a macrotidal beach.  
3520 *Sedimentology*, 54:39–53.
- 3521 McKenna Neuman, C., Li, B., and Nash, D. (2012). Micro-topographic analysis of  
3522 shell pavements formed by aeolian transport in a wind tunnel simulation. *Journal*  
3523 *of Geophysical Research*, 117(F4). F04003.
- 3524 McKenna Neuman, C. and Nickling, W. (1995). Aeolian sediment flux decay: Non-  
3525 linear behaviour on developing deflation lag surfaces. *Earth Surface Processes and*  
3526 *Landforms*, 20(5):423–435.
- 3527 McKenna Neuman, C. and Sanderson, S. (2008). Humidity control of particle emis-  
3528 sions in aeolian systems. *Journal of Geophysical Research*, 113(F2). F02S14.
- 3529 Min. V&W (1990). A new coastal defence policy for the netherlands. Rijkswaterstaat.
- 3530 Namikas, S. L., Edwards, B. L., Bitton, M. C. A., Booth, J. L., and Zhu, Y. (2010).  
3531 Temporal and spatial variabilities in the surface moisture content of a fine-grained  
3532 beach. *Geomorphology*, 114:303–310.
- 3533 Nickling, W. and McKenna Neuman, C. (1995). Development of deflation lag surfaces.  
3534 *Sedimentology*, 42(3):403–414.
- 3535 Nickling, W. G. and Ecclestone, M. (1981). The effects of soluble salts on the threshold  
3536 shear velocity of fine sand. *Sedimentology*, 28:505–510.
- 3537 Ojeda, E., Ruessink, B., and Guillen, J. (2008). Morphodynamic response of a two-  
3538 barred beach to a shoreface nourishment. *Coastal Engineering*, 55(12):1185–1196.
- 3539 Okin, G. S. (2008). A new model of wind erosion in the presence of vegetation. *Journal*  
3540 *of Geophysical Research*, 113(F2). F02S10.
- 3541 Owen, P. R. (1964). Saltation of uniform grains in air. *J. Fluid Mech*, 20(2):225–242.
- 3542 Peckham, S. D., Hutton, E. W. H., and Norris, B. (2013). A component-based approach  
3543 to integrated modeling in the geosciences: The design of CSDMS. *Computers and*  
3544 *Geosciences*, 53:3–12.
- 3545 Pye, K. and Tsoar, H. (1990). *Aeolian Sand and Sand Dunes*. Unwin Hyman, London.

- 3546 Raupach, M., Gillette, D., and Leys, J. (1993). The effect of roughness elements on  
3547 wind erosion threshold. *Journal of Geophysical Research: Atmospheres*, 98(D2):3023–  
3548 3029.
- 3549 Reniers, A., Gallagher, E., MacMahan, J., Brown, J., Rooijen, A., Thiel de Vries, J., and  
3550 Prooijen, B. (2013). Observations and modeling of steep-beach grain-size variability.  
3551 *Journal of Geophysical Research: Oceans*, 118(2):577–591.
- 3552 Roelvink, J. A., Reniers, A., van Dongeren, A. P., van Thiel de Vries, J. S. M., McCall,  
3553 R. T., and Lescinski, J. (2009). Modelling storm impacts on beaches, dunes and  
3554 barrier islands. *Coastal Engineering*, 56(11):1133–1152.
- 3555 Scheidt, S., Ramsey, M., and Lancaster, N. (2010). Determining soil moisture and  
3556 sediment availability at white sands dune field, new mexico, from apparent thermal  
3557 inertia data. *Journal of Geophysical Research*, 115(F2). F02019.
- 3558 Sherman, D. J., Jackson, D. W., Namikas, S. L., and Wang, J. (1998). Wind-blown sand  
3559 on beaches: an evaluation of models. *Geomorphology*, 22(2):113–133.
- 3560 Sherman, D. J. and Li, B. (2012). Predicting aeolian sand transport rates: a reevaluation  
3561 of models. *Aeolian Research*, 3(4):371–378.
- 3562 Shuttleworth, W. J. (1993). Evaporation. In Maidment, D. R., editor, *Handbook of  
3563 Hydrology*, pages 4.1–4.53. McGraw-Hill, New York.
- 3564 Sørensen, M. (2004). On the rate of aeolian sand transport. *Geomorphology*, 59(1):53–62.
- 3565 Spearman, C. (1904). The proof and measurement of association between two things.  
3566 *American Journal of Psychology*, 15:72–101.
- 3567 Stive, M. J. F., de Schipper, M. A., Luijendijk, A. P., Aarninkhof, S. G. J., van Gelder-  
3568 Maas, C., van Thiel de Vries, J. S. M., de Vries, S., Henriquez, M., Marx, S., and  
3569 Ranasinghe, R. (2013). A new alternative to saving our beaches from sea-level rise:  
3570 the Sand Engine. *Journal of Coastal Research*, 29(5):1001–1008.
- 3571 Stockdon, H. F., Holman, R. A., Howd, P. A., and Sallenger, A. H. (2006). Empirical  
3572 parameterization of setup, swash, and runup. *Coastal engineering*, 53(7):573–588.
- 3573 Stout, J. E. (2004). A method for establishing the critical threshold for aeolian transport  
3574 in the field. *Earth Surface Processes and Landforms*, 29(10):1195–1207.
- 3575 Tan, L., Zhang, W., Qu, J., Zhang, K., An, Z., and Wang, X. (2013). Aeolian sand  
3576 transport over gobi with different gravel coverages under limited sand supply: a  
3577 mobile wind tunnel investigation. *Aeolian Research*, 11:67–74.
- 3578 Turpin, C., Badr, T., and Harion, J. L. (2010). Numerical modelling of aeolian erosion  
3579 over rough surfaces. *Earth Surface Processes and Landforms*, 35(12):1418–1429.
- 3580 Udo, K., Kuriyama, Y., and Jackson, D. W. T. (2008). Observations of wind-blown sand  
3581 under various meteorological conditions at a beach. *Journal of Geophysical Research*,  
3582 113(F4). F04008.

- 3583 van der Wal, D. (1998). The impact of the grain-size distribution of nourishment sand  
3584 on aeolian sand transport. *Journal of Coastal Research*, pages 620–631.
- 3585 van der Wal, D. (2000). Grain-size-selective aeolian sand transport on a nourished  
3586 beach. *Journal of Coastal Research*, pages 896–908.
- 3587 van Genuchten, M. T. (1978). Mass transport in saturated-unsaturated media: one-  
3588 dimensional solutions. Technical Report Research Report No. 78-WR-11, Univ.  
3589 Princeton, NJ. Water Resources Program.
- 3590 Van Slobbe, E., De Vriend, H., Aarninkhof, S., Lulofs, K., De Vries, M., and Dircke, P.  
3591 (2013). Building with nature: in search of resilient storm surge protection strategies.  
3592 *Natural hazards*, 65(1):947–966.
- 3593 Šimůnek, J., Šejna, M., and van Genuchten, M. T. (1998). *The HYDRUS-1D software  
3594 package for simulating the one-dimensional movement of water, heat, and multiple solutes  
3595 in variably-saturated media*. International Ground Water Modeling Center, Colorado  
3596 School of Mines, Golden, Colorado, version 1.0. igwmc - tps - 70 edition. 186pp.
- 3597 Walstra, D. J. R. (2016). *On the anatomy of nearshore sandbars: a systematic exposition of  
3598 inter-annual sandbar dynamics*. PhD thesis, Delft University of Technology, Delft.
- 3599 Waterman, R. E. (2010). *Integrated coastal policy via Building with Nature*. TU Delft, Delft  
3600 University of Technology.
- 3601 Weng, W. S., Hunt, J. C. R., Carruthers, D. J., Warren, A., and Wiggs, G. F. S. (1991).  
3602 Air flow and sand transport over sand-dunes. *Acta Mechanica*, 2:1–22.
- 3603 Wiggs, G. F. S., Baird, A. J., and Atherton, R. J. (2004). The dynamic effects of moisture  
3604 on the entrainment and transport of sand by wind. *Geomorphology*, 59:13–30.
- 3605 Williams, A. T. (1971). An analysis of some factors involved in the depth of distur-  
3606 bance of beach sand by waves. *Marine Geology*, 11(3):145–158.



"thesis" — 2016/11/15 — 10:57 — page 128 — #158



---

3607 ACKNOWLEDGMENTS

---

3608 In the spring of 2012 I was still convinced that I would never engage in a PhD research  
3609 as it would be too specialized, too enduring and too lonely. Four years later, I learned  
3610 that an enduring (but hardly lonely) specialization fits me rather well and is an ex-  
3611 perience I would not want to have missed. Now I'm indebted to Jaap for bringing  
3612 the NEMO proposal to my attention. To Roos for convincing me to apply for a PhD  
3613 position after I had been rambling on about the proposal for weeks, apparently. She  
3614 was also the one that finally made me accept that it was time to wrap up and finish. I  
3615 thank Jaap and Sierd for their enthusiastic supervision. I thank Marcel for accepting  
3616 me on the NEMO project and providing me once again with the freedom to explore.  
3617 I thank Deltares for their generous support in this personal endeavor and Noor and  
3618 Jolijn for not keeping me up too many nights in the final year of my research.

3619 I have a special memory towards the six week MEGAPEX field campaign at the  
3620 Sand Motor, which was a surrealistic experience that illustrates how a group of  
3621 overly enthusiastic scientists is able to built a beautiful scientific dataset from a huge  
3622 pile of sand. Either by Meagan's state-of-the-art equipment that apparently require  
3623 American-sized *Freedom Poles* for appropriate mounting, or by the elegance of simple  
3624 solutions to complex problems, like Nick "Topo is My Life" Cohn walking his daily  
3625 transects accumulating to the equivalent of a pilgrimage to Santiago de Compostela. I  
3626 will not easily forget the first time Sierd and I deployed the nails as low-tech measure  
3627 for micro-topographic changes over a single tidal cycle. Due to unfortunate planning  
3628 we had to measure and retrieve the first batch nails (4 cm long, 3 mm thick) in the  
3629 middle of the night in pitch-dark. Waving our torches over the beach it took us only  
3630 about a few minutes to find a beautiful array of nails protruding proudly about 1  
3631 cm from the bed. Priceless! We learned so much these weeks. I thank the entire  
3632 MEGAPEX team for this exhausting experience, the assistance with our laborious sub-  
3633 aerial measurements, the proliferation of American flags at the Sand Motor (U-S-A!)  
3634 and the free pumpkins.

3635 Except for the six weeks at the Sand Motor, I shared a room at the Faculty of  
3636 Civil Engineering with my fellow NEMO promovendi Saulo and Bas, and Max, our  
3637 adopted son from the NatureCoast project. It has been a highly fruitful and challeng-  
3638 ing environment to work in, despite our research was only superficially related. I  
3639 much appreciated the discussions on what we all could do in our newly obtained and  
3640 privileged position: the utter necessity of face recognition in our room, the benefits of  
3641 having our own 4x4 and the possible improvements to our typical Dutch bread-and-  
3642 cheese lunch. But soon we found ourselves juggling with an enormous amount of  
3643 actual scientific ideas, international co-operations, measurement equipment stacked  
3644 around our desks and an abundance of data. Scientific research appeared to be a  
3645 very practical daily activity. Discussions started to shift accordingly: how to deploy  
3646 equipment in the field, how to solder your own measurement devices, what Python  
3647 package will get the most out of your data and when does data analysis become data  
3648 torture? Finally, when it occurred to us that the NEMO project had produced more  
3649 children than papers, the focus shifted once again to finalizing our research. I much

3650 appreciated the weekly papers & coffee meetings with Saulo regarding our writing  
3651 progress. We both needed it.

3652 As said, these four years appeared not to be so lonely after all. Luckily, since the  
3653 best ideas arise in conversation. Little pieces that fit together and make you under-  
3654 stand. I thank Sierd de Vries, Saulo Meirelles Nunes da Rocha, Max Radermacher, Bas  
3655 Huisman, Matthieu de Schipper, Martijn Henriquez, Ronald Brouwer, Marcel Stive,  
3656 Jaap van Thiel de Vries, Bert van der Valk, Ad van der Spek, Arjen Luijendijk, Dano  
3657 Roelvink, Fedor Baart, Kees den Heijer, Irv Elshoff, Mart Borsboom, Wiepke Jäger, Ad  
3658 Reniers, Thom Bogaard, Martine Rutten, Susan Steele, Laurens van der Maaten, Thea  
3659 Vuik, Duncan van der Heul, Lianne van der Weerd, Kathelijne Wijnberg, Leonardo  
3660 Duarte Campos, Filipe Galiforni Silva, Isaac Williams, Gerben Ruessink, Winnie de  
3661 Winter, Pam Hage, Yvonne Smit, Jasper Donker, Timothy Price, Maarten Kleinhans,  
3662 Sebastian Huizer, Marc Bierkens, Corjan Nolet, Joep Keijsers, Ate Poortinga, Michel  
3663 Riksen, Nick Cohn, Peter Ruggiero, Laura Moore, Orcencio Durán, Evan Goldstein,  
3664 Edie Gallagher, Daniel Buscombe, Andrew Cooper, Irene Delgado-Fernandez, Robert  
3665 Davidson-Arnott, Tom Barchyn, Giovanni Coco, Gerd Masselink, Bonnie Ludka, Mea-  
3666 gan Wengrove, Caroline Fredriksson, Bas Arens, Roeland de Zeeuw, Leon Roessen,  
3667 Bert Bakker, Jos van Meurs, Henk Tiggeloven, Giel Hermans, Steve van Herk, Sander  
3668 de Vree, Frank Kalkman, Jaap van Duin and the anonymous reviewers for all the little  
3669 pieces that made up this thesis.

3670  
3671

Bas Hoonhout  
Delft, September 2016

---

3672 CURRICULUM VITAE

---

3673 PERSONALIA

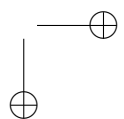
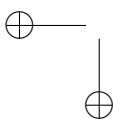
Bas Hoonhout  
26-06-1983, Amsterdam, Nederland

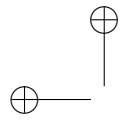
3674 EDUCATION

Montessori Lyceum Amsterdam, VWO (1995-2001)  
Delft University of Technology, Civil Engineering: Dune Erosion along  
Curved Coastlines (2002-2009, cum laude)

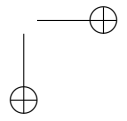
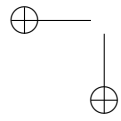
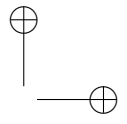
3675 EMPLOYMENT

Deltares, 2009—





"thesis" — 2016/11/15 — 10:57 — page 132 — #162



---

3676 PUBLICATIONS

---

3677 PEER-REVIEWED ARTICLES

- 3678 Hoonhout, B. M. and de Vries, S. (2016d). A process-based model for aeolian sediment  
3679 transport and spatiotemporal varying sediment availability. *Journal of Geophysical*  
3680 *Research: Earth Surface*. 2015JF003692.
- 3681 Hoonhout, B. M. and de Vries, S. (2016a). Aeolian sediment supply at a mega nour-  
3682 ishment. *Coastal Engineering*. Submitted.
- 3683 Hoonhout, B. M. and de Vries, S. (2016c). Field measurements on spatial variations in  
3684 aeolian sediment availability at the sand motor mega nourishment. *Aeolian Research*.  
3685 Submitted.
- 3686 Hoonhout, B. M., Radermacher, M., Baart, F., and Van der Maaten, L. J. P. (2015c). An  
3687 automated method for semantic classification of regions in coastal images. *Coastal*  
3688 *Engineering*, 105:1–12.
- 3689 Hoonhout, B. M., Baart, F., and Van Thiel de Vries, J. S. M. (2014a). Intertidal beach  
3690 classification in infrared images. *Journal of Coastal Research*, SI 66:657–662.

3691 CONFERENCES

- 3692 Hoonhout, B. M., Cohn, N., de Vries, S., Roelvink, J. A., Ruggiero, P., Moore, L. J.,  
3693 Durán, O., and Goldstein, E. (2016a). How tides and waves enhance aeolian sedi-  
3694 ment transport at the sand motor. In *Proceedings of the 35th International Conference*  
3695 *on Coastal Engineering*.
- 3696 Hoonhout, B. M. and de Vries, S. (2016b). Aeolis: A new model for aeolian sediment  
3697 supply and transport. In *Proceedings of the NCK-days 2016*.
- 3698 Hoonhout, B. M., Cohn, N., de Vries, S., Roelvink, J. A., Ruggiero, P., Moore, L. J.,  
3699 Durán, O., and Goldstein, E. (2016b). How tides and waves enhance aeolian sedi-  
3700 ment transport at the sand motor. In *Proceedings of the Ocean Sciences Meeting 2016*.
- 3701 Hoonhout, B. M., de Vries, S., and Cohn, N. (2015a). The influence of spatially varying  
3702 supply on coastal aeolian transport: a field experiment. In *Proceedings of Coastal*  
3703 *Sediments*, San Diego, USA.
- 3704 Hoonhout, B. M., de Vries, S., and Cohn, N. (2015b). The influence of spatially varying  
3705 supply on coastal aeolian transport: A field experiment. In *Proceedings of the NCK-*  
3706 *days 2015*.
- 3707 Hoonhout, B. M. and de Vries, S. (2014b). Process-based modeling of supply-limited  
3708 aeolian transport in coastal environments. In *Proceedings of the International Confer-*  
3709 *ence on Aeolian Research 2014*.

- 3710 Hoonhout, B. M., van Thiel de Vries, J. S. M., Curto, V., and Stive, M. J. F. (2014b).  
3711 Monitoring supply limiting conditions using imageing techniques. In *Proceedings*  
3712 of the 34th International Conference on Coastal Engineering.
- 3713 Hoonhout, B. M. and de Vries, S. (2014a). Modelling and monitoring of meso-scale  
3714 supply-limited aeolian transport. In *Proceedings of the NCK-days 2014*.
- 3715 Hoonhout, B. M., de Vries, S., Baart, F., van Thiel de Vries, J. S. M., van der Weerd, L.,  
3716 and Wijnberg, K. M. (2013). Monitoring of beach surface properties with remote  
3717 sensing. In *Proceedings of Coastal Dynamics*, Arcachon, France.
- 3718 Hoonhout, B. M. (2013). Monitoring the process of aeolian transport. In *Proceedings of*  
3719 *the NCK-days 2013*.
- 3720 Hoonhout, B. M. and van Thiel de Vries, J. S. M. (2012). Modeling dune erosion,  
3721 overwash and inundation of barrier islands. In *Proceedings of the 33rd International*  
3722 *Conference on Coastal Engineering*, Santander, Spain.
- 3723 Hoonhout, B. M. and den Heijer, C. (2010). Reliability of dune erosion assessment  
3724 along curved coastlines. In *Proceedings of the 32nd International Conference on Coastal*  
3725 *Engineering*, Shanghai, China.

3726 SOFTWARE AND DATA

- 3727 Hoonhout, B. M. (2016b). Aeolis v1.1: A process-based model for simulating  
3728 availability-limited aeolian sediment transport. GIT repository.
- 3729 Hoonhout, B. M. (2016a). Aeolis model setups v2.0. GIT repository.
- 3730 Hoonhout, B. M., de Vries, S., and Cohn, N. (2016c). Field measurements on aeolian  
3731 sediment transport at the sand motor mega nourishment during the megapex field  
3732 campaign. OpenDAP server.
- 3733 Hoonhout, B. M. and Radermacher, M. (2015b). Flamingo: a coastal image analysis  
3734 toolbox. GIT repository.
- 3735 Hoonhout, B. M. and Radermacher, M. (2015a). Annotated images of the dutch coast.  
3736 FTP server.

3737

3738 COLOPHON

3739 Measurement data presented in this thesis is open-source and can be obtained through  
3740 the 4TU.ResearchData initiative at:

3741 [data.tu.nl](http://data.tu.nl)

3742 The AEOLiS model presented in this thesis is open-source and can be obtained through  
3743 the OpenEarth GitHub repository at:

3744 [github.com/openearth/aeolis-python/](https://github.com/openearth/aeolis-python/)

3745 The model schematizations presented in this thesis are open-source and can be ob-  
3746 tained through the OpenEarth GitHub repository at:

3747 [github.com/openearth/aeolis-models/](https://github.com/openearth/aeolis-models/)

3748 The technical documentation of the AEOLiS model can be found at:

3749 [aeolis.readthedocs.io](https://aeolis.readthedocs.io)

3750 All scripts that are used for analysis of measurement data, model setup and the gen-  
3751 eration of figures and tables, including an ANSIBLE playbook that generates this thesis  
3752 from raw data, are published through the author's private GitHub repository at:

3753 [github.com/hoonhout/phd/](https://github.com/hoonhout/phd/)

3754 This document was typeset using the typographical look-and-feel `classicthesis` de-  
3755 veloped by André Miede.